

11-9-2017


Origami Reconfigurable Electromagnetic Systems

Shun Yao

Florida International University, syao002@fiu.edu

DOI: 10.25148/etd.FIDC004049

Follow this and additional works at: <https://digitalcommons.fiu.edu/etd>

 Part of the [Electrical and Electronics Commons](#), and the [Electromagnetics and Photonics Commons](#)

Recommended Citation

Yao, Shun, "Origami Reconfigurable Electromagnetic Systems" (2017). *FIU Electronic Theses and Dissertations*. 3514.
<https://digitalcommons.fiu.edu/etd/3514>

This work is brought to you for free and open access by the University Graduate School at FIU Digital Commons. It has been accepted for inclusion in FIU Electronic Theses and Dissertations by an authorized administrator of FIU Digital Commons. For more information, please contact dcc@fiu.edu.

FLORIDA INTERNATIONAL UNIVERSITY

Miami, Florida

ORIGAMI RECONFIGURABLE ELECTROMAGNETIC SYSTEMS

A dissertation submitted in partial fulfillment of

the requirements for the degree of

DOCTOR OF PHILOSOPHY

in

ELECTRICAL ENGINEERING

by

Shun Yao

2017

To: Dean John L. Volakis
College of Engineering and Computing

This dissertation, written by Shun Yao, and entitled Origami Reconfigurable Electromagnetic Systems, having been approved in respect to style and intellectual content, is referred to you for judgment.

We have read this dissertation and recommend that it be approved.

Nezih Pala

Jean H. Andrian

Berrin Tansel

Manos M. Tentzeris

Stavros V. Georgakopoulos, Major Professor

Date of Defense: November 09, 2017.

The dissertation of Shun Yao is approved.

Dean John L. Volakis
College of Engineering and Computing

Andres G. Gil
Vice President for Research and Economic Development
and Dean of the University Graduate School

Florida International University, 2017

© Copyright 2017 by Shun Yao

All rights reserved.

DEDICATION

I dedicate this dissertation to my lovely family. Without their love, understanding and support, the completion of this work would never have been achievable.

ACKNOWLEDGMENTS

I would like to express my sincerest gratitude to my major professor, Dr. Stavros V. Georgakopoulos, for his great mentoring and support through my Ph.D. program at FIU. He provided the most excellent research environment with the latest research software and top advanced equipment. He has truly given me the confidence and knowledge base to excel in the next stage of my career. I also appreciate Dr. Nezhil Pala, Dr. Jean H. Andrian, Dr. Berrin Tansel, and Dr. Manos M. Tentzeris for serving on my dissertation defense committee and for their illuminating comments.

I am sincerely thankful for my wife who encouraged me throughout the research. Thanks for her love, understanding, encouragement and advice. I also thank all the members of FIU Electrical and Computing Engineering Department and special thanks to Dr. Hao Hu, Kun Bao, Daerhan Liu, Xueli Liu, John Gibson, Karina Quintana, Elad Siman Tov, Pablo Gonzalez, Yonathan Bonan, Dr. Yipeng Qu, Dr. Olutola Jonah, Xiang Li, and Oscar Silveira for their help and friendship.

ABSTRACT OF THE DISSERTATION
ORIGAMI RECONFIGURABLE ELECTROMAGNETIC SYSTEMS

by

Shun Yao

Florida International University, 2017

Miami, Florida

Professor Stavros. V. Georgakopoulos, Major Professor

With the ever-increasing demand for wireless communications, there is a great need for efficient designs of electromagnetic systems. Reconfigurable electromagnetic systems are very useful because such designs can provide multi-functionality and support different services. The geometrical topology of an electromagnetic element is very important as it determines the element's RF performance characteristics. Origami geometries have significant advantages for launch-and-carry electromagnetic devices where devices need to fold in order to miniaturize their size during launch and unfold in order to operate after the platform has reached orbit.

This dissertation demonstrates a practical process for designing reconfigurable electromagnetic devices using origami structures. Four different origami structures are studied and the integrated Mathematical-Computational-Electromagnetic models of origami antennas, origami reflectors and origami antenna arrays are developed and analyzed. These devices provide many unique capabilities compared with the traditional designs, such as band-switching, frequency tuning, polarization adjustment and mode reconfigurability. Prototypes are also manufactured to validate the performances of the designs. These designs change their geometry naturally, and they can be compactly

packaged into small volume, which make them very suitable for spaceborne and satellite communication. Origami antennas and origami electromagnetics are expected to impact a variety of applications related to communications, surveillance and sensing.

TABLE OF CONTENTS

CHAPTER	PAGE
1. INTRODUCTION.....	1
1.1 Problem Statement.....	1
1.2 Research Objectives and Contributions.....	3
1.3 Methodology.....	4
1.4 Dissertation Outline.....	5
2. BACKGROUND AND RELATED WORK.....	6
2.1 Origami Art.....	6
2.2 Reconfigurable Electromagnetic Devices.....	7
2.3 Origami Structures Used in Electromagnetic Systems.....	9
3. ORIGAMI ACCORDION STRUCTURE BASED ANTENNA AND REFLECTOR.....	11
3.1 Origami Accordion Structure.....	11
3.2 9-Level Origami Accordion Antenna.....	14
3.3 Tunable Origami Accordion Antenna.....	19
3.4 Origami Accordion Reflector.....	24
4. ORIGAMI SPRING STRUCTURE BASED ANTENNA AND ANTENNA ARRAY.....	27
4.1 Origami Spring Structure.....	27
4.2 Tunable UHF Origami Spring Antenna with Actuation System.....	29
4.3 A Self-deploy Yagi Loop Antenna Based on Origami Spring Structure.....	35
4.3.1 Origami Yagi Loop Antenna Design.....	36
4.3.2 Origami Yagi loop Antenna Construction and Results.....	39
5. MORPHING ORIGAMI CONICAL SPIRAL ANTENNA.....	43
5.1 Introduction of the Conical Spiral Antenna.....	44
5.2 Design of Nojima Origami CSA.....	46
5.3 Comparison between the Nojima Origami CSA and the Traditional CSA.....	54
5.4 Manufacture and Measurements of Nojima Square CSA Prototype.....	65
5.5 Summary.....	75
6. ORIGAMI SEGMENTED HELICAL ANTENNA WITH SWITCHABLE SENSE OF POLARIZATION.....	77
6.1 Introduction of Techniques for HA Volume Reduction and Polarization Switching.....	78
6.2 The Hyperbolic Paraboloid Origami Unit for Origami SHA.....	79
6.3 Origami Segmented Helical Antenna.....	85
6.4 Segmented Helical Antenna on Origami-Inspired Skeleton Scaffolding.....	93
6.5 Skeleton Segmented Helical Antenna Performance.....	97

7. CONCLUSION AND FUTURE WORK.....	105
7.1 Conclusions.....	105
7.2 Future Work.....	106
REFERENCES	108
VITA.....	119

LIST OF TABLES

TABLE	PAGE
Table 5.1. Parameters of the Nojima Origami CSAs.....	57
Table 6.1. Measured Far-field Characteristics of Origami SHA.	91
Table 6.2. Geometry Parameters of the Segmented Helical Antenna.....	97
Table 6.3. Comparison between the SHAs and the Conventional SHA.....	100
Table 6.4. Simulated Gain versus Number of Turns of the Bifilar Skeleton SHA.....	103

LIST OF FIGURES

FIGURE	PAGE
Figure 3.1. Accordion structure.	12
Figure 3.2. Metal strip on the accordion structure base.	12
Figure 3.3. (a) Creased base material. (b) Folding the base material.	13
Figure 3.4. (a) Paper unit before folding. (b) Folded paper unit. (c) Front view of folded paper unit.	14
Figure 3.5. 9-Level origami accordion antenna model in ANSYS HFSS.	15
Figure 3.6. (a) Flat paper with copper strip. (b) Side view, (c) top view and (d) bottom view of the manufactured origami accordion antenna.	16
Figure 3.7. S_{11} of the accordion antenna at (a) the unfolded state, 160 mm height, and (b) the folded state, 40 mm height.	17
Figure 3.8. Simulated and measured normalized radiation pattern for elevation plane for $\varphi = 0^\circ$ at: (a) unfolded state, and (b) folded state.	18
Figure 3.9. Realized gain at (a) 160 mm height and (b) 40 mm height.	19
Figure 3.10. Tunable origami accordion antenna model.	20
Figure 3.11. (a) Simulation models of tunable accordion antenna for different heights. (b) Prototypes of tunable accordion antenna for different heights.	21
Figure 3.12. (a) Simulated S_{11} of the tunable accordion antenna. (b) Measured S_{11} of the tunable accordion antenna.	22
Figure 3.13. The realized gain along the central axis of the 3-level accordion antenna versus frequency when the height of each level changes from 2 mm to 10 mm.	23
Figure 3.14. (a) Simulated and measured radiation pattern for elevation plane. (b) Antenna is in the anechoic chamber.	24
Figure 3.15. Tunable origami accordion reflector structure.	25
Figure 3.16. Tunable origami accordion reflector structure.	25
Figure 3.17. The simulated elevation radiation pattern for $\varphi = 0^\circ$ of (a) the unfolded antenna at 670 MHz, and (b) the folded antenna at 1400 MHz.	26

Figure 4.1. (a) Origami spring paper structure. (b) Creased paper for folding origami spring.	28
Figure 4.2. (a) Origami spring paper structure. (b) Creased paper for folding origami ...	29
Figure 4.3. Copper layer on the origami spring paper base.	30
Figure 4.4. Simulation model of the origami spring antenna in ANSYS HFSS.....	31
Figure 4.5. Simulated reflection coefficient of the origami spring antenna at different states.	32
Figure 4.6. Simulate realized gain pattern of the origami spring antenna at (a) 1.09 GHz with $h = 16$ mm, (b)1.17 GHz with $h = 20$ mm, (c)1.24 GHz with $h = 24$ mm, (d)1.29 GHz with $h = 28$ mm (e)1.34 GHz with $h = 32$ mm and (f)1.39 GHz with $h = 36$ mm.	33
Figure 4.7. Simulated axial ratio along the $+z$ direction	33
Figure 4.8. Origami spring antenna prototype with the actuation system at (a) 145 mm height, and (b) 60 mm height.....	34
Figure 4.9. Measured efficiency of three-band CSCMR system for different distances.	35
Figure 4.10. Yagi array with circular loops.	36
Figure 4.11. The simulation model of Yagi origami loop antenna at: (a) folded state and (b) unfolded state.	38
Figure 4.12. The input impedance of the origami Yagi loop array.....	39
Figure 4.13. The manufactured prototype of the Yagi origami loop antenna at: (a) unfolded state and (b) folded state.....	40
Figure 4.14. Reflection coefficient of the origami Yagi loop array.....	41
Figure 4.15. (a) Radiation pattern of elevation plane when $\phi = 0^\circ$. (b) Radiation pattern of azimuth plane when $\theta = 90^\circ$	41
Figure 5.1. Geometry of a two-arm conical spiral antenna.....	45
Figure 5.2. (a) Geometry of flat Nojima pattern sheet with a square central-hub. (b) Semi folded Nojima pattern sheet. (c) Fully folded Nojima pattern sheet. ...	48
Figure 5.3. (a) Metal strip on the fully folded square central-hub Nojima wrap pattern. (b) Cross-section through the symmetry axis of the pyramid.....	50

Figure 5.4. The angles along the metal strip line (valley fold line).	51
Figure 5.5. The metal layer area for best antenna performance.....	53
Figure 5.6. (a) The traditional CSA. (b) Hexagon central-hub Nojima origami CSA. (c) Square central-hub Nojima origami CSA.	54
Figure 5.7. (a) Metal layer on the planar hexagon central-hub Nojima pattern. (b) Metal layer on the planar square central-hub Nojima pattern.	56
Figure 5.8. Simulated input impedance of three CSA antennas.	58
Figure 5.9. Simulated gain along the +z direction of three CSA antennas.	59
Figure 5.10. The surface current density distribution of (a) the traditional CSA at 2.5 GHz, (b) the traditional CSA at 3.5 GHz, (c) the Nojima hexagon CSA at 2.5 GHz, (d) the Nojima hexagon CSA at 3.5 GHz, (e) the Nojima square CSA at 2.5 GHz, (f) the Nojima square CSA at 3.5 GHz.....	61
Figure 5.11. Simulated axial ratio along the +z direction of three CSA antennas.....	62
Figure 5.12. Elevation patterns for the right-handed and left-handed circular polarized components of the electric field at the frequency $f = 3$ GHz: (a) traditional CSA for $\phi = 0^\circ$, (b) traditional CSA for $\phi = 90^\circ$, (c) Nojima hexagon CSA for $\phi = 0^\circ$, (d) Nojima hexagon CSA for $\phi = 90^\circ$, and (e) Nojima square CSA for $\phi = 0^\circ$, (f) Nojima square CSA for $\phi = 90^\circ$	64
Figure 5.13. (a) Square central-hub Nojima pattern with $\alpha' = 15^\circ$. (b) 2 turns Nojima origami square CSA.....	65
Figure 5.14. The prototype of the Nojima square CSA at (a) unfolded state and (b) fully folded state.	66
Figure 5.15. The front and back side of the linearly tapered microstrip balun.....	67
Figure 5.16. The simulation Nojima square CSA model with balun at (a) unfolded state and (b) fully folded state.	68
Figure 5.17. The simulated and measured S_{11} of the Nojima square CSA at the unfolded state.....	69
Figure 5.18. The simulated and measured S_{11} of the Nojima square CSA at the unfolded state.....	70
Figure 5.19. Simulated 3-D radiation pattern of the Nojima square CSA at (a) 0.48 GHz for unfolded state and (b) 2.5 GHz for folded state.	71

Figure 5.20. Simulated and measured realized gain pattern of the Nojima square CSA at unfolded state for (a) elevation plane when $\phi = 90^\circ$, and (b) azimuth plane.....	71
Figure 5.21. Simulated and measured realized gain along the +z direction of the Nojima square CSA at the folded state.....	72
Figure 5.22. Simulated and measured realized gain axial ratio along the +z direction of the Nojima square CSA at the folded state.....	73
Figure 5.23. The simulated and measured realized gain patterns along the +z direction of the Nojima square CSA at the folded state for (a) 2.5 GHz, $\phi = 0^\circ$, (b) 2.5 GHz, $\phi = 90^\circ$, (c) 3 GHz, $\phi = 0^\circ$, (d) 3 GHz, $\phi = 90^\circ$	74
Figure 6.1. (a) Creased square pattern for hyperbolic paraboloid origami. (b) Hyperbolic paraboloid origami.....	80
Figure 6.2. Origami paper base that can rotate around its center axis with multiple hyperbolic paraboloid units.	81
Figure 6.3. The origami rectangle unit pattern for the hyperbolic paraboloid with the antenna traces.....	81
Figure 6.4. (a) Top view and (b) side view of a rectangle hyperbolic paraboloid origami unit with the antenna traces.....	82
Figure 6.5. Rectangle hyperbolic paraboloid origami unit at the compact intermediate state for stowing.....	83
Figure 6.6. The hyperbolic paraboloid origami unit for (a) 150 μm -thick paper at left-hand state, (b) 150 μm -thick paper at right-hand state, (c) 50 μm -thick (2-mil) Kapton film at left-hand state, (d) 50 μm -thick (2-mil) Kapton film at right-hand state, (e) 76 μm -thick (3-mil) Kapton film at left-hand state, (f) 76 μm -thick (3-mil) Kapton film at right-hand state, (g) 127 μm -thick (5-mil) Kapton film at left-hand state, and (h) 127 μm -thick (5-mil) Kapton film at right-hand state.....	84
Figure 6.7. The side view of (a) the origami SHA, and (b) the conventional HA. The top view of (c) the origami SHA, and (d) the conventional HA.....	87
Figure 6.8. Simulated S_{11} of the conventional HA and origami SHA.	88
Figure 6.9. The manufactured prototype of origami SHA at (a) left-handed state and (b) right-handed state.	88
Figure 6.10. (a) Expanded telescoping central axis, (b) Collapsed telescoping central axis, (c) Tightly folded origami SHA.	89

Figure 6.11. Measured S_{11} of the origami based SHA at both left-hand state and right-hand state.	90
Figure 6.12. Measured elevation patterns of the origami SHA for the RHCP and LHCP components of the electric field at 0.98 GHz: (a) $\varphi = 0^\circ$ at the left-hand state, (b) $\varphi = 90^\circ$ at the left-hand state, (c) $\varphi = 0^\circ$ at the right-hand state, and (d) $\varphi = 90^\circ$ at the right-hand state.....	92
Figure 6.13. Unit of the supporting skeleton of the SHA.	94
Figure 6.14. The simulation model of (a) the hexagon SHA at left-hand state, (b) the hexagon SHA at right-hand state, (c) the square SHA at left-hand state and (d) the square SHA at right-hand state.	95
Figure 6.15. Manufactured prototype of the (a) hexagon skeleton SHA, (b) square skeleton SHA, and (c) conventional HA.	98
Figure 6.16. Measured elevation patterns for the RHCP and LHCP components of the electric field: (a) hexagon SHA for $\varphi = 0^\circ$ at the right-hand state, (b) hexagon SHA for $\varphi = 90^\circ$ at the right-hand state, (c) hexagon SHA for $\varphi = 0^\circ$ at the left-hand state, (d) hexagon SHA for $\varphi = 90^\circ$ at the left-hand state, (e) square SHA for $\varphi = 0^\circ$ at the right-hand state, (f) square SHA for $\varphi = 90^\circ$ at the right-hand state, (g) square SHA for $\varphi = 0^\circ$ at the left-hand state, and (h) square SHA for $\varphi = 90^\circ$ at the left-hand state.....	102
Figure 6.17. (a) Deployable skeleton scaffolding for square SHA. (b) Compressed square skeleton SHA.....	104

CHAPTER 1

INTRODUCTION

1.1 Problem Statement

There has been a large amount of work by mathematicians and engineers on folding/unfolding systems over the past two decades. The focus is usually on the construction of an object and its proper mechanism to unfold. The ability of an object to unfold is often referred to as deployability. The modern origami art emerged in the 1950s and inspired a new generation of not only artists, but also scientists [1-2]. Origami and more generally folding and unfolding systems have been used in engineering and their geometries have been mathematically examined [3-5]. Origami systems are particularly suitable for applications where deployability, collapsibility, and stowability are important. Engineers have used origami art to design folding space telescopes that can compactly fit into small cargo spaces in order to be carried into orbit by space shuttles [6]. Origami has also been applied to design automobile airbags that can fully inflate within a few milliseconds and stop rapidly-accelerating bodies [7]. Another example of origami inspired engineering is an origami heart stent that can be compressed into a small tube so that it can travel through the blood stream to a location where it unfolds and prevents heart failure [8]. In addition, origami folding techniques are used in biomedical applications such as, generation of 3D cell-laden microstructures [9] and construction of self-assembling DNA nanostructures [10]. Recently, a crawling robot which can fold itself was developed [11] thereby demonstrating a practical process for creating self-assembling machines by means of planar materials and origami folding.

With the ever-increasing demand of wireless communications, there is a great need for efficient designs of electromagnetic systems. Reconfigurable electromagnetic systems are very useful because such designs can provide multi-functionality and support different services [12-14]. The geometrical topology of an electromagnetic element is very important as it determines the element's RF performance characteristics. Various complex geometrical designs have been used in electromagnetic systems to develop components with enhanced performance and unique capabilities such as, fractal antennas [15]. Fractal antennas can obtain a radiation pattern and input impedance similar to a longer antenna, and yet take up less area due to their efficient space filling properties.

Airborne and spaceborne structures, e.g., nano-satellites or satellites, require antennas that are miniaturized, since space in such structures is very limited [16-18]. Therefore, it is very important to determine how large antennas and antenna arrays can optimally fold in order to fit in compact storage/launching compartments. Dish reflector antennas are widely used on satellites [19-20]. For example, a deployable reflector antenna with a diameter of 22 m was designed in [19]. Even though such antennas are deployable their base and metal dish significantly increase their weight and these designs are expensive and difficult to scale down to the size required for satellites. Other designs such as, patch antenna arrays [21-22], have also been proposed, and researchers have attempted to find a compromise between acceptable gain and proper size. Origami geometries have significant advantages for launch-and-carry applications where antennas need to fold in order to miniaturize their size during launch, and unfold in order to operate after the platform has reached orbit [23-25]. Also, reconfigurable antennas are preferred in airborne and

spaceborne systems as they can support multiple services by reconfiguring their operation (i.e., polarization, far-field radiation pattern, and frequency) [26-27].

1.2 Research Objectives and Contributions

Previous work has been performed on reconfigurable electromagnetic systems. However, there is limited research on how to design electromagnetic structures based on flexible foldable substrates. Therefore, this dissertation mainly addresses four research contents: (1) design proper 2-D/3-D structures for origami reconfigurable electromagnetic systems; (2) design analytical electromagnetic models that can predict the performance of foldable structures; (3) investigate manufacturing of antenna elements on foldable flexible substrates; and (4) develop actuation mechanisms suitable for autonomous reconfiguration of origami electromagnetic systems.

Reconfigurable electromagnetic devices offer the following advantages: compact size, reconfigurable performance in terms of radiation pattern and gain, and frequency of operation. Also, origami electromagnetic systems can have a significant impact on spaceborne and nano-satellite applications. Given the size and shape of a large antenna or antenna array, it is very important to determine whether and how it can be folded to fit in a compact storage/launching compartment. In addition, our research will lead to minimization of the number of antennas on spaceborne and airborne structures by developing suitable origami topologies that can reconfigure themselves thereby providing real-time adjustability and serving different applications.

The primary purpose of this research is to derive rigorous and integrated Mathematical-Computational-Electromagnetic models of origami geometries in order to

study and develop novel foldable, energy autonomous and self-deployable electromagnetic systems with multi-band and folding-dependent operation. In order to make a mathematical model be useful for origami electromagnetic systems, it will have to: (1) be general enough to model the foldability of two and three-dimensional objects, (2) allow at least some control over rigid foldability of the designs, and (3) be computationally efficient.

1.3 Methodology

To generalize the three-dimensional deployable structures, we need to consider, not only the initial and final folded state, but also the process of transitioning between them. For that purpose, we need to specify a sequence of folding/unfolding steps, each of which is reachable by a simple fold from the previous, so that the whole sequence can actually be realized by the folding process. Rigidity imposes relatively tight constraints on the design, however, if we are using thin layers of metal on a flexible surface, it may not be necessary to require strict rigidity.

In order to design and realize the origami electromagnetic systems, analytical as well as computational methods will be used in this research. The integration of origami design software with electromagnetic software will be explored. Also, full-wave electromagnetic simulation software, such as, ANSYS HFSS will be used. In order to derive the formulas to generate the 2-D origami pattern, analysis will be performed with mathematical tools, such as, Matlab and Mathematica.

Prototype models of origami electromagnetic systems will be developed and tested. Also, some models will be fabricated using 3-D printing to analyze whether designs are suitable for origami structures. The electromagnetic performance of each design will be

calculated using electromagnetic software. In order to improve the folding and unfolding performance, different materials with different thickness will be tested for the origami base structure. Prototypes will be made by attaching conductive layers on different origami base structures. Technologies, such as, PCB prototyping will be used to find the optimum process for manufacturing the origami antennas. Finally, measurements will be conducted to verify the performance of the designs using a vector network analyzer and an anechoic chamber.

1.4 Dissertation Outline

The dissertation is organized as follows: Chapter 2 reviews the existing literature related to the issues involved in origami reconfigurable electromagnetic systems. In Chapter 3, the design and performance of origami accordion structure based antennas and reflectors are presented. In Chapter 4, the origami spring structure is studied, and the origami spring based antennas and antenna arrays are developed. In Chapter 5, the mode reconfigurable origami antenna, which can morph from a dipole to a conical spiral antenna, is presented. In Chapter 6, the origami based segmented helical antenna, which can switch the sense of polarization between LHCP and RHCP, are designed and analyzed. Finally, Chapter 7 provides the conclusions of this dissertation. Suggestions for future research are also discussed in this chapter.

CHAPTER 2

BACKGROUND AND RELATED WORK

In this chapter, the existing literature related to the issues involved in origami reconfigurable electromagnetic systems is reviewed. Origami art is briefly introduced in Section 2.1. The recent work of reconfigurable electromagnetic devices is discussed in Section 2.2. The related designs of origami structures used in electromagnetic systems are reviewed in Section 2.3.

2.1 Origami Art

Origami is the art of paper folding. Origami is composed from two Japanese words: *oru* which means folding, and *kami* which means paper. Art historians believe that Japanese origami was invented sometimes in the centuries after Buddhist monks carried paper to Japan during the 6th century [28]. Abstract folded paper forms were used in religious ceremonies over many years, and by the 1600s, decorative shapes that we recognize today, such as, the traditional crane, were being folded [29]. In modern usage, the word “origami” is used as an inclusive term for all folding practices, regardless of their culture of origin. The goal is to transform a flat sheet square of paper into a finished sculpture through folding and sculpting techniques. Modern origami practitioners generally discourage the use of cuts, glue, or markings on the paper [30].

Almost any laminar (flat) material can be used for folding; the only requirement is that it should hold a crease. Artistic origami uses paper which is an elastic material that prefers to be flat, but other materials are more useful for engineering. There are two categories of origami: rigidly foldable origami, where stiff panels are folded along hinged

creases and creases are geodesically fixed within the paper [31]; and non-rigidly-foldable origami, where deformation is allowed on each individual face and/or vertices and creases can move within the paper [32]. Advances in computer science, number theory, and computational geometry have paved the way for powerful new analysis and design techniques, which now extend far beyond the art itself [33].

To design an origami model, it is necessary to determine the crease pattern that will dictate the folds necessary to achieve the desired 3D form. An origami base is the first step in the folding process, and it is the foundation of every design. Several algorithms have been developed to design efficient crease patterns to fold bases [34-35].

2.2 Reconfigurable Electromagnetic Devices

Reconfigurable antennas, filters, reflectors, antenna arrays, frequency selective surfaces, and other radio-frequency (RF) devices has been developed [36], because they have unique advantages over standard devices, such as band-switching and frequency tuning [37-44], beam-steering [45-47], polarization adjustment [52-55], and many other capabilities which are needed in future wireless communication systems.

There are many ways to design reconfigurable electromagnetic devices. Intrinsic device properties such as capacitances and inductances as well as switching times, actuation waveforms, on/off resistances and power handling are the primary concerns when choosing a switching or tuning device for a specific application. The reconfigurability of filters and antennas can be accommodated by use of PIN diodes or varactors [37-42]. The varactors are usually located at the end of microstrip stubs [37], in slots [38] or along the current path [39], working as controlling circuits. PIN diodes are used as switches to

control the effective electrical length of antennas [40-42]. Microelectromechanical system (MEM) switches also enable the development of reconfigurable antennas [43-45], frequency selective surfaces [46-47] and antenna arrays [48-49]. In [50-51], an optical controlled switch was used for a reconfigurable antenna design, the switch is preferred over electronically controlled switches because it provides perfect isolation between the controlling optical signal and controlled microwave signal even at high switching speeds and high microwave frequencies. Reconfigurable RF circuits can be accomplished using variable capacitors to tune the resonance frequencies of LC circuits with small parasitic capacitances and a high Q factor [52-54]. In [55-57], different designs of slots are applied on the antenna or the ground structure to realize the polarization reconfigurability. The polarization and operating frequency band of the antennas and reflector arrays can be also changed through fluidic movement [58-60]. The transistors [61], relays [62], and even dielectric structures [63-64] are used in the design of reconfigurable electromagnetic devices.

Also, some reconfigurable antennas are designed by directly changing the antenna geometry using mechanisms. In [65], a tunable helical antenna is presented, which uses a shape memory alloy placed in parallel with the antenna to control the antenna height. However, such antennas exhibit geometrical distortion (i.e., they do not retain their canonical shape, such as, a helix) when they are stretched or collapsed and they cannot be efficiently compacted. A tape spring antenna, which can work in both deployable and stowed states, was proposed in [66]. This antenna deploys along a tape line and, therefore, it can only be designed as a dipole or a monopole antenna. In [67], a monopole antenna

transforms to a patch antenna with a light-activated hinge, but such hinges cannot guarantee continuity of the antenna element.

2.3 Origami Structures Used in Electromagnetic Systems

Limited previous work has been performed on origami electromagnetic structures. A foldable array structure for energy harvesting was successfully launched and deployed based on the Miura-origami design, which could be folded rigidly without bending any of the quadrilaterals in the crease pattern [68-69]. Concepts of thin shell structures and pantographs have been used as basis for the development of origami antennas, such as conical log-spiral antennas [70]. A foldable frequency selective surface was also introduced in [71], which comprises of periodic elements arranged in an origami-like fashion on a dielectric sheet. By folding and unfolding the FSS, the resonance frequency shifts. Folding also has been utilized to form 3D antennas by printing antenna elements on paper, and then folding the paper into cubic structures [72]; a 3-D dipole was designed for wireless sensor nodes application in [73]. However, these 3D antennas only operate at their folded states and cannot reconfigure themselves. A UHF quadrifilar helical antenna, supported by helical arms of S2 glass fiber reinforced epoxy, was designed in [74]. The package volume of this antenna is about 30% of the expanded structure, which makes it a good candidate for CubeSat applications. In addition, other electromagnetic elements such as, 2-D and 3-D Strongly Coupled Magnetic Resonators have been developed using folding for wireless power transfer systems [75].

Recently, the 3-D printing technique with liquid metal alloy (LMA) material has attracted a lot of attention, which features a great potential in reconfigurable electronics

due to its non-poisonous, high-conductivity, flow-able and stretchable properties [76]. A 3-D flexible inverted-F antenna for wearable applications is presented in [77]. The micro-channels are printed to delimit the shape of the conductive part of the antenna, and the antenna sensitivity to the bending is strongly reduced. In [78], a 3-D printed antenna “tree” was presented that can integrate virtually any antenna and is capable to reconfigure in frequency, radiation pattern and polarization by filling/unfilling the LMA or folding/unfolding the origami scaffolding structure. This approach can be realized only through the recent developments in flexible 3D printing technologies that enable the quick prototyping of on-demand 3D foldable/compressible antennas.

Software for designing origami geometries has also developed. For example, Tree Maker can compute the full crease pattern for a stick figure [79]. The crease pattern can be folded into corner, edge, or middle flaps. A rigid origami simulation software is presented in [80], which can calculate the kinematics of rigid origami from general crease pattern. In [81], simulation software for reconfigurable antennas was discussed with particular focus on the modeling of switches. However, no methodologies have been presented for the design of reconfigurable origami folding/unfolding electromagnetic structures yet.

CHAPTER 3

ORIGAMI ACCORDION STRUCTURE BASED ANTENNA AND REFLECTOR

In this chapter, the design of 3-D origami accordion structure based antenna and reflector are studied. The origami accordion structure is described in Section 3.1. The antennas built on an accordion paper pattern are presented in Section 3.2 and 3.3, which can be folded and unfolded to different heights thereby providing reconfigurable antenna performance in terms of frequency of operation and gain, [82-83]. The origami accordion reflector is discussed in Section 3.4. This novel antenna is suitable for airborne and spaceborne structures as well as payloads as it can collapse during launch (thereby minimizing its size) and expand after it has reached orbit. In practice, the height of such accordion antennas can be controlled by a non-conductive telescoping mechanism.

3.1 Origami Accordion Structure

The accordion folded sheet pattern and its variants have been widely applied to the design of art [84], objects [85], and architectural structures [86]. The origami accordion structure is widely used in our lives due to its collapsible and flexible nature, and it has a large internal space generated from a thin sheet.

Figure 3.1 shows the geometry of an accordion structure. This model contains 6 levels. All the odd levels (counted from the bottom) are parallel, and so are the even levels. The height, H , and the distance, h , between levels can be precisely controlled by folding and unfolding the accordion structure. When this structure is totally folded, the position of every level is close to horizontal. When the structure is unfolded, all levels are inclined and the larger the ratio of H/h is, the larger θ is.

In Figure 3.2, the metal layer is put along one level of the accordion structure and after a certain length, jump to another level, and in this way, a 3-D metal structure for antenna application is constructed. This means that many different antennas can be built on one accordion base. It should be noted that since the base material of the accordion is dielectric, even when the antenna is completely folded (i.e., collapsed), the metal elements on the different levels will be isolated from each other. Another important advantage of this accordion structure is that it is hollow. Therefore, it provides space for other components, such as, sensor circuits or height controllers.

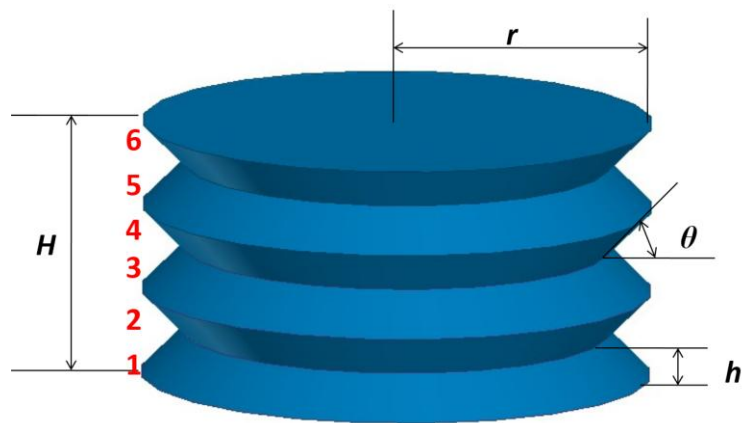


Figure 3.1. Accordion structure.

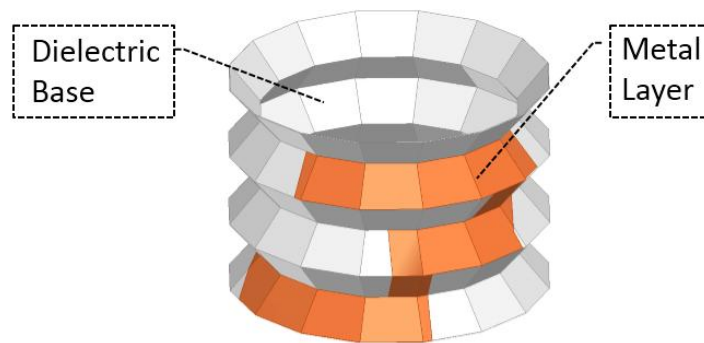


Figure 3.2. Metal strip on the accordion structure base.

The origami accordion structure has many variants. In this chapter, the accordion lantern variant is studied. Figure 3.3 shows the steps to make this variant accordion structure by folding a piece of flat paper or other dielectric material. First, proper creases on the flat paper are made. The number of creases and the crease directions depend on the size of the accordion structure. Then the paper is folded cylindrically, and the two sides are connected together as shown in Figure 3.3(b).

The rectangle in Figure 3.4(a) is the rectangular paper unit before folding. Figure 3.4(b) shows the shape of a paper unit after it is folded along the creases. It is seen that the two short sides of the paper unit are curved with two different central angles. Figure 3.4(c) is the front view of the paper unit, and it shows that the central angle α is greater than the angle β . Although, the two arcs have the same length, the exterior circumference of the accordion is bigger than the interior circumference.

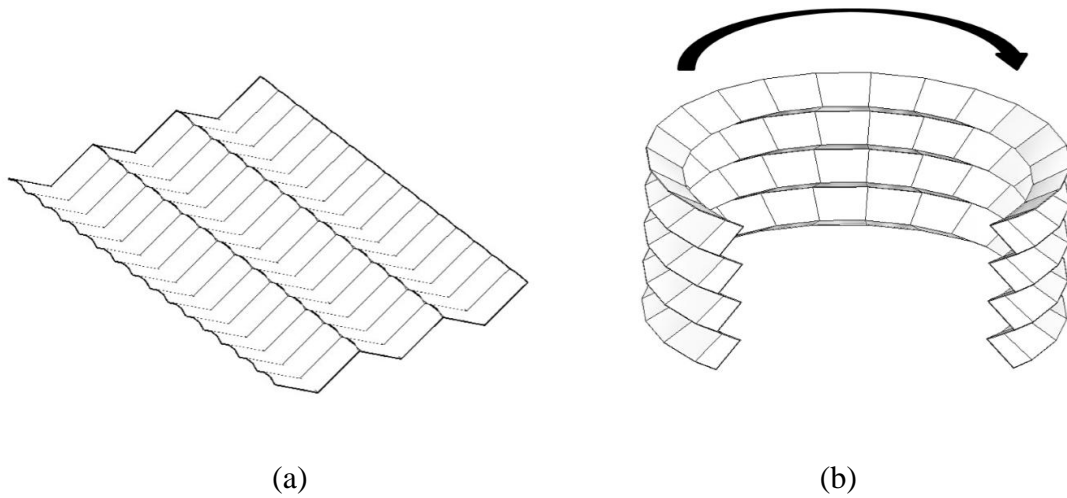


Figure 3.3. (a) Creased base material. (b) Folding the base material.

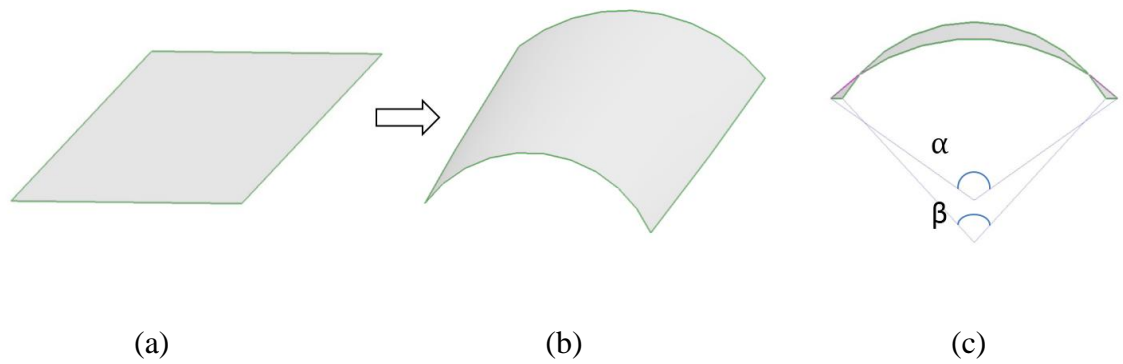


Figure 3.4. (a) Paper unit before folding. (b) Folded paper unit. (c) Front view of folded paper unit.

3.2 9-Level Origami Accordion Antenna

Here, an accordion antenna model is designed based on the structure illustrated in Figure 3.2. The geometry of this antenna is shown in Figure 3.5. The metal strip goes along the first level of the accordion paper base. After a quarter round, it goes to the next odd level. There are 9 odd levels in total. The metal material, which was used to build the antenna, is copper. The thickness of the copper strip is 0.1 mm, and its width is 7 mm. The radius, r , which is the distance between the central axis and the edge of every level, is 50 mm. The antenna is fed using a 50-Ohm coax.

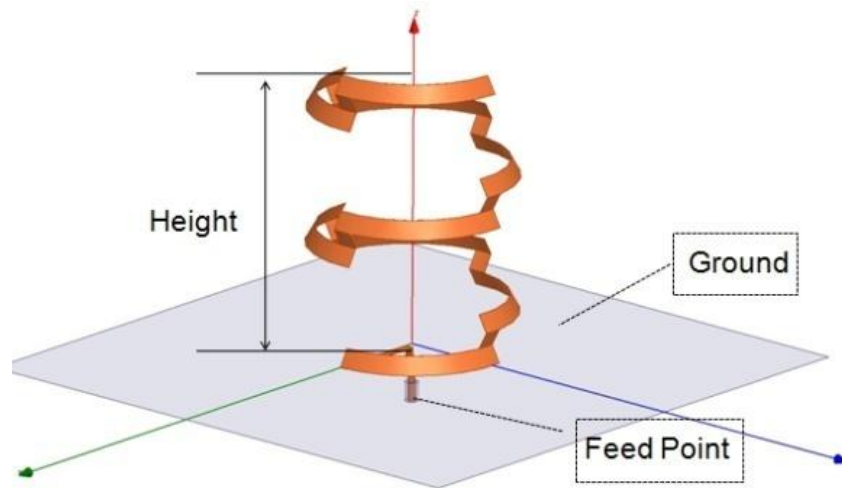
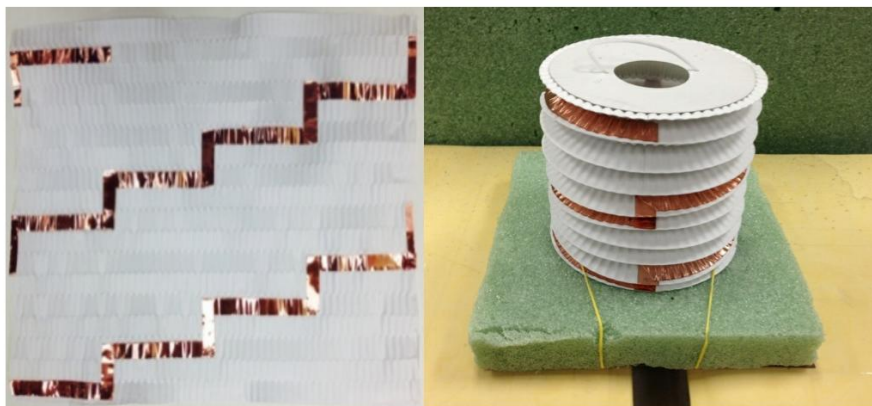


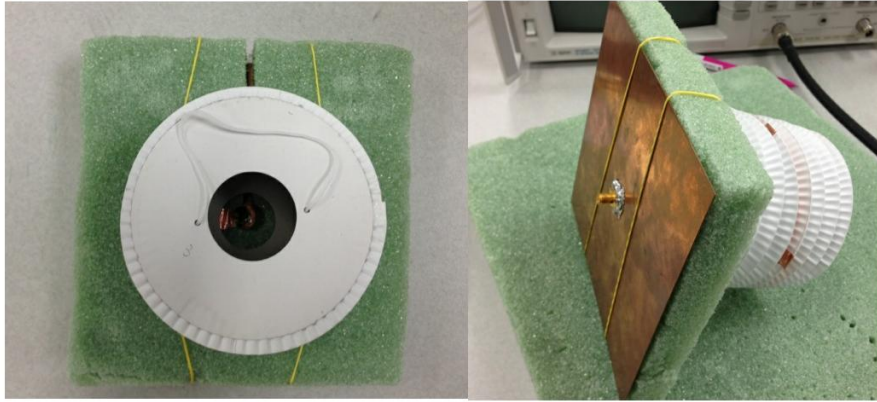
Figure 3.5. 9-Level origami accordion antenna model in ANSYS HFSS.

A real model is also manufactured to validate the simulation results. Figure 3.6(a) shows the flat creased paper with the copper strip on it before it is folded. The prototype of the antenna is shown in Figure 3.6(b). A 160 mm by 160 mm copper sheet was used as the ground with a 20 mm thick polystyrene foam layer between the antenna and the copper sheet.



(a)

(b)

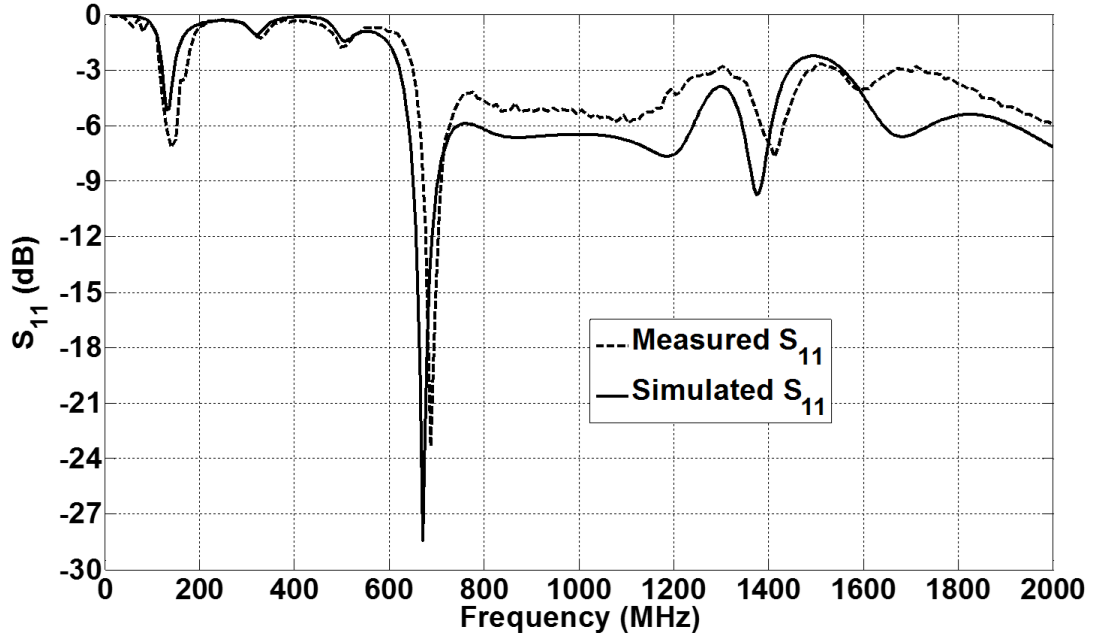


(c)

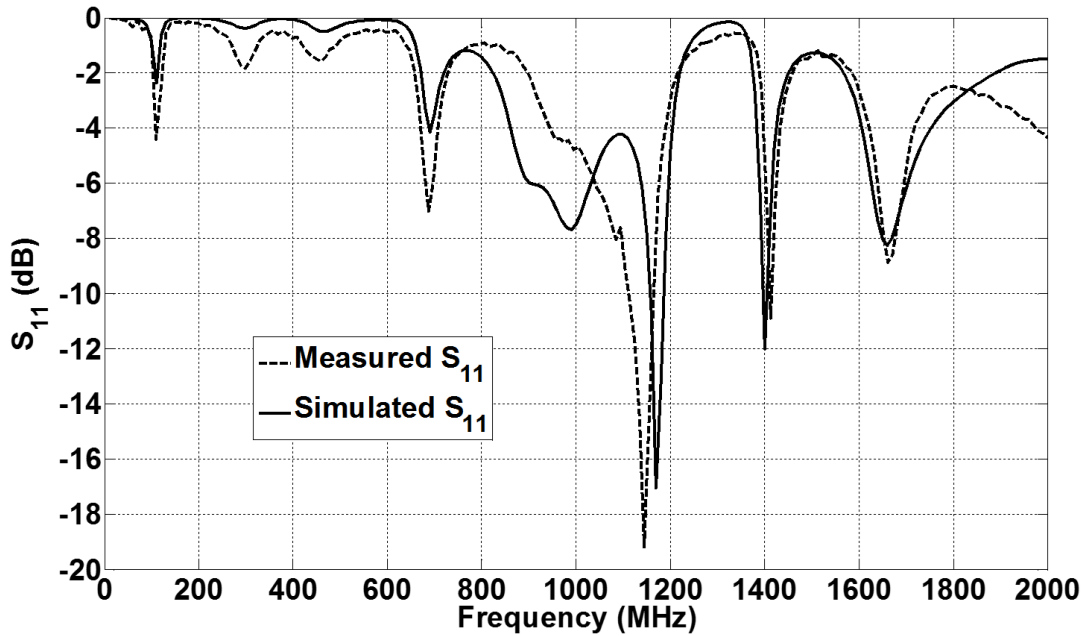
(d)

Figure 3.6. (a) Flat paper with copper strip. (b) Side view, (c) top view and (d) bottom view of the manufactured origami accordion antenna.

The graphs in Figure 3.7 show the simulated and measured reflection coefficient of this antenna at different heights. The simulation results are from ANSYS HFSS. The measurements were obtained using a vector network analyzer. Figure 3.7 (a) shows the measurements and simulation results of S_{11} when the height of antenna is 160 mm (unfolded state). Figure 3.7(b) shows the measurements and simulation results of S_{11} when the height of antenna is 40mm (folded state). Figure 3.7 shows that the resonances of this accordion antenna change when it folds or unfolds thereby providing a reconfigurable performance. Therefore, this origami antenna is a spatially reconfigurable antenna.



(a)



(b)

Figure 3.7. S_{11} of the accordion antenna at (a) the unfolded state, 160 mm height, and (b) the folded state, 40 mm height.

Figure 3.8 compares the simulated and measured normalized radiation pattern for the elevation plane of the antenna. Figure 3.8(a) shows the pattern at 1400 MHz for a height

of 40mm, and Figure 3.8(b) shows the pattern at 670 MHz for a height of 160mm. The measurements of the gain were conducted in an anechoic chamber. The simulated and measured gain data illustrate that this antenna is directional, and the maximum gain is along the central axis (z direction). The shape of the pattern is similar to the one of a helical antenna working at axial mode.

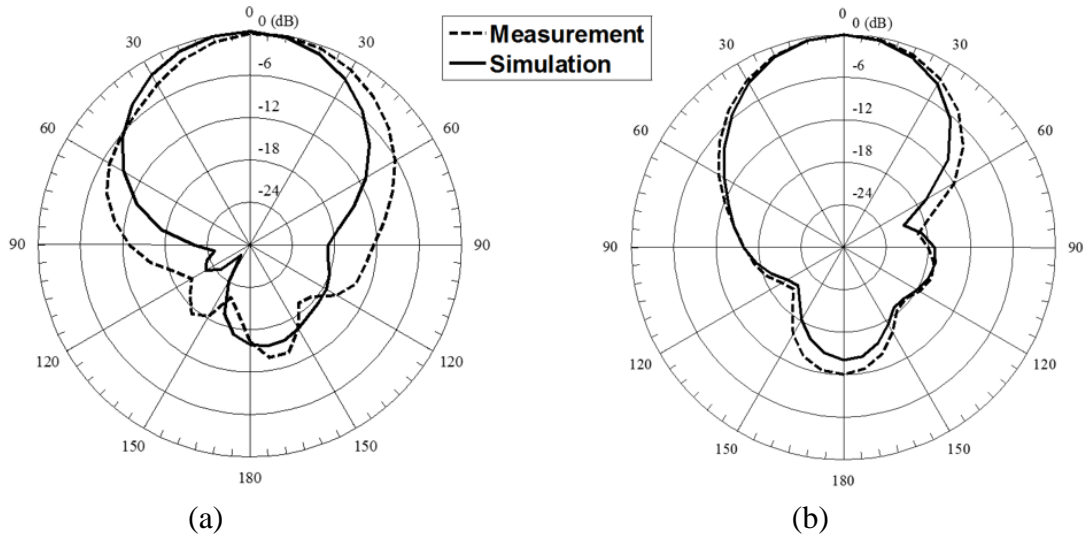
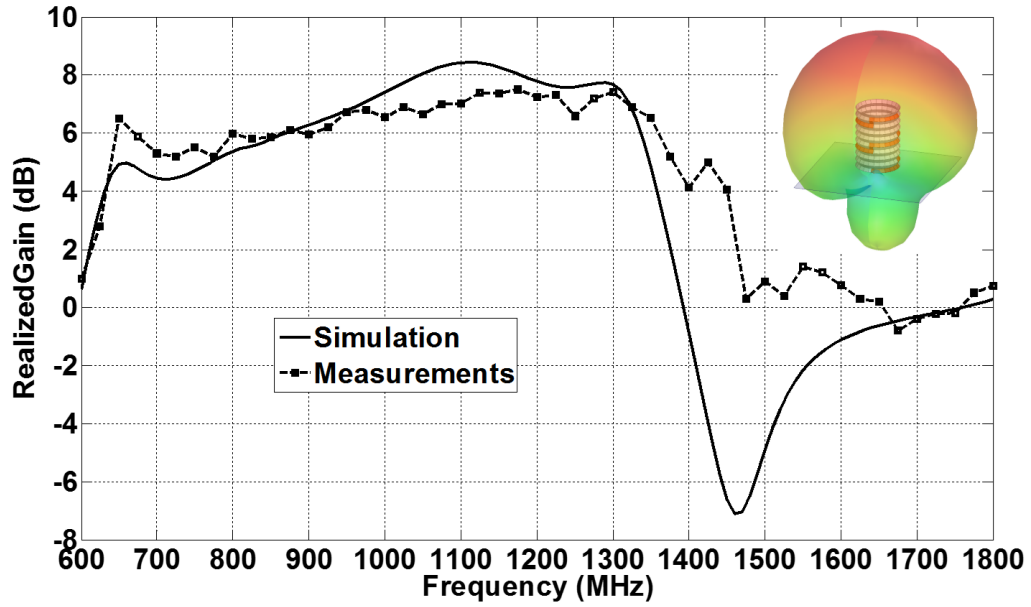
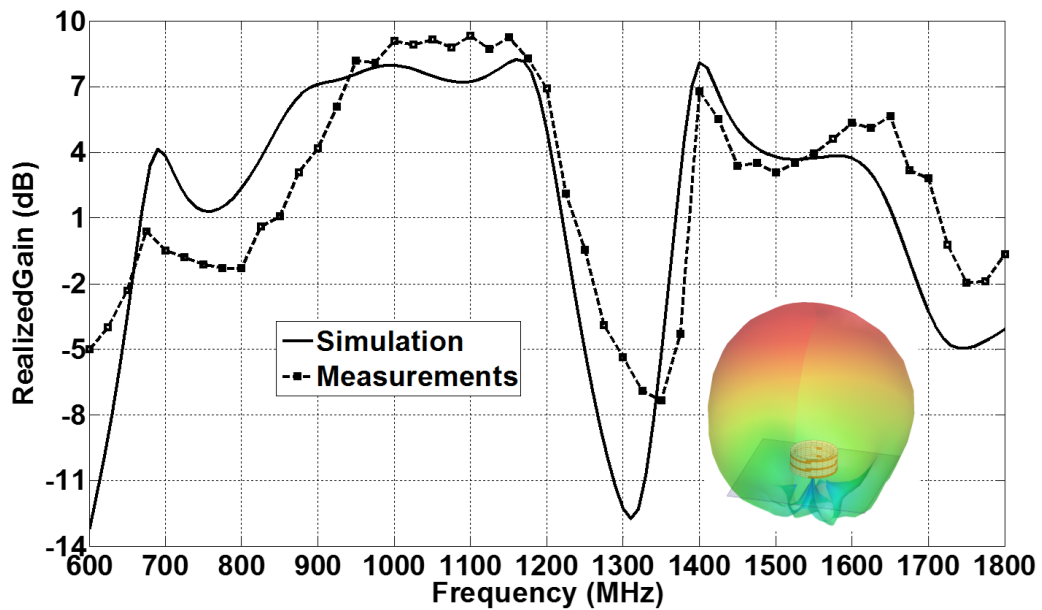


Figure 3.8. Simulated and measured normalized radiation pattern for elevation plane for $\varphi = 0^\circ$ at: (a) unfolded state, and (b) folded state.

Figure 3.9 shows the simulated and measured realized gain along the z direction of the accordion antenna versus frequency at different heights. It can be seen from the results, that the unfolded state has significantly larger realized gain at 650 MHz and 1300 MHz. However, at 1400 MHz, the folded state achieves a larger realized gain. Therefore, this illustrates again that this origami antenna is a spatially reconfigurable antenna that based on its height provides optimal gain at different frequencies.



(a)



(b)

Figure 3.9. Realized gain at (a) 160 mm height and (b) 40 mm height.

3.3 Tunable Origami Accordion Antenna

As mentioned in the previous section, many different antennas with different characteristics can be developed based on accordion origami structures. In this section, a

continuously tunable accordion antenna model is developed. Figure 3.10 shows the geometry of this antenna. The metal strip goes along the first level of the accordion base. After a whole round, it goes to the next odd level. There are 3 odd levels in total. The metal material is copper. The thickness of the copper strip is 0.1 mm and the width is 5 mm. The radius, r , which is the distance between the central axis and the edge of every level, is 20 mm.

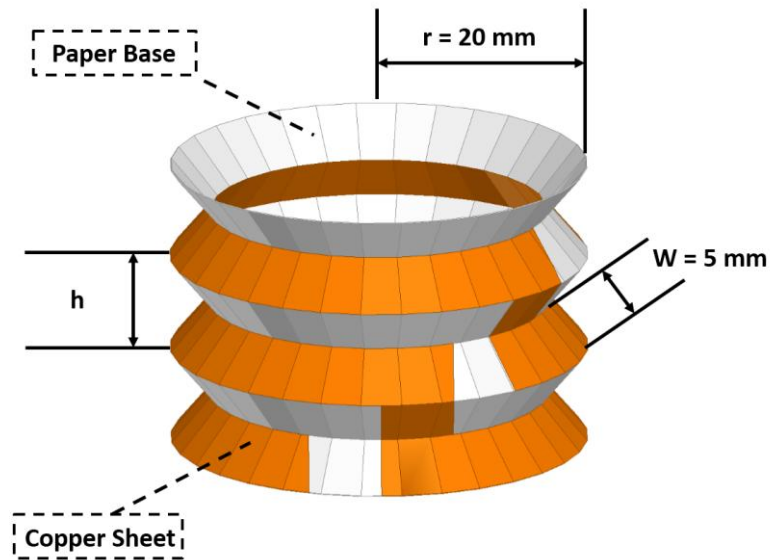


Figure 3.10. Tunable origami accordion antenna model.

Figure 3.11(a) shows the simulated accordion antenna model for three different heights. The height of each level, h , for the 3 states illustrated in Figure 3.10 is 10 mm, 6mm and 2 mm, respectively. In this case, it was not easy to make prototypes of this antenna using paper without the development of special tooling. Therefore, in order to validate our simulation results, one prototype was built for each of the cases of Figure 3.11(a) using a 3D printer. The thickness of the origami accordion base was 1 mm. The material used for the 3D printing is Polylactic Acid with a dielectric constant of 3.1. Figure

3.11(b) shows the manufactured prototypes of the accordion antenna for the three different heights.

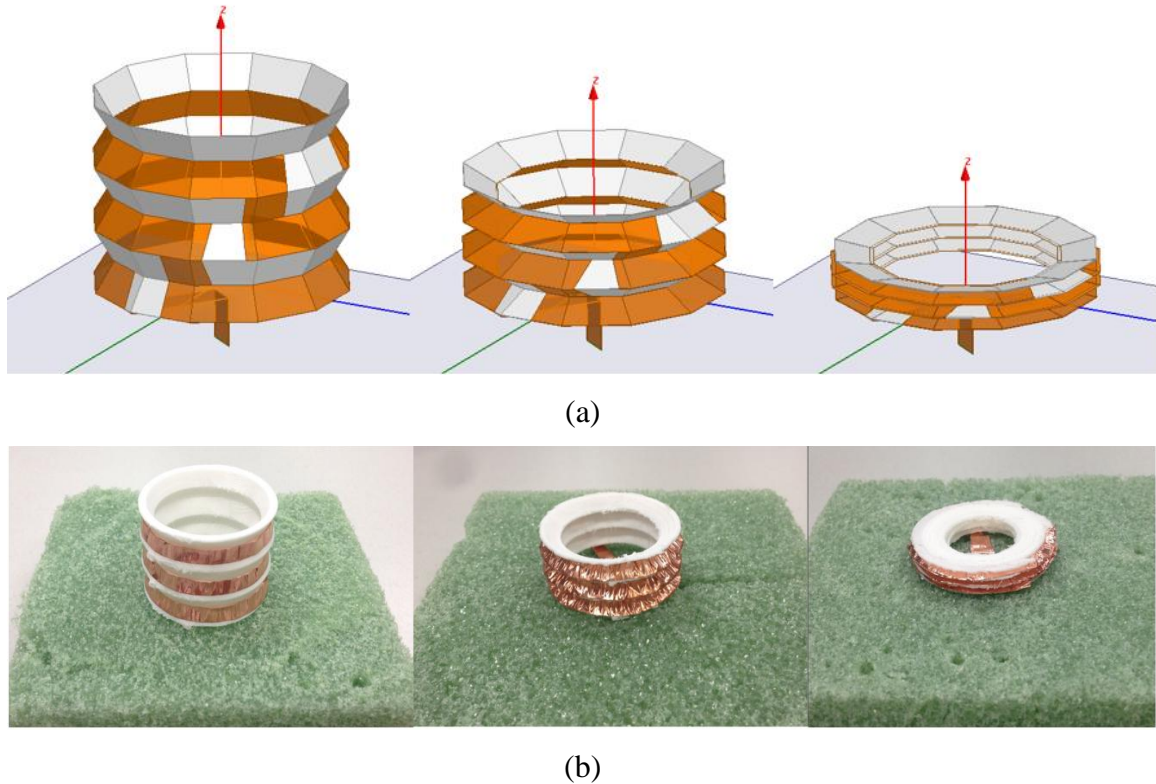
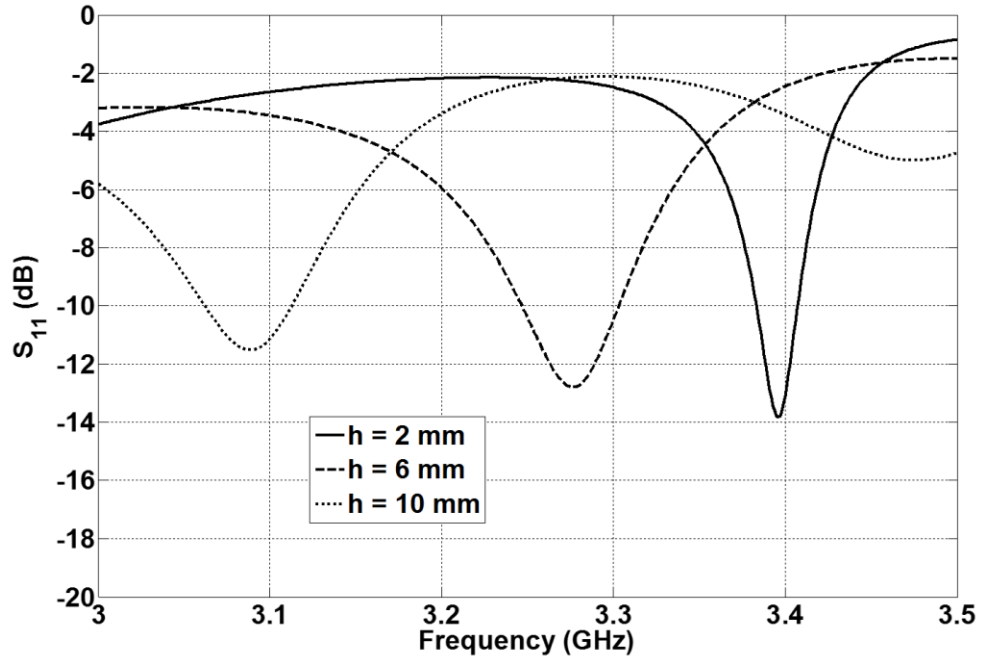
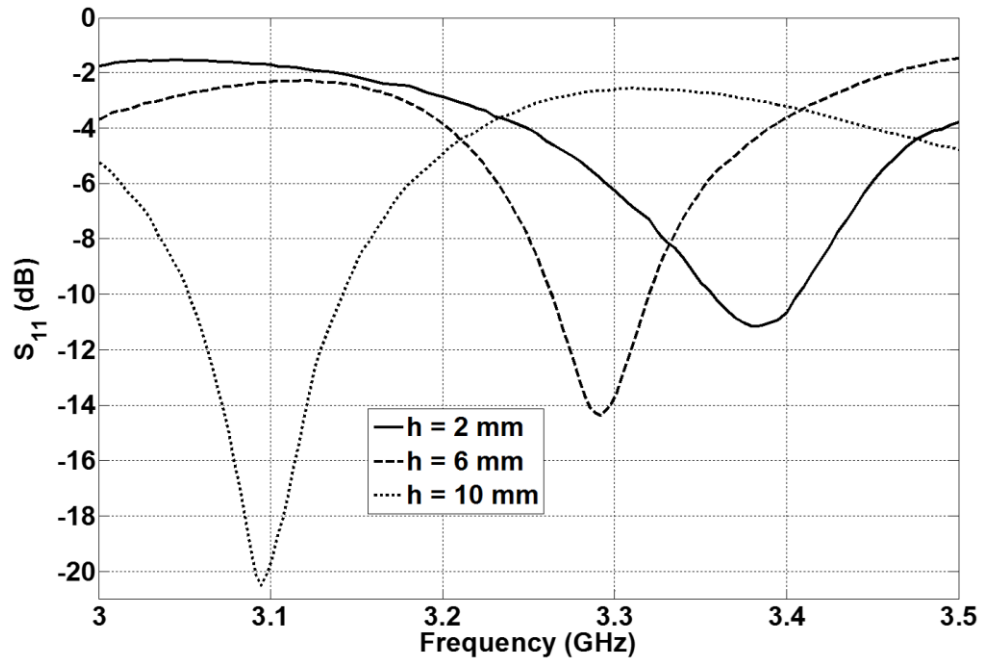


Figure 3.11. (a) Simulation models of tunable accordion antenna for different heights. (b) Prototypes of tunable accordion antenna for different heights.

Figure 3.12 compares the simulated and measured reflection coefficient of this antenna for different heights. The simulation results were obtained using ANSYS HFSS, and illustrate that the antenna operating frequencies shift from 3.4 GHz down to 3.09 GHz when the height, h , increases from 2mm to 10mm. The similar shift of the antenna operating frequencies occurs in the measurements. It should be pointed out that the measured S_{11} is worse at the $h = 2$ mm state than the other two states, that is because of the capacitance effect due to the adjacent copper layers and the PLA layer between them.



(a)



(b)

Figure 3.12. (a) Simulated S_{11} of the tunable accordion antenna. (b) Measured S_{11} of the tunable accordion antenna.

Figure 3.13 shows the simulated realized gain along the z direction of this accordion antenna versus frequency at different heights. These results clearly illustrate the peak

realized gain shifts continuously for different antenna heights, which also demonstrate that the operating frequency of the origami antenna is continuously tunable. Therefore, this origami antenna is a reconfigurable tunable antenna.

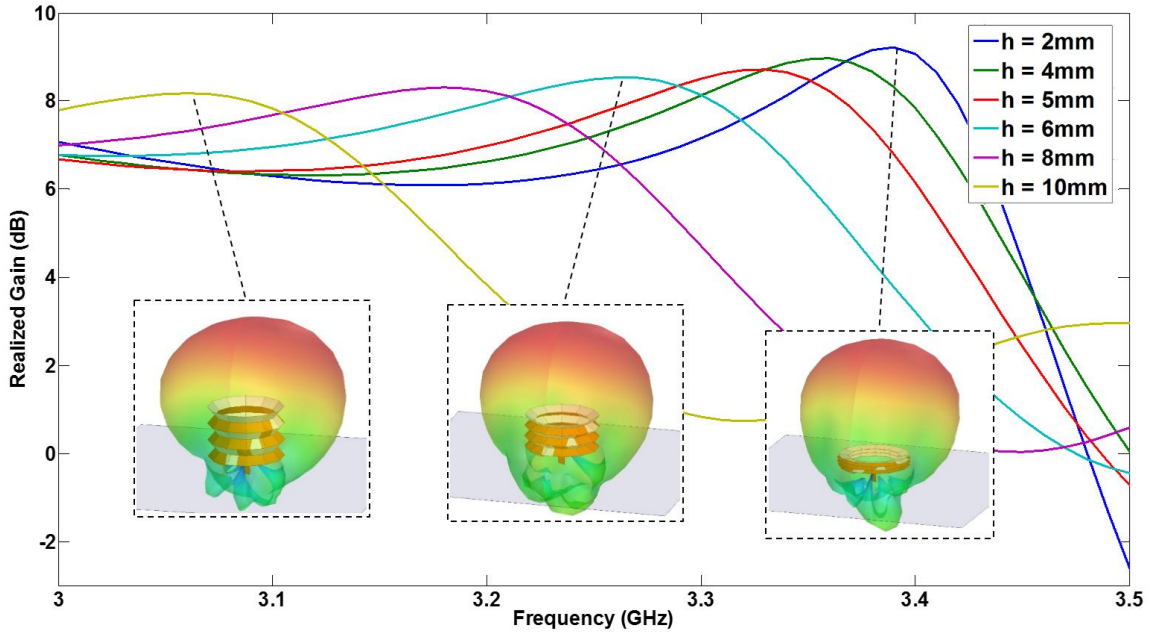
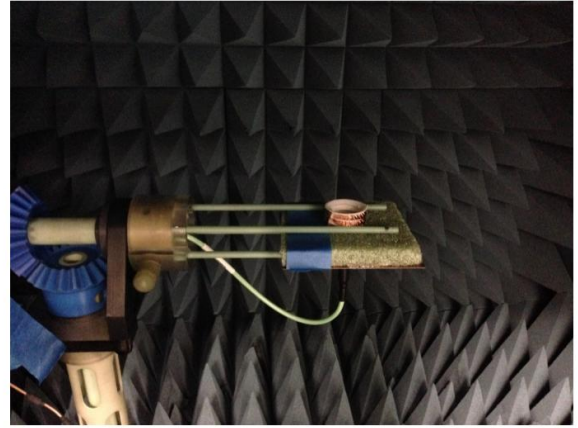
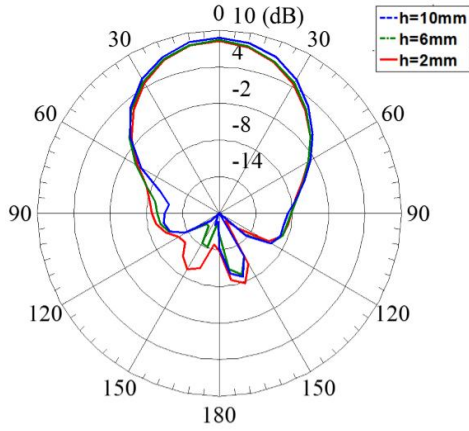


Figure 3.13. The realized gain along the central axis of the 3-level accordion antenna versus frequency when the height of each level changes from 2 mm to 10 mm.

Figure 3.14(a) shows the measured far-field radiation pattern for the elevation plane of this antenna at 3.09 GHz, 3.27 GHz and 3.4 GHz for the level-height, h , of 10 mm, 6 mm and 2mm, respectively. The measurements of the gain were conducted in an anechoic chamber as shown in Figure 3.14(b). The measurements agree well with the simulated results. It can be seen that this antenna is directional, and the peak gain is along its central axis. The measured gain along zenith is 7.03 dB, 7.53 dB and 6.87 dB for heights, h , of 10 mm, 6 mm and 2mm, respectively. The height of the reflector is mm when the antenna is at unfolded state, and the height is mm when the antenna is folded.



(a) (b)
 Figure 3.14. (a) Simulated and measured radiation pattern for elevation plane. (b) Antenna is in the anechoic chamber.

3.4 Origami Accordion Reflector

The radius of every level of the origami accordion structure presented in previous sections are identical, and the accordion has a cylindrical type of shape. The 2-D pattern for folding the accordion is a rectangular as shown in Figure 3.6(a). If we use a trapezoid 2-D pattern to fold the accordion, the radius of each level of the folded structure will be gradually increased, and the 3-D accordion will have a truncated cone shape as shown in Figure 3.15(a). The cone has a maximum diameter D_1 , and the minimum diameter is D_2 . The height of the cone is denoted as H_l , which is adjustable.

The truncated cone reflector provides higher gain for directional antennas compared to infinite ground plane, square reflector and cylindrical cup reflector [87]. The origami structure can work as a quasi-truncated cone reflector with an inner metal layer. The accordion origami antenna can be put inside the accordion reflector, as shown in Figure 3.16. The optimal height for the truncated cone reflector for helical antenna is half wavelength of the operating frequency, i.e., $H_l = 0.5\lambda$ [87]. Since the origami accordion

antenna is a reconfigurable antenna which has several operating frequencies, the height adjustable accordion structure is a good candidate for the multiband reflector.

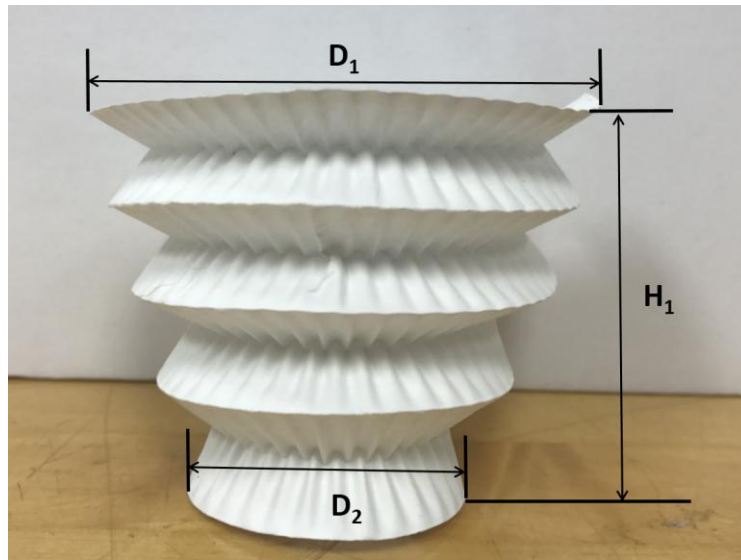


Figure 3.15. Tunable origami accordion reflector structure.

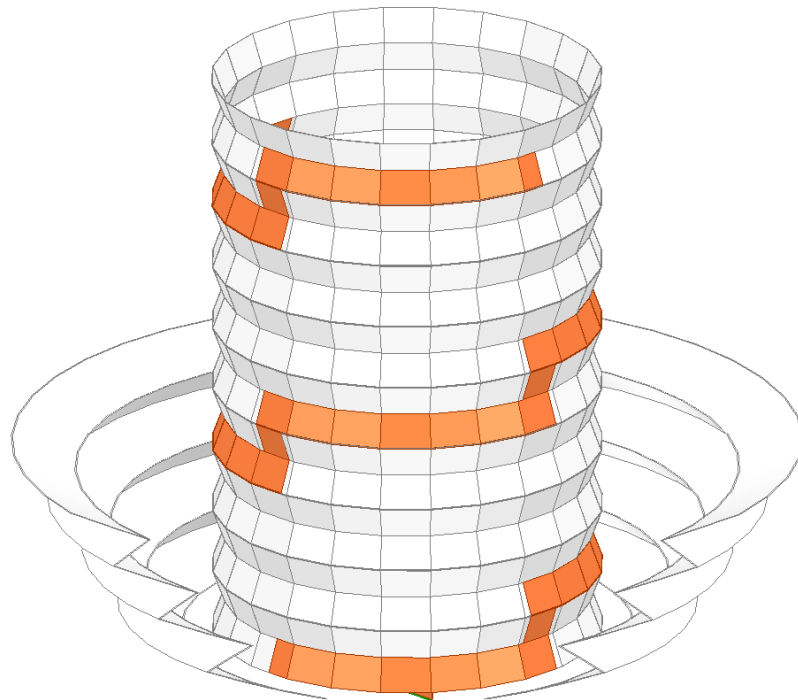


Figure 3.16. Tunable origami accordion reflector structure.

The 9-level origami accordion antenna presented in section 3.2 is used in the simulation. The accordion reflector has 4 levels. In order to make the whole design have a compact structure, the maximum and minimum diameters of the reflector are chosen as 400 mm and 110 mm, respectively. The height of the reflector, H_I , is 30 mm when the antenna is folded, and H_I is 80 mm when the antenna is unfolded. The simulated realized gain patterns of the antenna with and without the reflector is compared in Figure 3.17. From the pattern results, it can be seen that the antenna gain is improved by approximate 2 dB at both states. The results confirm that the origami accordion cone structure can work as a multiband reflector which enhances the gain of the origami accordion antenna.

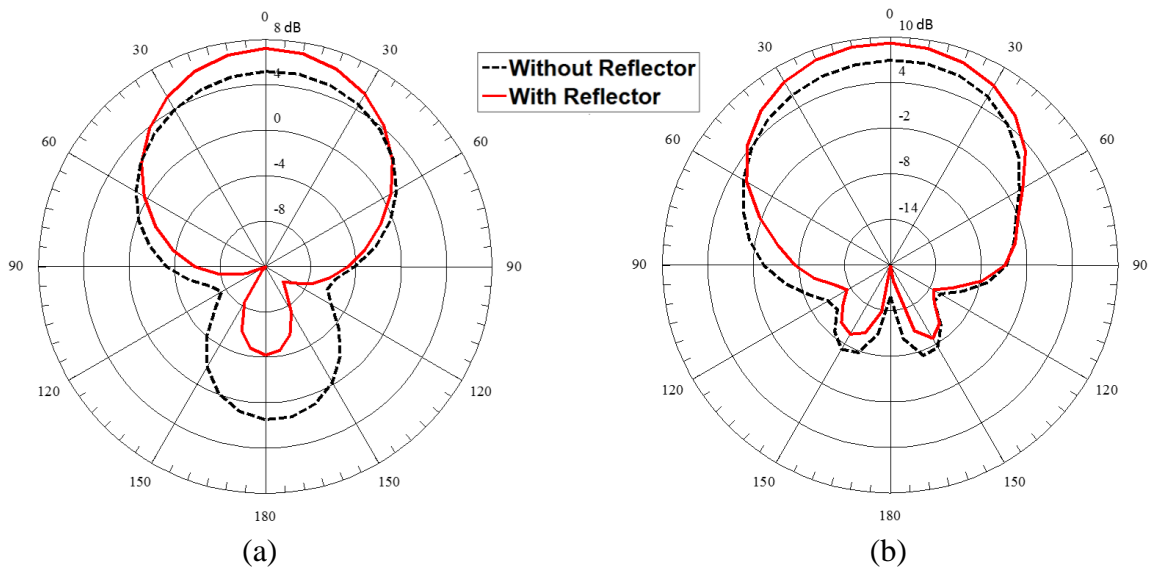


Figure 3.17. The simulated elevation radiation pattern for $\varphi = 0^\circ$ of (a) the unfolded antenna at 670 MHz, and (b) the folded antenna at 1400 MHz,.

CHAPTER 4

ORIGAMI SPRING STRUCTURE BASED ANTENNA AND ANTENNA ARRAY

In this chapter, the origami spring structure is studied for antenna and antenna array designs, and it is manufactured using dielectric materials, such as, paper. In Section 4.1, the 2-D pattern of the origami spring structure is analyzed. An operating-frequency-tunable 3D antenna based on this origami spring structure is designed in Section 4.2, which can be folded and unfolded to different heights thereby proving reconfigurable performance. An origami spring based Yagi loop antenna array is presented in Section 4.3. The whole length of the array can be controlled by a servo gripper.

4.1 Origami Spring Structure

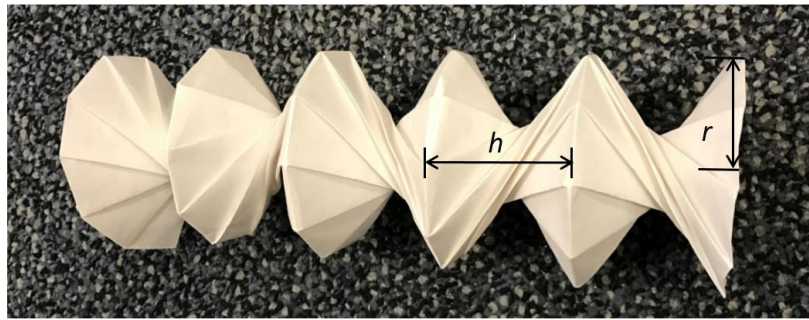
The origami spring model, shown in Figure 4.1(a), was created by Jeff Beynon [88]. When pressure is exerted on the top of this spring structure, it collapses, and it can deploy when pressure is removed. Also, the length of the whole spring body can be controlled by pressing or stretching one of its levels. In Figure 4.1(a), the height of each spring level is denoted as h , and the radius of each level is denoted as r . When the spring structure is expanded, h is enlarged while the radius r is getting smaller.

The whole 3-D structure can be folded from a piece of rectangular flat paper, as shown in Figure 4.1(b). The solid lines are valley-folds. The long dimension of the paper is folded into 4ths, and the short dimension is folded into 12ths. After the folding, we have 48 small rectangles. Then fold each rectangle diagonally in half along the dash lines, which are mountain-folds. The paper will now be rolled and twisted until it forms the collapsible

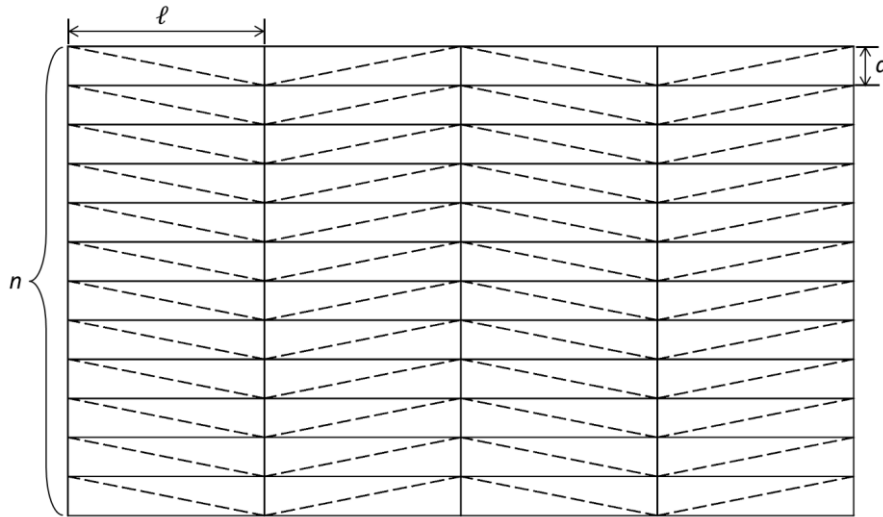
model, which has 4 levels of the spring structure, and each level is formed by 12 twisted rectangles.

The length of each rectangle unit is denoted as ℓ , and the width of each rectangle unit is denoted as a . n is the number of rectangle units of each column. We derived the following equation which must be satisfied in order to fold the rectangular sheet into an origami spring structure:

$$\pi \cdot (\ell^2 + a^2)^{\frac{1}{2}} \approx n \cdot a. \quad (4.1)$$



(a)



(b)

Figure 4.1. (a) Origami spring paper structure. (b) Creased paper for folding origami spring.

Other dielectric materials besides paper are tested for the folding of origami spring. From our tests results, both the Kapton[®] film and Polycarbonate plastic film with 1-5 mil thickness work well for the origami spring folding, and they exhibit similar performance as sketching paper. In Figure 4.2, an origami spring folded with 3-mil thick Polycarbonate plastic paper is presented.

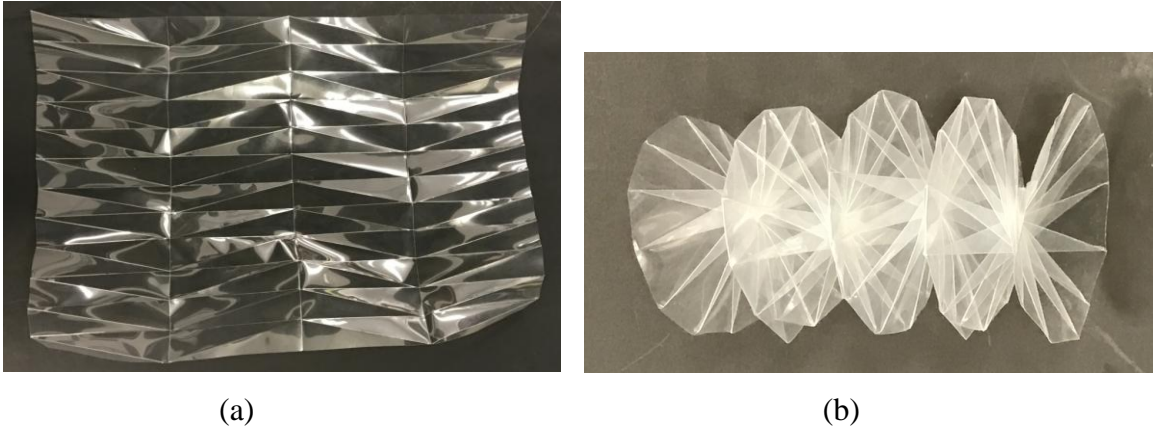


Figure 4.2. (a) Creased 3-mil thick Polycarbonate plastic film for folding origami spring. (b) Folded origami spring with 3-mil thick Polycarbonate plastic film.

4.2 Tunable UHF Origami Spring Antenna with Actuation System

In this section, a tunable origami spring antenna with directional radiation pattern is designed. Because of its natural property to expand and collapse, the total height of the origami spring antennas can be changed thereby providing reconfigurable performance. The antenna has four levels and can be folded and unfolded by an actuation system. The operating frequency of the antenna shifts continuously from 1.1 to 1.4 GHz. The dimensions of the 2-D spring pattern are selected based on the formula (4.1). The values of the ℓ , a , n are 90 mm, 20 mm, 12, respectively.

Figure 4.3 shows the copper layer on the 360 mm by 240 mm rectangular creased paper base, and the 50 ohms input excitation is from one side of the conductor. A 6 mm

wide copper strip is put along the edge of first level from the upper right corner, after crossing 11 rectangles, the tape goes along a diagonal line to the position which lies opposite on the edge of the second level. Repeat this process until the 4-levels of the pattern are finished. There will be a 3-D origami antenna after the paper is folded as shown in Figure 4.4.

In Figure 4.4, h is the height of each spring level, and the total height H of this antenna design equals $4 \times h$. The radius of each level is denoted as r . When h is enlarged, the radius r is getting smaller. The equivalent model of this origami antenna are four loops connected in parallel. The perimeter of the loop is approximately one wavelength of the operating frequency. The operating frequency shifts via changing the total height of the origami spring base.

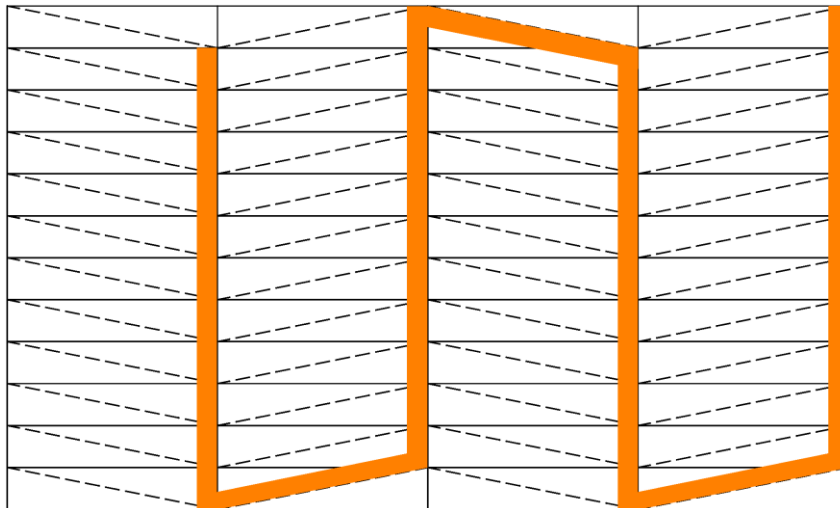


Figure 4.3. Copper layer on the origami spring paper base.

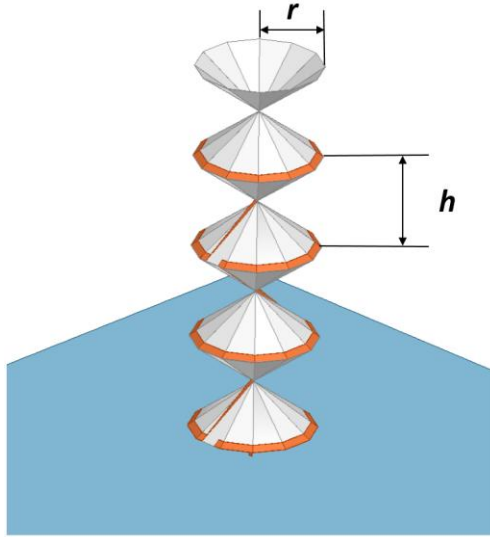


Figure 4.4. Simulation model of the origami spring antenna in ANSYS HFSS.

The graph in Figure 4.5 shows the simulated reflection coefficient of this antenna at different states. From the simulation results, it can be found that the lowest S_{11} peak shifts from 1.09 GHz to 1.39 GHz when the height h changes from 16 mm to 36 mm. Figure 4.6 shows the simulated elevation radiation pattern at the lowest S_{11} peak in the operating frequency band with different height h . The antenna exhibits directional gain above 9 dB towards the positive z direction.

This antenna is right-handed circularly polarized. The simulated axial ratio is below 3 dB at the lowest S_{11} peak in the operating frequency band, as shown in Figure 4.7. From the simulation results, we found that the sense of the circular polarization is decided by the rolling direction of the first loop of the antenna. Which means, this antenna can be also changed to a left-handed circularly polarized antenna when the copper strip is put on the paper base from the bottom right corner.

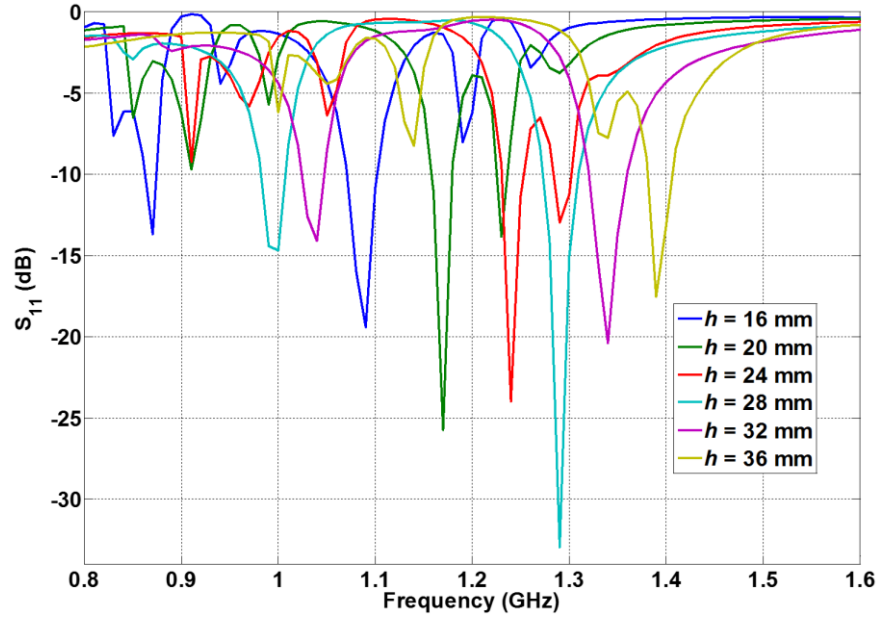
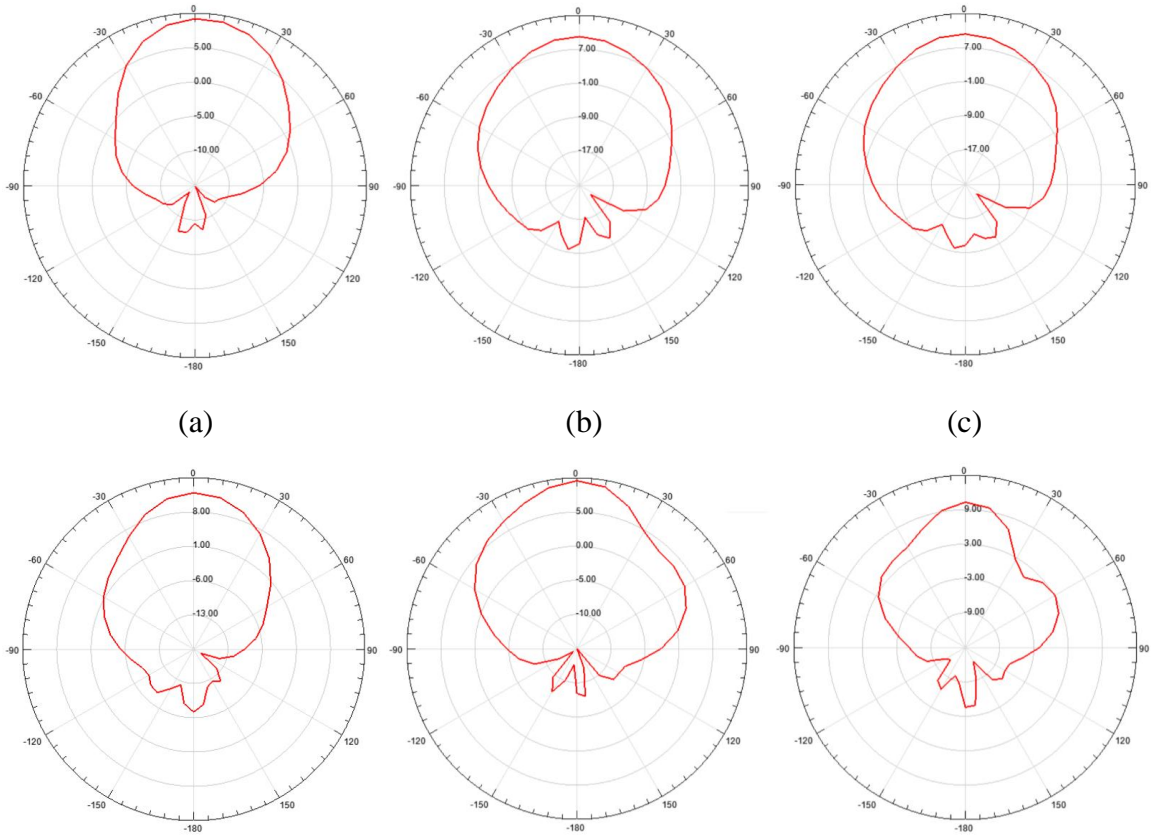


Figure 4.5. Simulated reflection coefficient of the origami spring antenna at different states.



(d) (e) (f)

Figure 4.6. Simulate realized gain pattern of the origami spring antenna at (a) 1.09 GHz with $h = 16$ mm, (b) 1.17 GHz with $h = 20$ mm, (c) 1.24 GHz with $h = 24$ mm, (d) 1.29 GHz with $h = 28$ mm (e) 1.34 GHz with $h = 32$ mm and (f) 1.39 GHz with $h = 36$ mm.

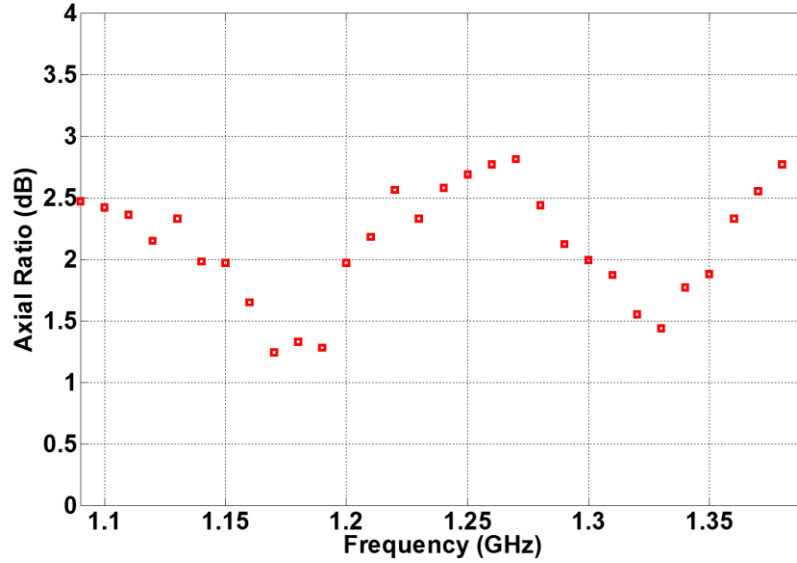
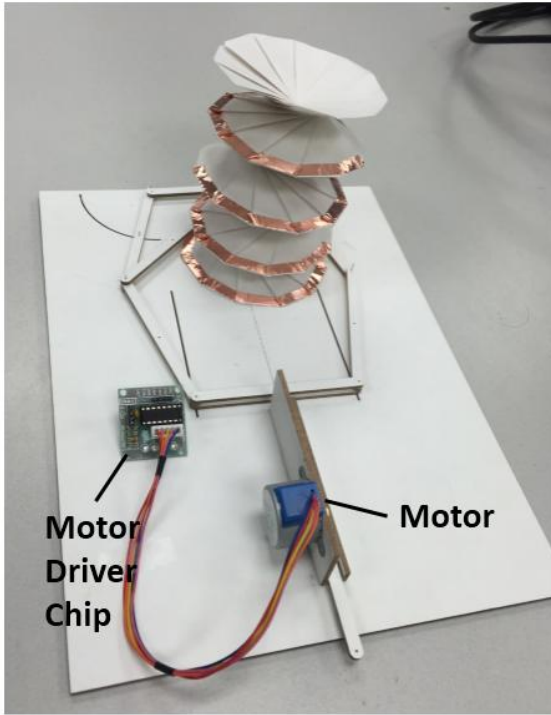
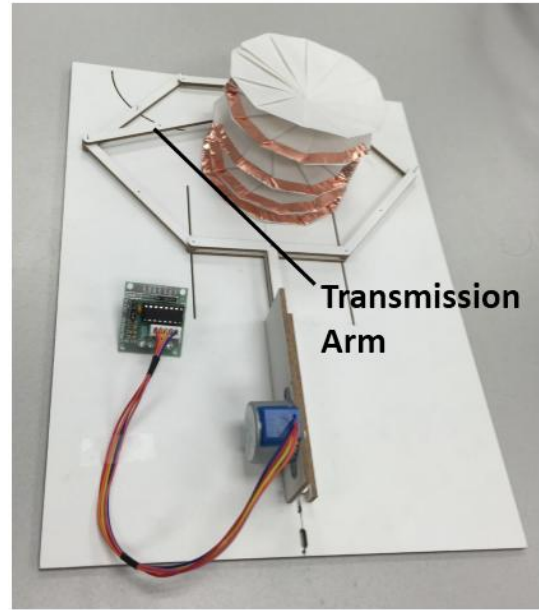


Figure 4.7. Simulated axial ratio along the $+z$ direction

Figure 4.8 shows the manufactured prototype of this origami spring antenna with the actuation system. The antenna is constructed using 0.1 mm thick copper tape on 0.15 mm thick sketching-paper substrate without any coating. The permittivity of the paper that is used to build the origami spring base is 2.2. The hexagon actuation systems is built with several plywood arms on the ground plane around the antenna, and one end of a transmission arm is glued at the corner of the first level of the antenna paper base. The position of the arms can be changed by a step motor. The 28BYJ-48 stepper motor is used, which is a 4 phase uni-polar motor (has common center connection) that works within 5-12 DC Volts. Because the whole spring body can be controlled by pressing or stretching one of its levels, the transmission arm can change the height of the whole spring body from 60 mm to 145 mm by changing the radius of the first level.



(a)



(b)

Figure 4.8. Origami spring antenna prototype with the actuation system at (a) 145 mm height, and (b) 60 mm height.

Figure 4.9 shows the measured realized gain versus frequency. The prototype was measured in the StarLab anechoic chamber. It can be seen that the peak realized gain shifts continuously from 1.1 GHz to 1.4 GHz when the antenna's total height H increases from 60 mm to 145 mm. Therefore, this is an antenna that can tune its operating frequency by adjusting its height.

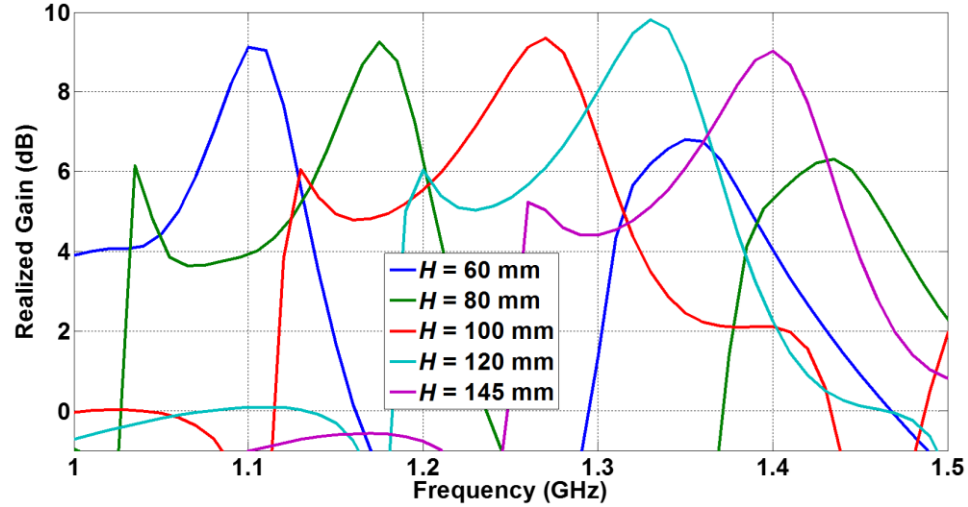


Figure 4.9. Measured efficiency of three-band CSCMR system for different distances.

4.3 A Self-deploy Yagi Loop Antenna Based on Origami Spring Structure

In this section, a Yagi loop antenna is built based on an origami spring base made out of paper. The antenna can achieve a high gain (>10 dBi) and high front-to-back ratio. The whole length of the array can be controlled by a servo gripper.

Yagi antenna arrays have been widely used in fields of long distance radio communications and point-to-point communications because of the high gain and simple structure. Compared with the classical array of dipoles, the Yagi loop is much less affected by the electrical properties of the soil. The properties of Yagi loop arrays have been studied by several investigators [89-91]. The antenna designers are able to optimize the parameters of the Yagi loop array under the constraints of the antenna size, directivity or bandwidth. However, the Yagi arrays currently on the market that operate at the lower frequencies (under 10 GHz) are too bulky. While the directors enhance the antenna's gain also increase the volume of the antenna. Folding/unfolding origami antennas can be used to minimize the size of antennas and provide reconfigurability. The structure of the origami spring is

suitable for designing Yagi loop antenna array. The big advantage of the origami spring is that the whole spring body can be controlled by applying pressure at any level.

4.3.1 Origami Yagi Loop Antenna Design

Figure 4.10 shows a Yagi array consisting of N circular loops of arbitrary dimensions. In Figure 4.10, a_i is the radius of the wire, b_i is the radius of each loop, d_{ij} is the distance between $loop_i$ and $loop_j$. To satisfy the property of a robust Yagi antenna, we will have $a_i \ll b_i$ and $a_i \ll \lambda$, where λ is the wavelength of the antenna's operating frequency [90].

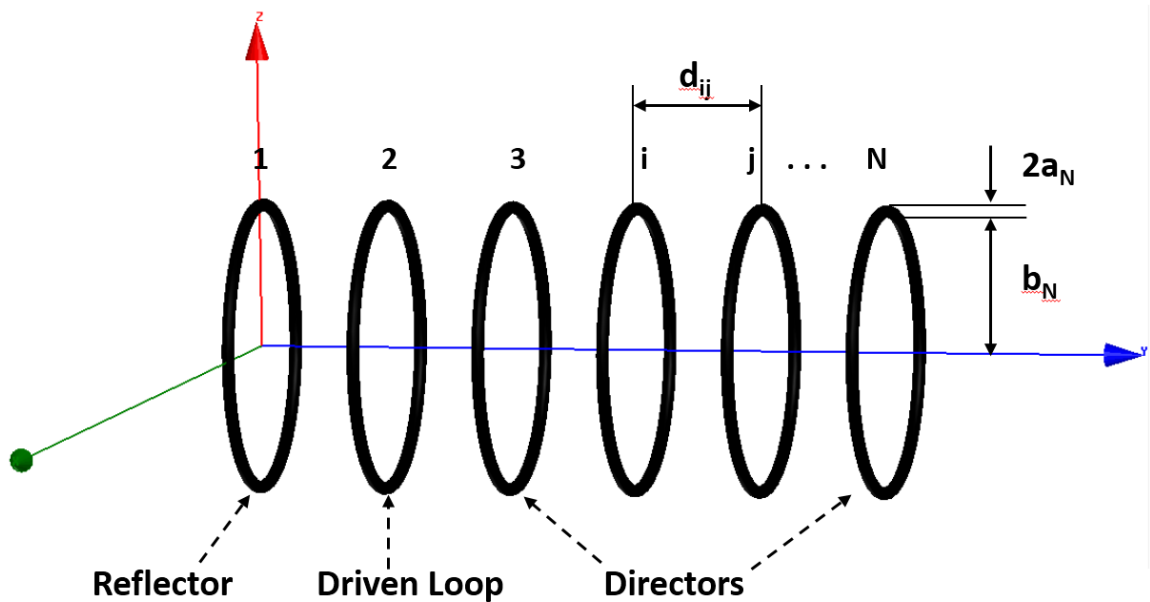


Figure 4.10. Yagi array with circular loops.

For a Yagi loop array where the second loop is the only excited one, the resulting loop currents, the input admittance Y_2 , the radiation patterns, and the forward and backward directivities G_d and G_r , are given by [91]:

$$I_i(\phi) = V_i \left[\sum_{n=m_0+1}^{n_i} 1/Z_{ii}^n + j\omega C_{gi} \right] \cos n\phi + \sum_{n=0}^{m_0} y_{i2}^n v_2 \cos n\phi. \quad (4.2)$$

$$Y_2 = I_2 / V_2. \quad (4.3)$$

$$\begin{bmatrix} E_\theta \\ E_\phi \end{bmatrix} = -\frac{\eta_0}{4r} \exp[-jkr] \begin{bmatrix} \cos \theta \\ 1 \end{bmatrix} \sum_{i=1}^N kb_i \cdot \exp(jkd_{i1} \cos \theta) \cdot \sum_{n=0}^{\infty} j^n I_i^n [J_{n-1}(x_i) \pm J_{n+1}(x_i)] \cdot \begin{bmatrix} \sin n\phi \\ \cos n\phi \end{bmatrix}. \quad (4.4)$$

$$G_{d,r} = \frac{\pi\eta_0}{4[\operatorname{Re} Y_2]|V_2|^2} \left| \sum_{i=1}^N kb_i \exp(\pm jkd_{i1}) I_i \right|^2. \quad (4.5)$$

where k and η_0 are the propagation constant and the characteristic impedance of free space, respectively. In these equations (y_{ij}^n) is the inverse of the impedance matrix (Z_{ij}^n), C_{gi} is the gap capacitance, $x_i = kb_i \cdot \sin\theta$, and the subscripts d and r in the directivity equation refer to the forward and backward gains along the array axis, respectively.

The dimensions of the rectangle unit of the 2-D spring pattern for the origami Yagi loop antenna design is same as the dimensions for the antenna design in section 4.2, i.e., $\ell = 90$ mm, and $a = 20$ mm. 5 levels spring pattern is used for this design. The first level is for the reflector loop. The excitation loop is on the second level, and the director loops are located on the third to fifth levels. The edge shape of every spring level is regular dodecagon. The distance between the dodecagon center and the edges is defined by b_i . The exciter in this design is a full wave loop antenna. The circumference of the exciter approximately equals one wavelength of the resonant frequency:

$$2\pi \cdot b_2 \approx \lambda . \quad (4.6)$$

The 5-element array used in this design is shown in Figure 4.11. The radius of the reflector is $b_1 = 0.183 \lambda$. The radii of the three directors are $b_3 = b_4 = b_5 = 0.142 \lambda$. The distance between the reflector and exciter is $d_{12} = 0.2 \lambda$. The distance between the exciter and the first director is $d_{23} = 0.18 \lambda$. The distances between directors are $d_{34} = d_{45} = d_{23}$.

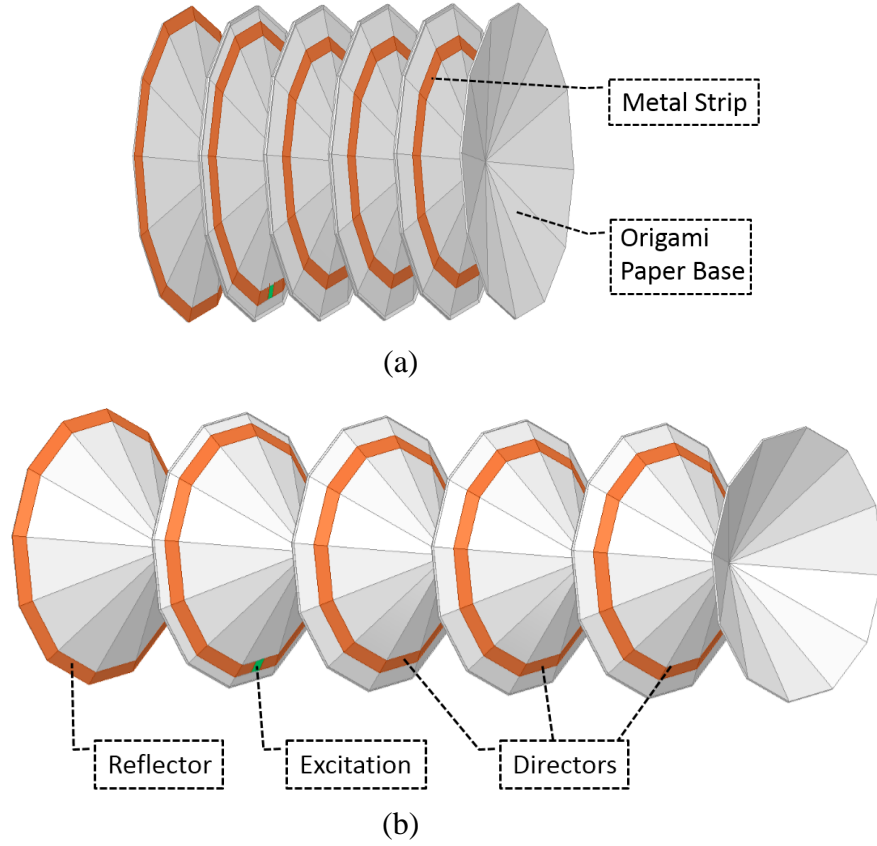


Figure 4.11. The simulation model of Yagi origami loop antenna at: (a) folded state and (b) unfolded state.

By adjusting the loop's position on the origami spring base, we can have different loop radius, and also we can modify the distance between loops on adjacent levels. We used copper tape to build the antenna. The width of the copper tape is 4 mm, and the thickness is 0.1 mm. The radius of the equivalent circular area is much less than the

wavelength. When the origami spring is unfolded, we have $b_1 = 40$ mm, $b_2 = 35$ mm, $b_3 = b_4 = b_5 = 31$ mm, as shown in Figure 4.11(b).

Usually, the impedance of the full wave single loop antenna is in the vicinity of 100 ohms. The value can be reduced when there are reflector and directors. When $d_{12} = 43$ mm, $d_{23} = d_{34} = d_{45} = 40$ mm, the input impedance plot versus frequency is shown in Figure 4.12. At 1.31 GHz, the input impedance is $64 + 0.7j$ ohms. That means 50 ohms transmission line can be used to excite the antenna.

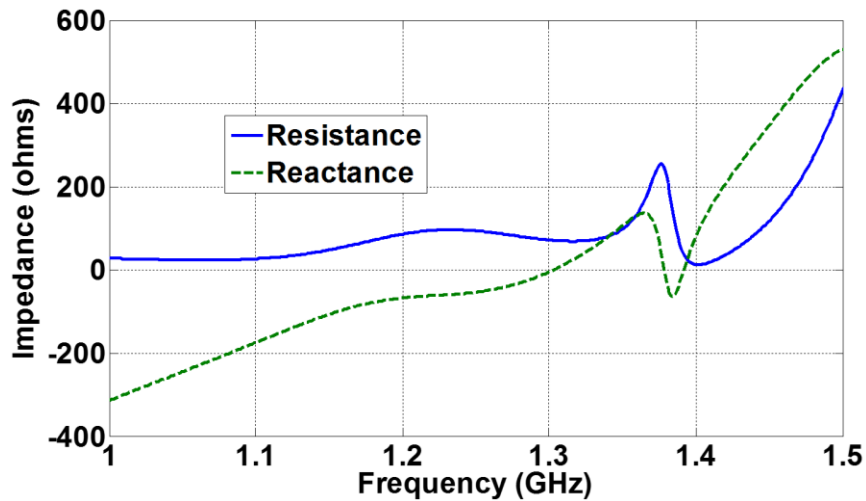


Figure 4.12. The input impedance of the origami Yagi loop array.

4.3.2 Origami Yagi loop Antenna Construction and Results

The graphs in Figure 4.13 show the manufactured prototype of the Yagi origami loop antenna. The origami spring base is built with 0.15 mm thick sketching-paper substrate without any coating, and the permittivity of the paper is 2.2. A 50 ohms coaxial line is connected to the driven loop. A ferrite choke is around the coaxial cable, working as a balun. A PLA gripper was printed by a 3D printer to control the spring body. One handle is fixed in place while the other is rotating at a given angle. When the handle rotates

inwards the gripper is pushing the antenna's sides together, making the antenna expand. The sides of the antenna are attached to the handles so that when the handle moves outwards the antenna shrinks. In order for the handle to rotate by itself, the 28BYJ-48 stepper motor is attached directly to the gripper. The spring body length is 20.5 cm when the antenna fully expands. The antenna can be compressed to 5 cm long.

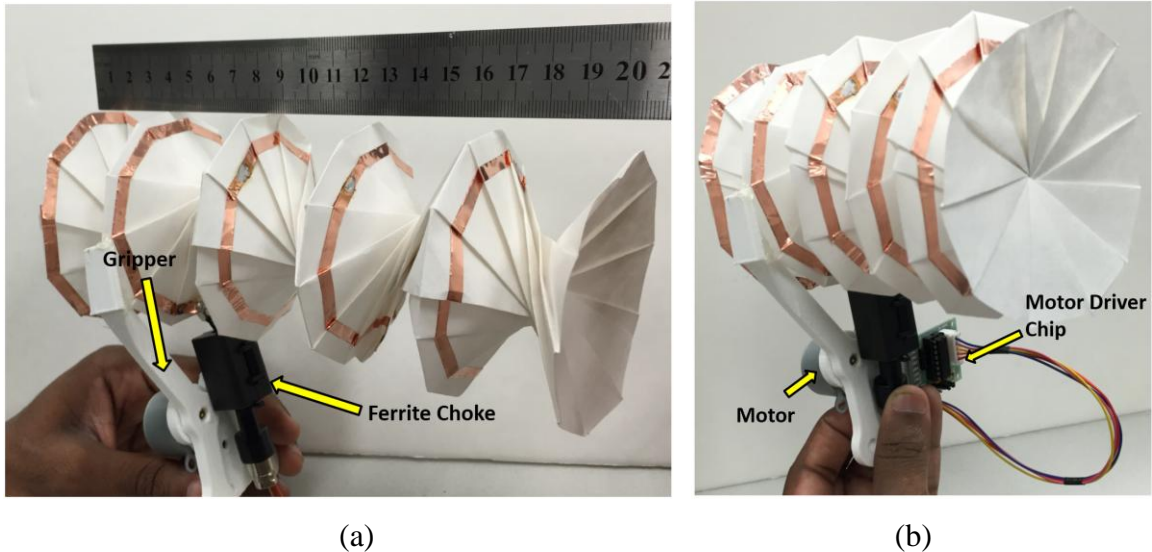


Figure 4.13. The manufactured prototype of the Yagi origami loop antenna at (a) unfolded state and (b) folded state.

The reflection coefficient versus frequency is shown in Figure 4.14. The measurements agree well with the simulation results at the operating frequency. The measured reflection coefficient is -17.4 dB at the operating frequency of 1.31 GHz.

Figure 4.15 shows the measured realized gain pattern for the elevation plane of the antenna at elevation plane and azimuth plane. The antenna works at end-fire mode. A realized gain of 10.4 dBi is achieved at 1.31 GHz. The front-to-back ratio of this antenna is greater than 14 dB. This antenna is vertically polarized.

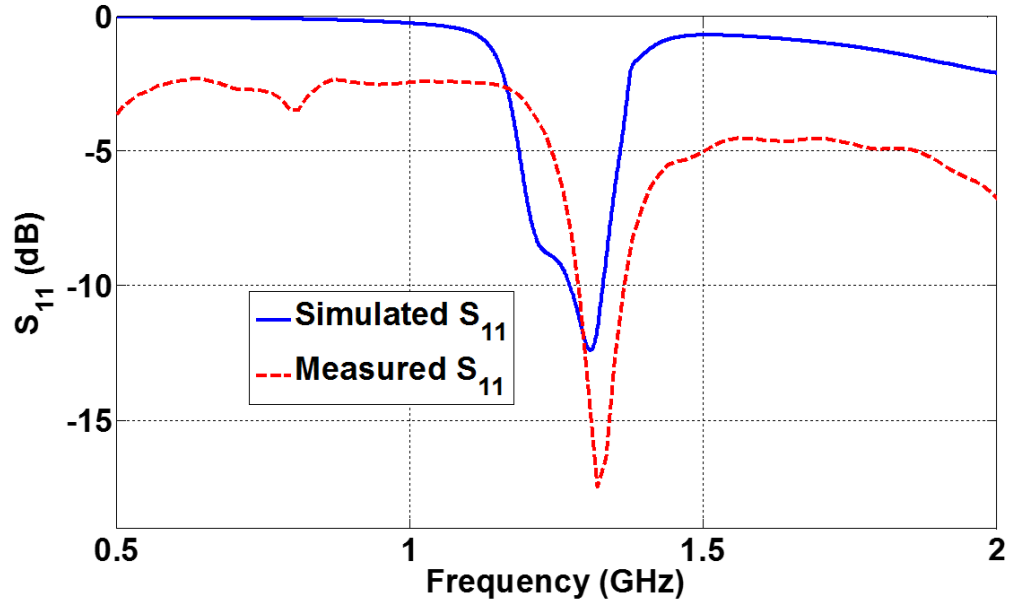


Figure 4.14. Reflection coefficient of the origami Yagi loop array.

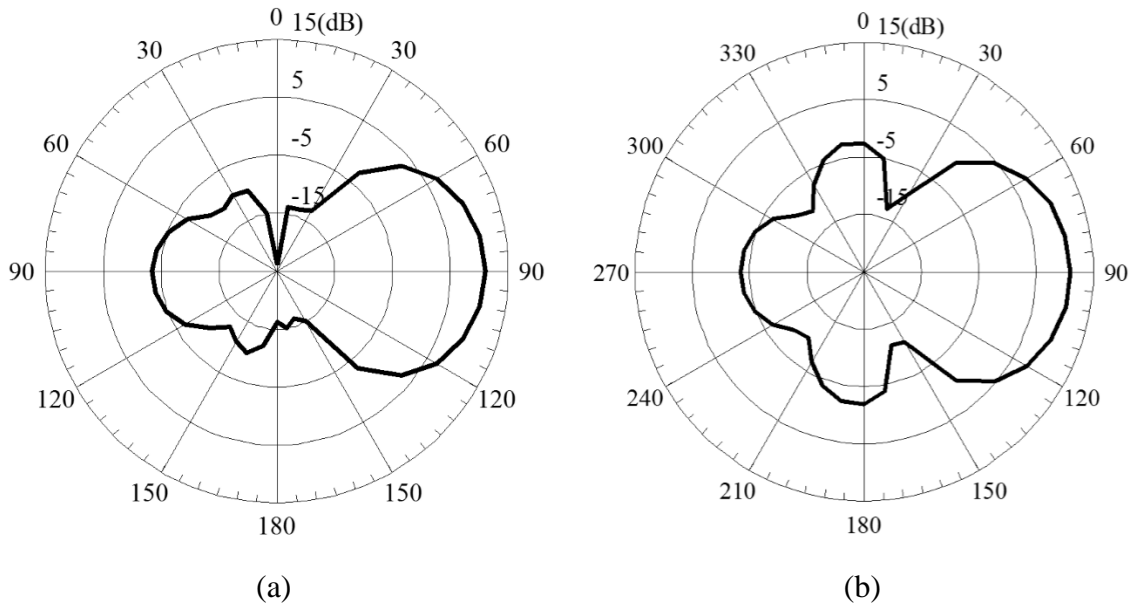


Figure 4.15. (a) Radiation pattern of elevation plane when $\varphi = 0^\circ$. (b) Radiation pattern of azimuth plane when $\theta = 90^\circ$.

The Yagi origami loop array presented in this section has high directional gain and high front-to-back ratio, and can self-fold into small volume which is suitable for applications on spaceborne structures and satellites. In this design, every level structure of

the origami spring is identical, so it's hard to design different distances between directors, that results in relatively narrow bandwidth. For future work, an origami spring structure with different level height will be investigated to make the antenna more broadband.

CHAPTER 5

MORPHING ORIGAMI CONICAL SPIRAL ANTENNA

In this chapter, a two-arm Nojima origami conical spiral antenna (CSA) is designed. The antenna is based on the origami Nojima wrap pattern that enables the antenna to morph from a planar dipole to a conical spiral antenna. The design equations of the Nojima origami CSA are presented and its performance is studied using simulations and measurements. The reflection coefficient, input impedance, gain and axial ratio of this antenna are investigated over a wide frequency band. The radiation patterns of this antenna are also examined. A prototype of an origami Nojima CSA with 1.5 turns is manufactured and measured.

The antenna parameters of CSA is briefly reviewed in Section 5.1. In Section 5.2, the relationships between the angles of the Nojima wrap pattern geometry and those of the traditional CSA are presented. Also, design formulas for Nojima origami CSAs are derived. In Section 5.3, two different quasi-equivalent Nojima origami CSAs are developed, and their performance is compared with the performance of traditional CSAs. Section 5.3 illustrates that the origami Nojima pattern can transform a planar dipole printed on a flexible substrate to a polygonal CSA thereby: (a) providing a new way to construct from planar flexible metalized substrates polygonal CSAs that exhibit similar performance to the traditional CSAs, and (b) creating a physically reconfigurable antenna that can change its performance by changing its geometry. In Section 5.4, the properties of a practical Nojima square origami CSA with a balun are examined at the folded and unfolded states. It is shown that the Nojima origami antenna exhibits reconfigurable performance at the two

states. Also, a prototype of the proposed origami antenna is constructed and its performance is validated through simulations and measurements.

5.1 Introduction of the Conical Spiral Antenna

The conical spiral antenna (CSA) is one of the most popular frequency-independent antennas and it is widely used in space and satellite communications. The CSA was developed by Rumsey [92]. Rumsey introduced the angle principle, which states that the frequency-independent antenna is entirely defined by angles. Also, the truncation principle should be satisfied for practical antennas, that the antenna must have an active region of finite size [93]. Dyson provided comprehensive information for the CSA by performing a series of measurements [94]. Yeh and Mei analyzed the CSA using the Method of Moments [95-96]. The properties of the CSA have been studied by many researchers [97-101].

A two-arm CSA that is constructed by winding two metallic strips around the surface of a truncated cone is shown in Figure 5.1. The geometry of a CSA is defined by three angles, which are the half angle of the cone, θ_0 , wrap angle, α , and the angular width, δ , of the antenna arms. The angle θ_0 is measured between the axis of the CSA and the side of the cone. When $\theta_0 = 90^\circ$, the CSA becomes a planar spiral antenna [97], which radiates equally in two directions ($\pm z$). Smaller angle values of θ_0 provide larger gain and larger front-to-back ratio. The angle α , which describes the rate of wrap of the arms, is the angle between the antenna arm and the radial line from the apex of the cone. The greater angle α causes more uniformity in the main lobe [100]. In most applications, θ_0 is from 5° to 15° , and α is from 60° to 80° [99]. The angle δ defines the angular width of the arms along the cone, and it is constant everywhere along the cone. Larger δ always yields a higher

attenuation rate and slightly narrower beam-width [96]. When $\delta = 90^\circ$, the metallic arms are identical in size and shape to the non-metalized regions of the conical surface. This is called a self-complementary structure, which is most commonly used in CSAs. The minimum and maximum diameters of the truncated cone are d and D , respectively. The bandwidth (BW) of the CSA is limited by the minimum and maximum diameter of the cone and is approximately written as [99]:

$$BW = \frac{f_{\max}}{f_{\min}} = \frac{\lambda_{\max}}{\lambda_{\min}} \approx \frac{D}{d}. \quad (5.1)$$

The sense of rotation of the circularly polarized field is determined by the direction of winding of the CSA arms.

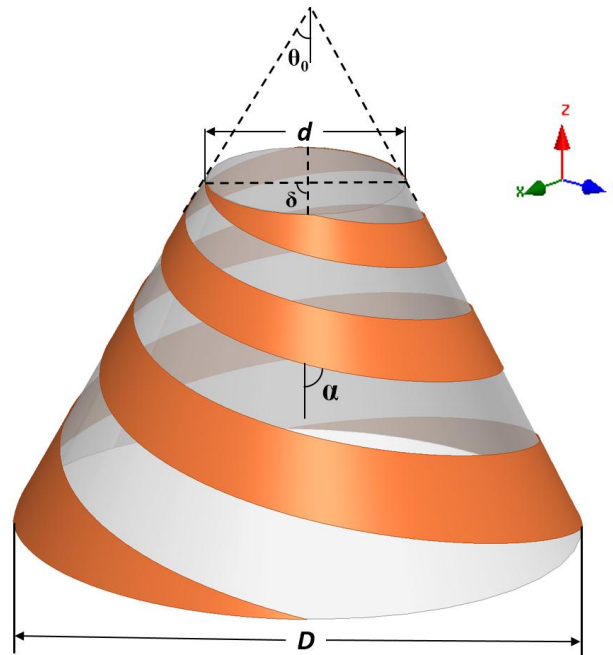


Figure 5.1. Geometry of a two-arm conical spiral antenna.

5.2 Design of Nojima Origami CSA

The Nojima wrapping origami structure was proposed by Taketoshi Nojima [5]. This structure can fold a 2-D pattern into a symmetrical 3-D wrap shape without any cutting or gluing. Various types of Nojima wrap models can be designed by using different central-hub shapes and different angles between segments. A narrowband reconfigurable origami antenna was developed in [102] by attaching a metal strip of uniform width on a Nojima origami base. In this section, a new origami antenna based on the Nojima wrap, which can morph itself from a 2-D planar dipole to a 3-D CSA, is developed. The design equations of this Nojima origami CSA are derived for the first time and presented here. The Nojima origami CSA meets the two necessary conditions for frequency-independent antennas: the angle principle and the truncation principle [92-93], i.e., the investigated antenna has broadband performance characteristics, such as uniform input impedance, circular polarization and realized gain.

The Nojima wrap pattern is a symmetrical structure. The central-hub of a Nojima wrap pattern has to be an N -gon shape [5]. Figure 5.2(a) shows a Nojima wrap pattern sheet with a square central-hub. The square side length is ℓ . The inner angle φ ($\angle ABC$) of the central-hub is

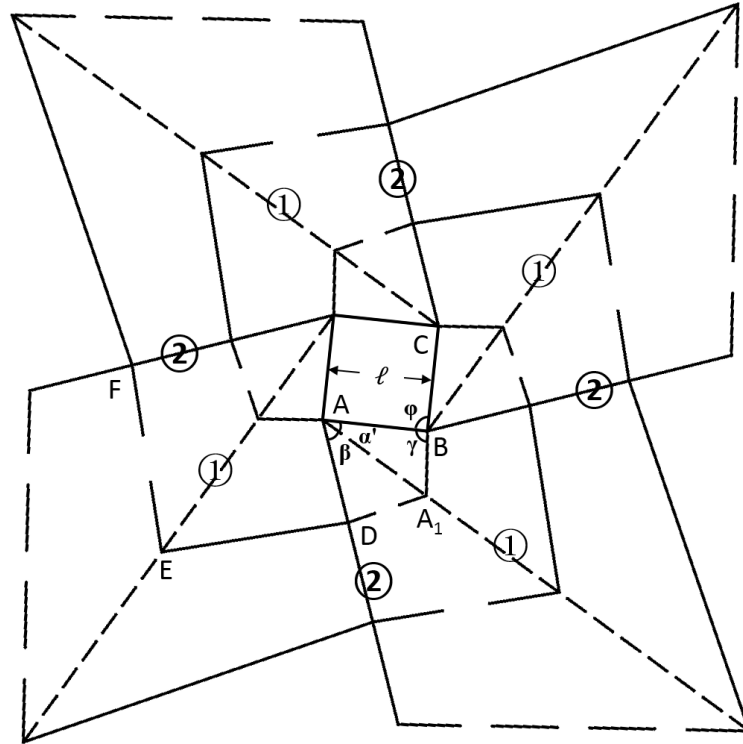
$$\varphi = (N - 2) \times \pi / N . \quad (5.2)$$

In order to construct the fold lines of the Nojima pattern, pairs of dashed lines and solid lines need to be drawn from the corners of the central-hub, as shown by ① and ② in Figure 5.2(a). In this chapter, all solid fold lines correspond to mountain-folds and all dashed fold lines correspond to valley-folds. These fold lines will make the pattern sheet fold like an

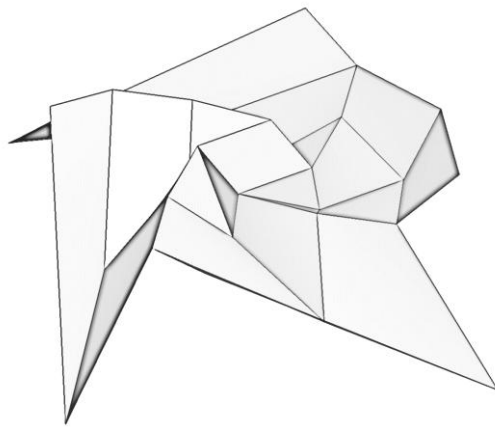
umbrella. Then, in order to make the pattern sheet roll around the central-hub, the following steps are followed: (a) another solid line from corner B needs to be drawn and intersect line ① at the point A_I (note that angle $\angle A_I B A$ is arbitrary), (b) draw a dashed line from point A_I until it intersects line ② at point D , (c) make $\angle A A_I D$ equal to $\angle A A_I B$, i.e., line $A_I B$ and line $A_I D$ are symmetrical to line ①, (d) draw line segments DE , EF in similar way, i.e., lines DA_I and line DE are symmetrical to line ②, as lines ED and line EF are symmetrical to line ①. These steps provide an Archimedean type spiral fold line $BA_I DEF$. When this fold line $BA_I DEF$ intersects lines ① and ②, the line pattern must be interchanged from solid to dashed. Similarly, fold lines like $BA_I DEF$ must be drawn from every corner of the central-hub.

Finally, by folding the sheet along the creases marked by the fold lines, the sheet can be wrapped into the semi-folded shape shown in Figure 5.2(b) and the fully folded shape shown in Figure 5.2(c). The fully folded pattern occurs when every surface of the pattern touches adjacent surfaces without any space between them. For our discussion, angles $\angle BAA_I$, $\angle A_I AD$, and $\angle ABA_I$ are denoted as α' , β , and γ , respectively. The four angles α' , β , γ and φ define the geometry of the origami Nojima wrap. The following condition must be satisfied in order to wrap the sheet around a central hub symmetrically to its vertical axis, [5]:

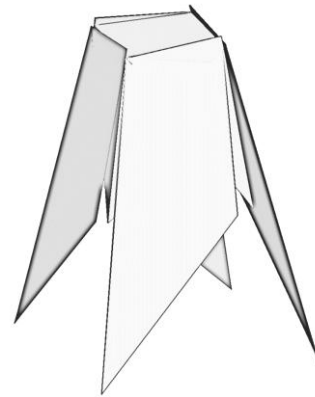
$$\beta + \gamma = (\pi / 2)(1 + 2 / N). \quad (5.3)$$



(a)



(b)



(c)

Figure 5.2. (a) Geometry of flat Nojima pattern sheet with a square central-hub. (b) Semi folded Nojima pattern sheet. (c) Fully folded Nojima pattern sheet.

Different wrapping models can be designed by choosing different angles β and γ . It should be noted that the fold lines are calculated without taking into account the thickness of the sheet. In practice, the creases need to be adjusted based on the thickness of the

substrate so that the wrapped layers are logarithmically separated from each another radially in the fully folded state, rather than being coplanar [103].

The geometry of the fully folded square central-hub Nojima wrap pattern is a truncated square pyramid shape as shown in Figure 5.3(a). Every side of the model has the isosceles trapezoid shape. The upper corner angles of the trapezoid are equal to γ . If we place a metal strip along line ① (valley-fold line), when the sheet is fully folded, the metal strip will have a conical square spiral shape, as shown by the black strip in Figure 5.3(a). The angle between the metal strip and the trapezoid top line is equal to α' . The winding direction of the metal strip is right-handed. A left-handed line can be achieved when α' is larger than $\pi/2$. The relationship between α' and the CSA angle α is

$$\alpha' = \pi / 2 - \alpha . \quad (5.4)$$

Figure 5.3(b) shows the cross section through the symmetry axis of the pyramid. If the material thickness can be omitted, the half vertex angle θ' is defined only by the inner angle φ and the angle γ as

$$\theta' = \sin^{-1} \left[\tan \frac{\varphi}{2} \times \tan \left(\gamma - \frac{\pi}{2} \right) \right]. \quad (5.5)$$

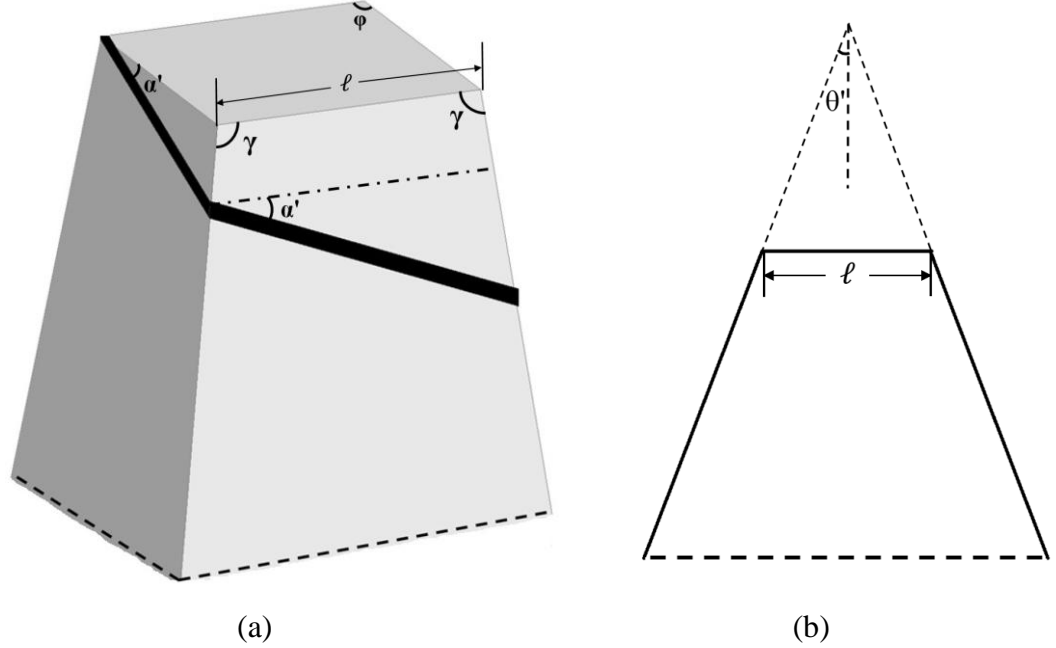


Figure 5.3. (a) Metal strip on the fully folded square central-hub Nojima wrap pattern.
 (b) Cross-section through the symmetry axis of the pyramid.

When $\gamma = \pi/2$, the pattern will fold into a cuboid, and the metal strip will have a helical shape. When $\gamma > \pi/2$, the bigger γ is, the bigger θ' is. When $\gamma < \pi/2$, the whole pattern will fold upward, and the central-hub will be the bottom of the structure. The folded pattern will have the same structure if all the creases in Figure 5.2(a) are folded in the reverse fashion, i.e., the valley folds will be mountain folds and vice versa, and $\angle ABA_1$ is made equal to $\pi - \gamma$. In the rest of this paper, only the $\gamma > \pi/2$ case is considered. When the thicknesses of the substrate and metal layer are taken into account, the half vertex angle θ' can be derived as

$$\theta' = \sin^{-1} \left[\tan \frac{\varphi}{2} \times \tan \left(\gamma - \frac{\pi}{2} \right) \right] + \sin^{-1} \left[\frac{(2t_1 + t_2) \sin(\alpha' + \gamma)}{\ell \sin \gamma \sin \alpha'} \right]. \quad (5.6)$$

where t_1 is the thickness of the substrate and t_2 is the thickness of the metal layer. In practice, the actual θ' may have slight disagreement with the theoretical value because of the slight deformation of the material surface.

The length of each segment of the metal strip that forms the antenna can be calculated. In Figure 5.4, $\angle AA_1B$ is denoted as $\angle 1$, $\angle AA_2B_1$ is denoted as $\angle 2$, etc. Also, $\angle ADA_1$ is denoted as $\angle 1'$, $\angle AD_1A_2$ is denoted as $\angle 2'$, etc. The following relations are true:

$$\angle 1 = \pi - \alpha' - \gamma. \quad (5.7)$$

$$\angle 1' = \alpha' + \gamma - \beta. \quad (5.8)$$

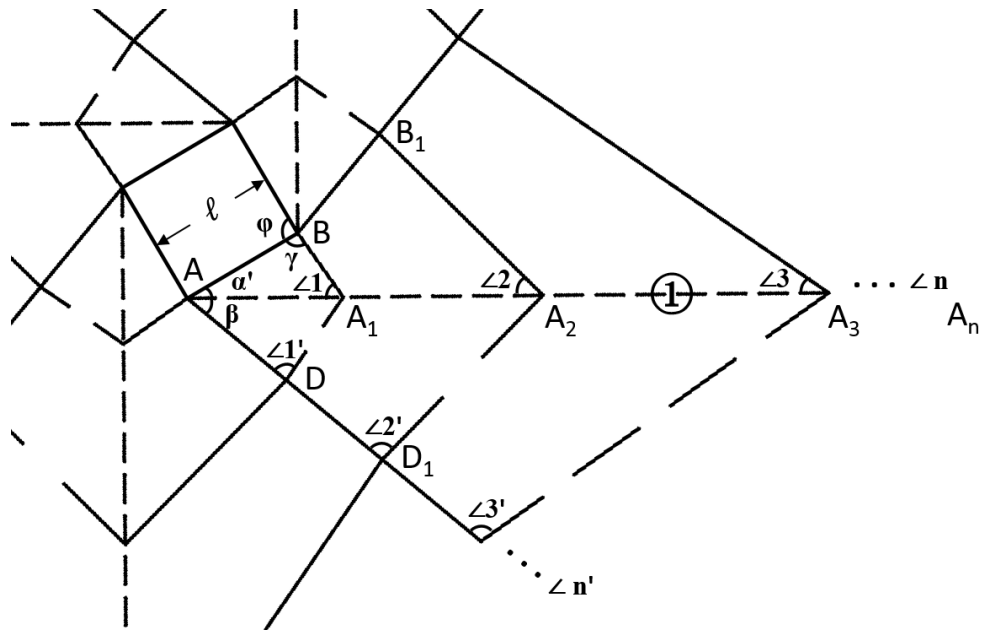


Figure 5.4. The angles along the metal strip line (valley fold line).

By using trigonometrical functions, the relationship between $\angle n$ and $\angle(n-1)$ is as follows:

$$\angle n = \angle(n-1) - (\pi - \varphi - 2\beta). \quad (5.9)$$

This means that as the number of turns of the spiral fold line increases, the angle $\angle n$ decreases. Also, in order to make the entire Nojima pattern have a closed shape, $\angle n$ should be positive. Therefore, the maximum number of the segments, n_{max} , of line ① satisfies the following condition:

$$n_{max} < \frac{\pi - \alpha' - \gamma}{\pi - \varphi - 2\beta} + 1. \quad (5.10)$$

From the formulas (5.3) and (5.10), it is found that when angle γ increases, the maximum number of metal strip segments decreases. Noticing that $\angle n$, $\angle n'$, and β are the three interior angles of a triangle, the relationship between $\angle n'$ and $\angle(n-1)'$ is found from the equation (5.9), that is

$$\angle n' = \angle(n-1)' + (\pi - \varphi - 2\beta). \quad (5.11)$$

By using the law of sines, the length of segment AA_l is determined from triangle ABA_l as

$$\ell_{AA_l} = \sin \gamma \times \ell / \sin(\alpha' + \gamma). \quad (5.12)$$

The length of AA_n in terms of AA_{n-1} is the following:

$$\ell_{AA_n} = \frac{\ell_{AA_{n-1}} \times \sin \angle(n-1) + \ell \times \sin(\alpha' + \angle n)}{\sin \angle n}. \quad (5.13)$$

As previously mentioned in this chapter, when $\delta = 90^\circ$, the traditional CSA achieves best radiation performance. The same radiation performance can be achieved by the origami CSA design. Here, the square central-hub Nojima pattern is used as an example. In this case, the metal strip needs to be widened to make the truncated square pyramid shape a self-complementary structure. In Figure 5.5, each quadrilateral $A_n A_{n+1} B_n B_{n-1}$ will be a side face of the truncated square pyramid when the pattern is fully folded. A parallel

line to line ② from point A_1 intersects line A_2B_1 at point M_1 . The horizontal cross section passing through point A_1 of the folded structure will be a square, and segment A_1M_1 will be an edge of this square. Points $M_2, M_3 \dots M_n$ can be similarly found. It can be proven that all M points are on a straight line. Also, all the angles $\angle A_n A_{n-1} M_{n-1}$ are equal to the angle between line ① and line ②, which is

$$\angle A_n A_{n-1} M_{n-1} = \pi - \beta - \varphi. \quad (5.14)$$

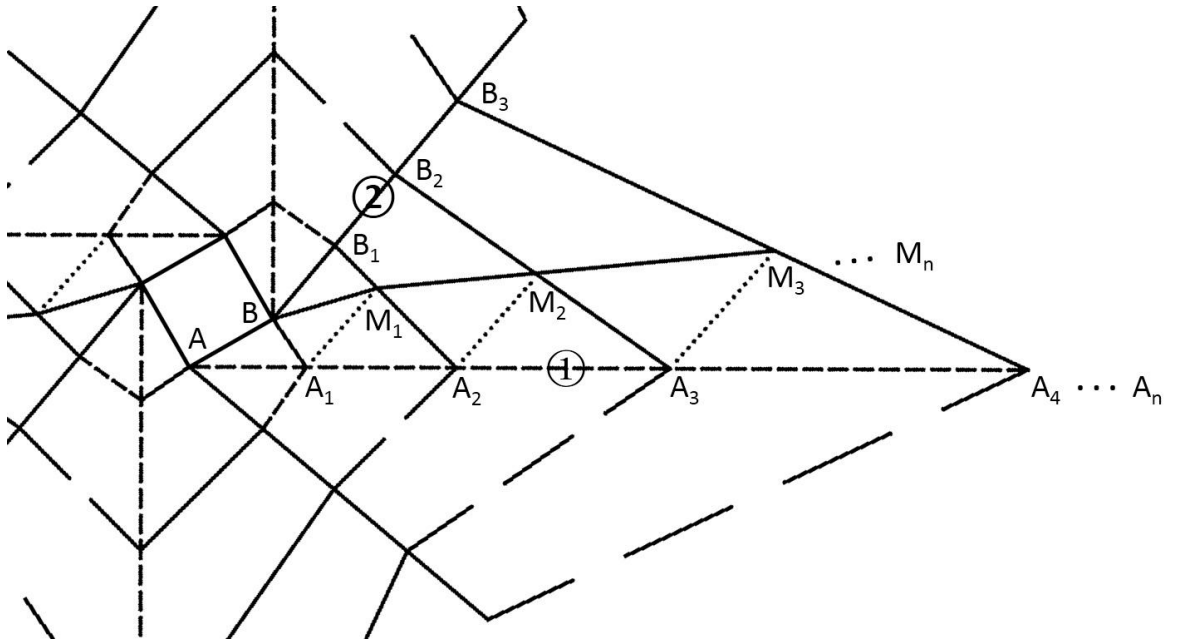


Figure 5.5. The metal layer area for best antenna performance.

By putting the metal layer in the area $AA_n M_n M_1 B$, the metal layer covers half of the perimeter of the horizontal cross section when the pattern is fully folded. The length of segment line $A_n M_n$ can be calculated from the following equation:

$$l_{A_n M_n} = \frac{(l_{AA_n} - l_{AA_{n-1}}) \sin \angle n}{\sin(\angle n + \beta + \varphi)}. \quad (5.15)$$

The active region of this antenna moves from the central-hub to the large end of

metal layer as the wavelength of the radiation goes from $\lambda_{min} \approx N \cdot \ell$ to $\lambda_{max} \approx N \cdot \ell_{AnMn}$ [94].

From the formula (5.1), the BW is approximately:

$$BW = \frac{f_{max}}{f_{min}} = \frac{\lambda_{max}}{\lambda_{min}} \approx \frac{\ell_{AnMn}}{\ell}. \quad (5.16)$$

5.3 Comparison between the Nojima Origami CSA and the Traditional CSA

In this section, two types of a two-arm Nojima origami CSA (square central-hub and hexagon central-hub) are designed and compared to the traditional CSA. All the results are simulated using ANSYS HFSS.

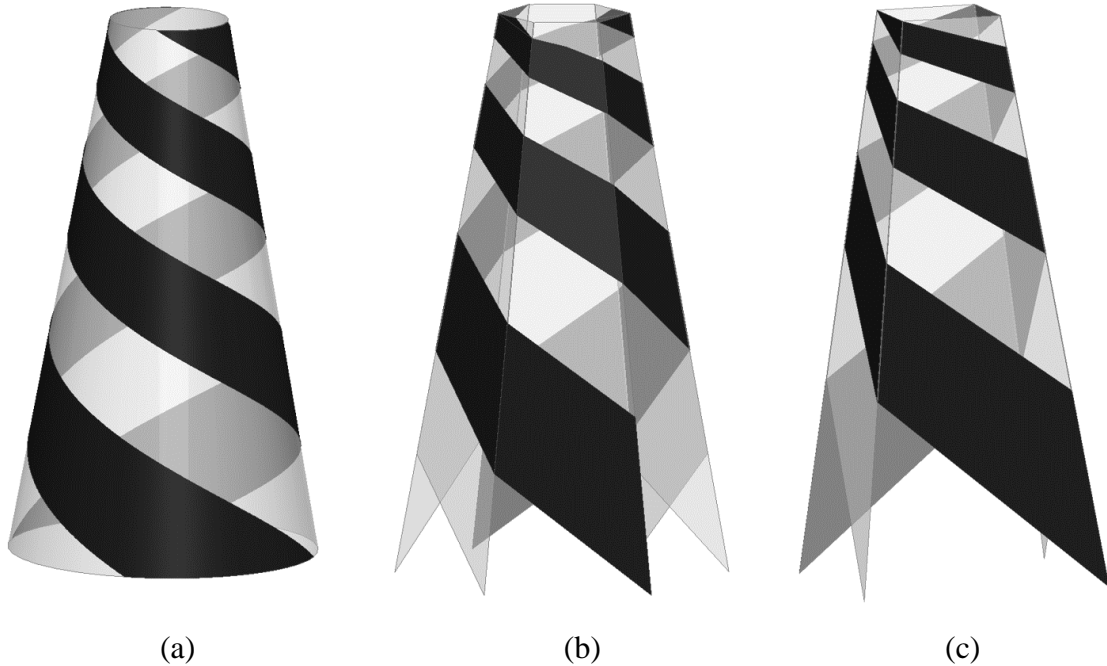


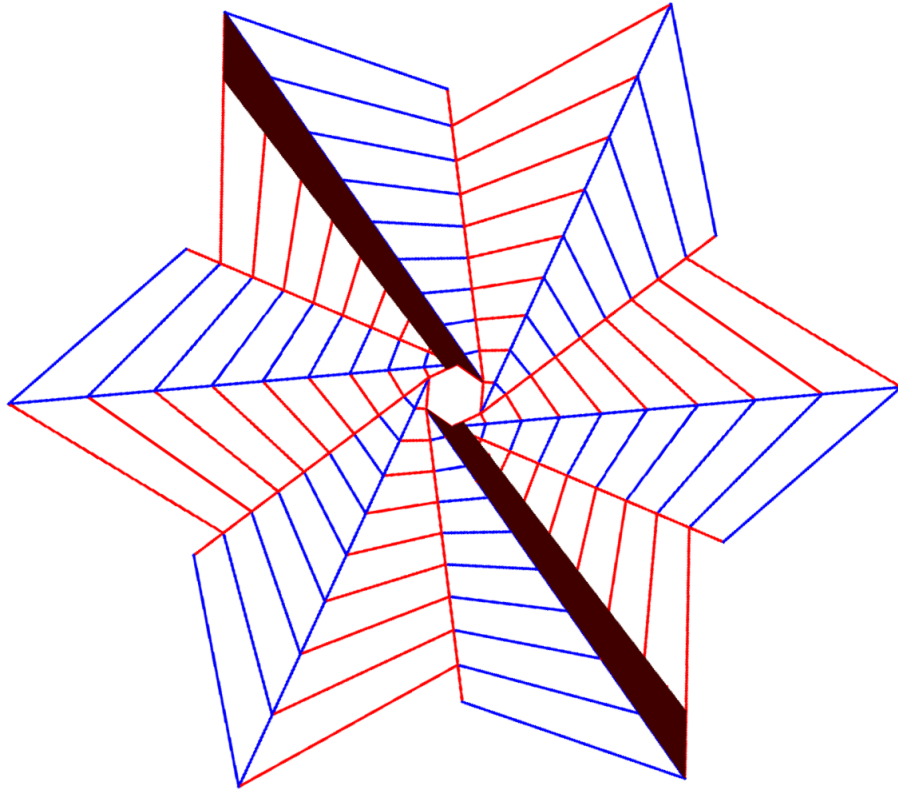
Figure 5.6. (a) The traditional CSA. (b) Hexagon central-hub Nojima origami CSA. (c) Square central-hub Nojima origami CSA.

Figure 5.6(a) shows the model of a traditional two-arm CSA. Each arm of the CSA has 1.5 turns. The half angle of the cone θ_0 is 7.6° , the wrap angle α is 70° , and the angular width δ is 90° . The minimum diameter, d , is 23 mm, and the maximum diameter, D , is 48 mm. The total height h of the traditional CSA is 93.7 mm. The active region of this CSA

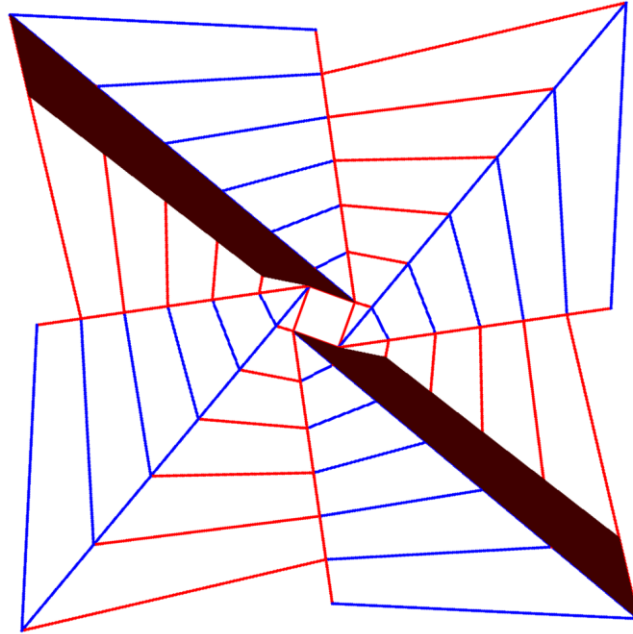
moves from the small end to the large end as the operating frequency changes from $f_{min} \approx 2$ GHz to $f_{max} \approx 4.2$ GHz. The winding directions of the antenna arms are right-handed.

Two Nojima origami CSA models (one with a square central-hub, and one with a hexagon central-hub), which are quasi-equivalent to the CSA of Figure 5.6(a), are shown in Figure 5.6(b) and Figure 5.6(c). Each quasi-equivalent model is designed based on similar geometric dimensions (i.e., top diameter d , bottom diameter D , half angle of the cone θ_0 , and total height h) to the ones of the traditional CSA, and identical number of turns (i.e., 1.5 turns) of the traditional CSA model. This means that the volume of the Nojima origami CSAs is approximately the same to the CSA of Figure 5.6(a).

Figure 5.7 shows the metallization layout (represented by the brown area) on the planar (unfolded) Nojima pattern. The red lines in the figure correspond to mountain-folds and all the blue lines correspond to valley-folds. In order to make the Nojima origami CSA have 1.5 turns, lines ① and ② of the Nojima hexagon pattern must have 9 segments, and lines ① and ② of the Nojima square pattern must have 6 segments. Two metal strips are placed symmetrically on the flat dielectric substrate, as shown in Figure 5.7. It is expected that this structure will work as a dipole when the substrate is flat (i.e., unfolded). The performance of the unfolded antenna is discussed in Section 5.4. In the simulation model, the thickness of the metal layer is 0.1 mm. From the equations in Section 5.2, the values of all the parameters of the Nojima Origami CSA are calculated and listed in Table 5.1.



(a)



(b)

Figure 5.7. (a) Metal layer on the planar hexagon central-hub Nojima pattern. (b) Metal layer on the planar square central-hub Nojima pattern.

Table 5.1. Parameters of the Nojima Origami CSAs.

Parameters	Hexagon central-hub Nojima Origami CSA	Square central-hub Nojima Origami CSA
N	6	4
φ	120°	90°
α'	20°	20°
γ	92°	93°
β	28°	42°
ℓ	12 mm	19 mm
n	9	6

Figure 5.8 shows the simulated input impedance (resistance and reactance) of the three antennas. These results illustrate that the reactance of the Nojima hexagon and square CSAs is close to zero from 2.3 GHz to 3.5 GHz and 2.5 GHz to 4 GHz, respectively. Also, the resistance of the Nojima hexagon CSA is approximately 150Ω in the operating frequency range of the traditional CSA (2 GHz - 4.2 GHz), whereas the resistance of the Nojima square CSA is approximately 100Ω from 2.3 GHz to 4 GHz. Our simulation analysis has shown that when the angle parameters of the origami CSAs are set, the number of turns of each arm will not significantly affect the input impedance. In fact, the input impedance is mostly dependent on the shape of the central-hub of the CSA. Also, since the central-hub of the Nojima hexagon CSA geometry has more sides than that of the Nojima square CSA, the Nojima hexagon CSA is geometrically more similar to the traditional CSA and therefore, it is expected that the input impedance performance of the Nojima hexagon

CSA will be more similar to the one of the traditional CSA.

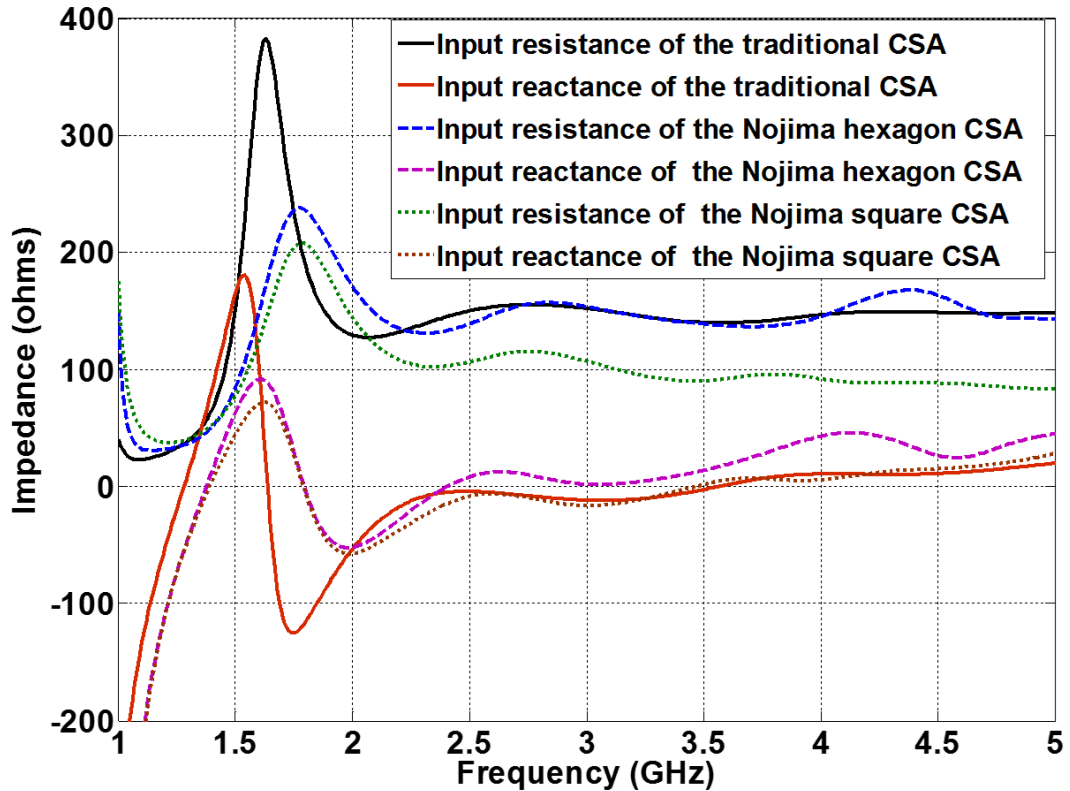


Figure 5.8. Simulated input impedance of three CSA antennas.

Figure 5.9 shows the simulated gain along the zenith direction (+z) versus frequency of the three CSA antennas. It can be seen that in the operational frequency band the gain of both Nojima origami CSAs is approximately 1 dB lower than the gain of the traditional CSA. Gain depends on an antenna's radiation intensity and total power accepted by the antenna and it does not include the reflection efficiency. Also, it should be noted that the conduction and dielectric efficiency of all three antennas is approximately 100%. Therefore, the lower gain of the Nojima CSAs is due to the lower directivity of the Nojima CSA radiation patterns.

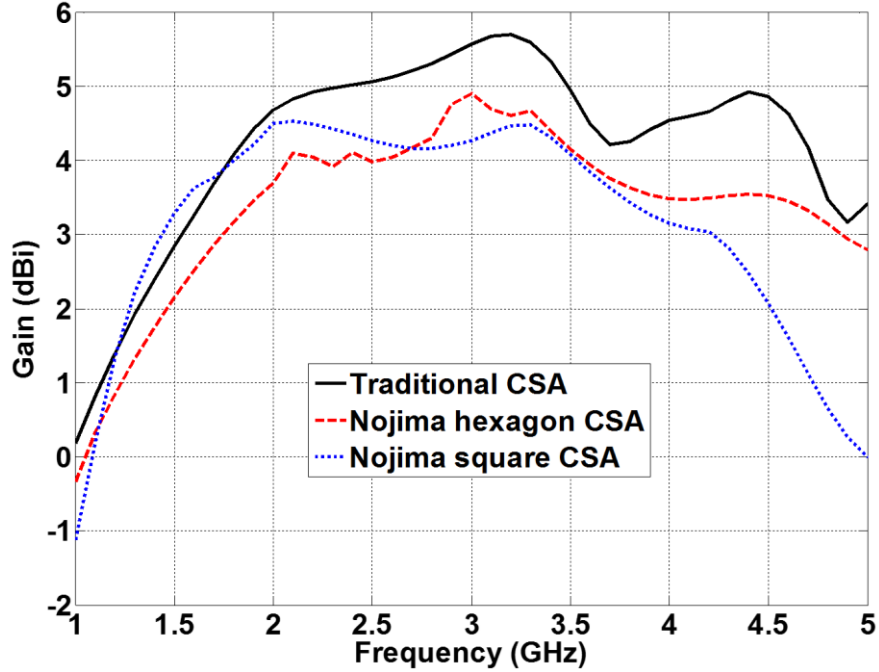
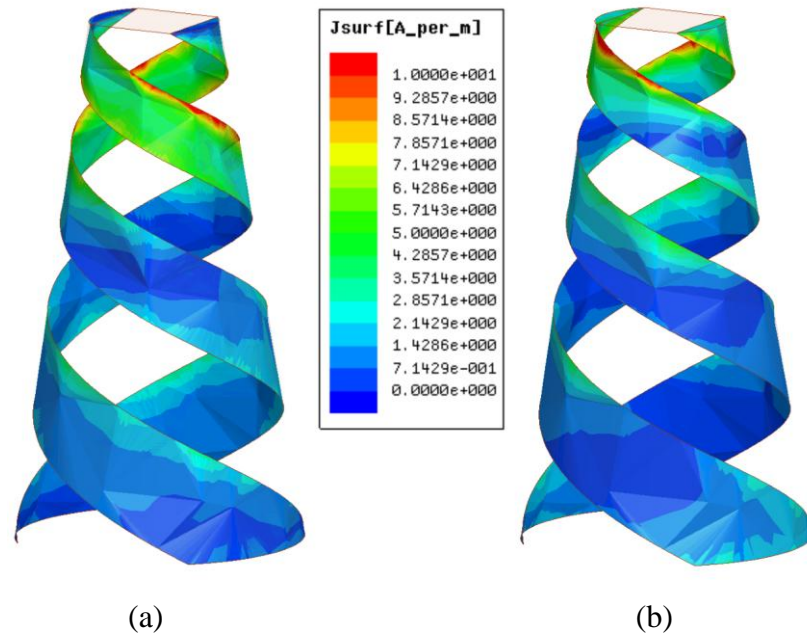


Figure 5.9. Simulated gain along the $+z$ direction of three CSA antennas.

The field at the highest operating frequency of the CSA is radiated from the small end of the cone whereas the field at the lowest operating frequency is radiated from the large end of the cone. In fact, the part of the cone, where its cross section is approximately one wavelength in circumference at a given frequency, is responsible for the majority of the radiated field at this frequency [99]. As previously mentioned in this paper, the volume of the Nojima hexagon CSA and that of the Nojima square CSA are approximately the same. Therefore, the perimeters of both the small and large ends of the Nojima square CSA are larger than the corresponding perimeters of the Nojima hexagon CSA. Thus, at the lower frequency range (below 2.7 GHz), the Nojima square CSA has better radiation performance. This also explains why the gain of Nojima hexagon CSA is better at the higher frequency range (above 2.7 GHz).

Figure 5.10 shows the surface current density distribution of the traditional CSA and the Nojima origami CSAs at 2.5 GHz and 3.5 GHz. It can be observed that the Nojima origami CSAs have a similar current distribution compared to the traditional CSA. The magnitude of the current density initially increases to its peak value as it flows away from the input port and then decreases in value [96]. The distance from the input port at which the current is maximum is directly proportional to the wavelength of the operating frequency. It can be seen that the current magnitude maximum position moves closer to the input port of the antenna as the frequency increases.



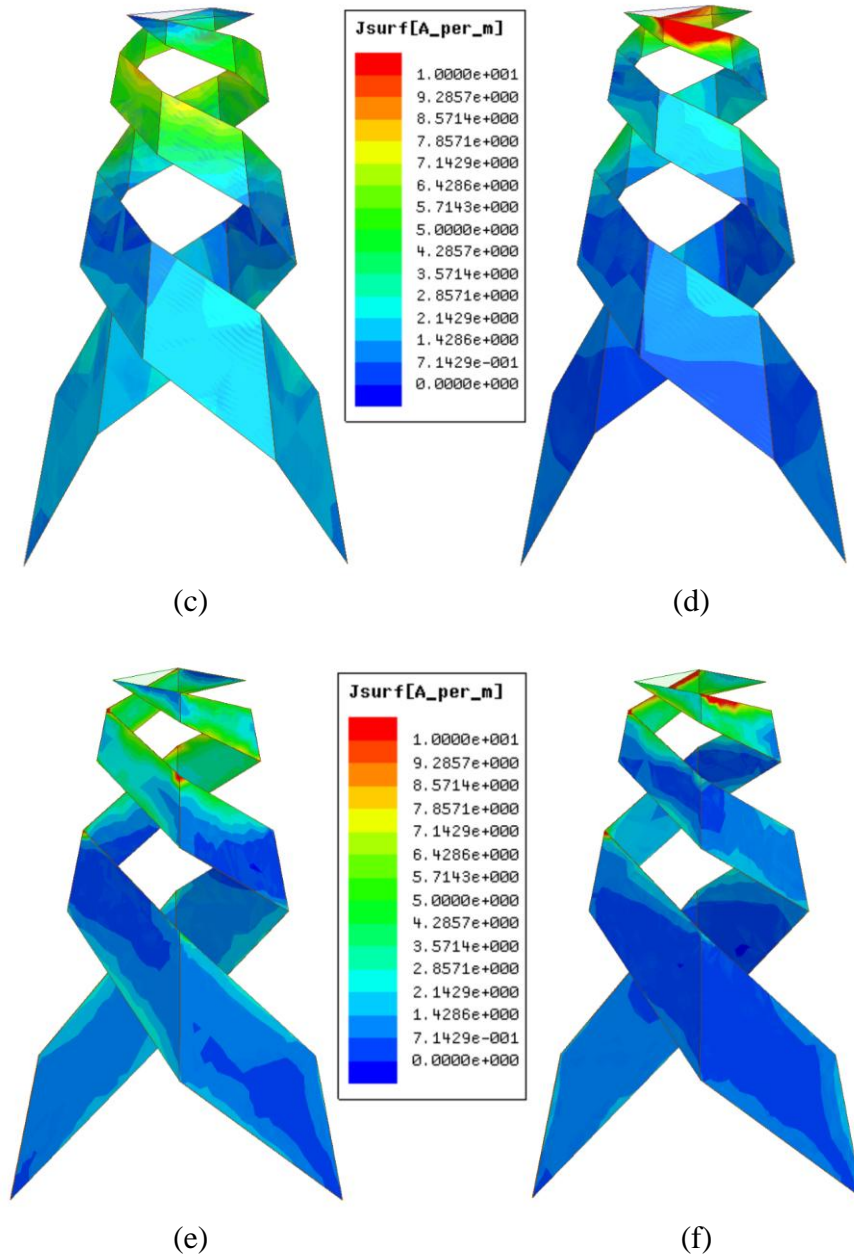


Figure 5.10. The surface current density distribution of (a) the traditional CSA at 2.5 GHz, (b) the traditional CSA at 3.5 GHz, (c) the Nojima hexagon CSA at 2.5 GHz, (d) the Nojima hexagon CSA at 3.5 GHz, (e) the Nojima square CSA at 2.5 GHz, (f) the Nojima square CSA at 3.5 GHz.

The simulated axial ratio of the three CSAs at zenith is shown in Figure 5.11. The axial ratio of all three CSAs is below 2 (i.e., 3 dB) in the traditional CSA's operating frequency band. Therefore, all three CSAs are circularly polarized.

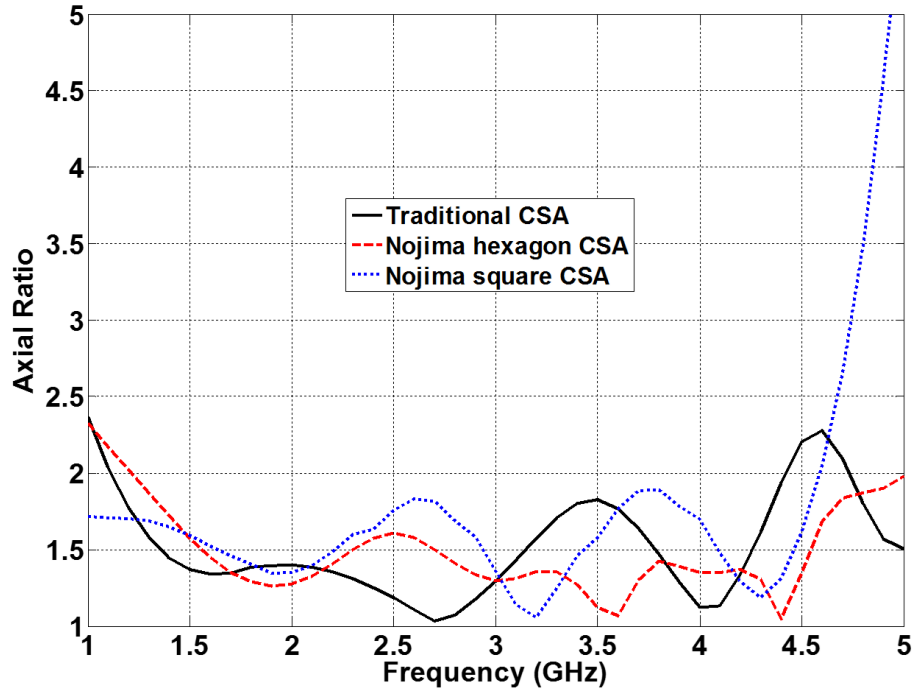
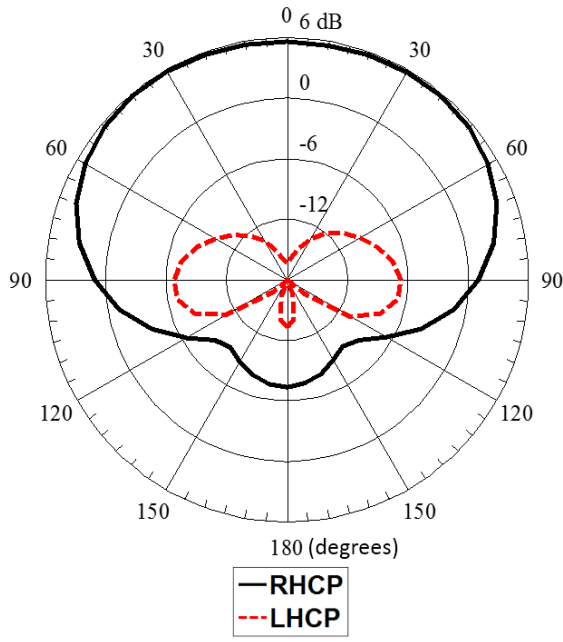


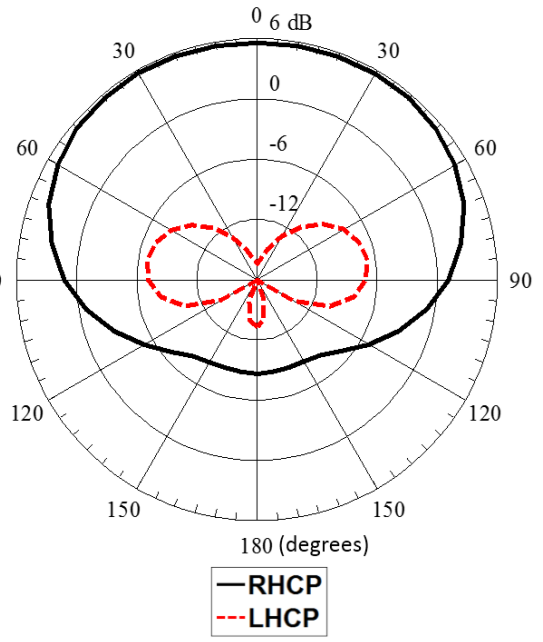
Figure 5.11. Simulated axial ratio along the +z direction of three CSA antennas.

Figure 5.12 shows the elevation patterns for $\varphi = 0^\circ$ and $\varphi = 90^\circ$ for the three CSAs. The patterns are given for both of the circular polarized components of the electric field, i.e., right-handed and left-handed. It is seen, that all three CSAs are right-handed circularly polarized as expected and the radiation pattern is directional towards zenith.

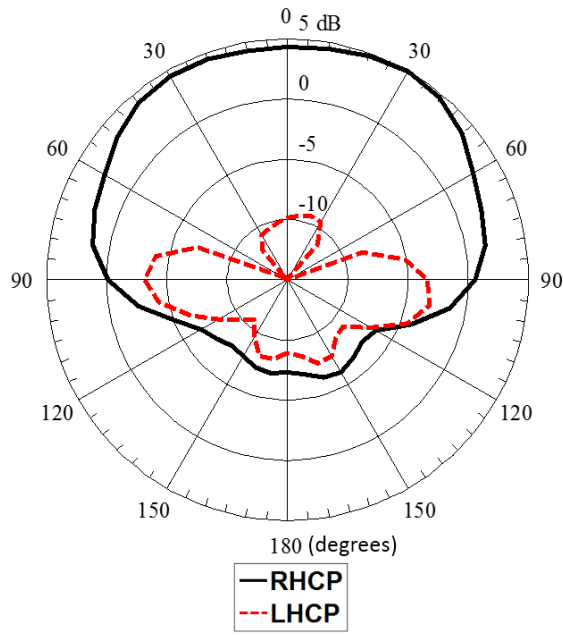
Figure 5.8, Figure 5.9 and Figure 5.11 show that all the 3 CSAs have broadband performance [100]. The operating frequency bandwidths of the quasi-equivalent origami CSAs are smaller compared with the bandwidth of the traditional CSA. When we increase the number of sides of the central-hub, N , of the origami CSA model, the antenna input impedance will be closer to the traditional CSA, and the antenna gain will increase at the higher frequency range but decrease at the lower frequency range.



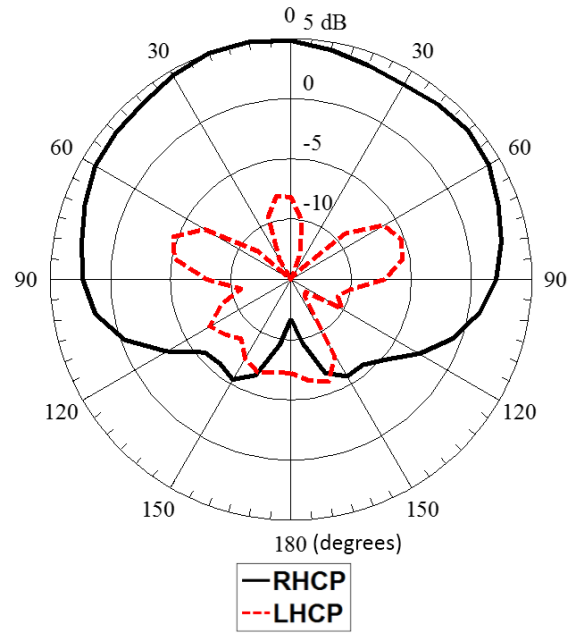
(a)



(b)



(c)



(d)

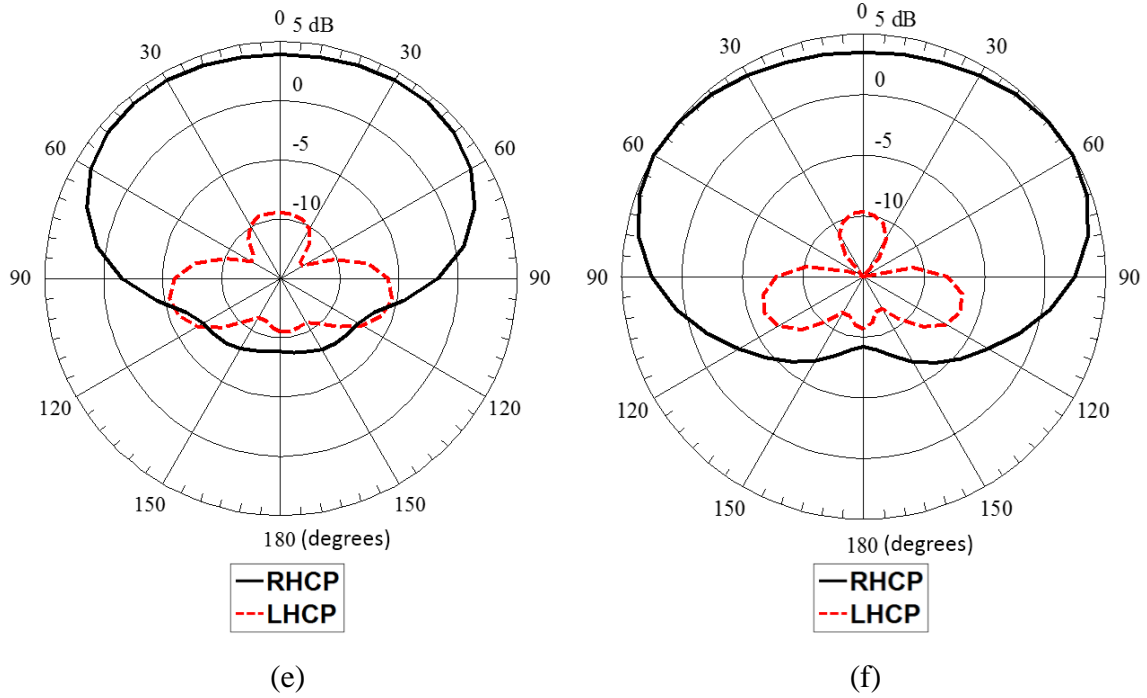


Figure 5.12. Elevation patterns for the right-handed and left-handed circular polarized components of the electric field at the frequency $f = 3$ GHz: (a) traditional CSA for $\phi = 0^\circ$, (b) traditional CSA for $\phi = 90^\circ$, (c) Nojima hexagon CSA for $\phi = 0^\circ$, (d) Nojima hexagon CSA for $\phi = 90^\circ$, and (e) Nojima square CSA for $\phi = 0^\circ$, (f) Nojima square CSA for $\phi = 90^\circ$.

The bandwidth of the origami CSA can be increased by increasing its number of turns and decreasing its wrap angle. For example, if we decrease α' to 15° , a new Nojima square pattern can be built in the same area, in which the lines ① and ② will have 8 segments, as shown in Figure 5.13(a). The pattern will be folded into a 2-turn Nojima square CSA with the wrap angle α equals 75° , as shown in Figure 5.13(b). From the simulation results, the operating frequency band of this 2-turn Nojima square CSA is 2 GHz - 3.8 GHz. The gain along the +z direction of the 2-turn CSA is approximately 0.5 dB lower than the 1.5 turns CSA, and its E-plane beamwidth is 10° - 20° wider than the 1.5-turn CSA in the operating frequency band.

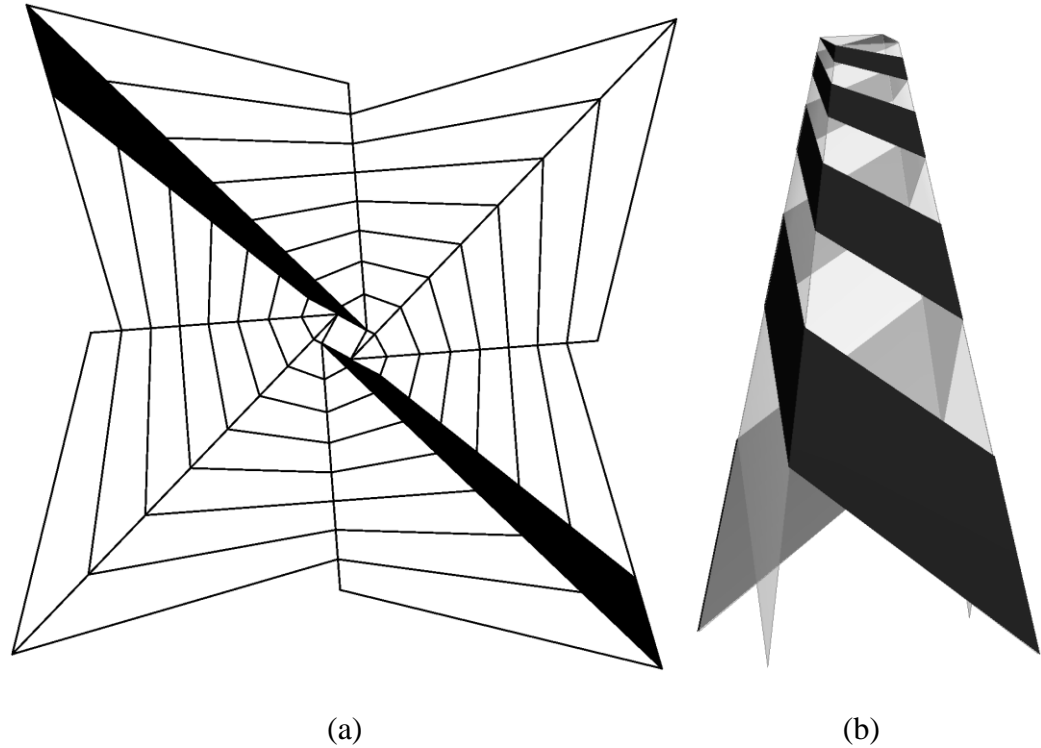


Figure 5.13. (a) Square central-hub Nojima pattern with $\alpha' = 15^\circ$. (b) 2 turns Nojima origami square CSA.

5.4 Manufacture and Measurements of Nojima Square CSA Prototype

The prototype of the square central-hub Nojima origami CSA shown in Figure 5.6(c) is manufactured here. The prototype is constructed using 0.1 mm thick copper tape on 0.2 mm thick sketching-paper substrate without any coating. The copper tape is glued on the paper and creased with the paper, so that it will stay attached to the paper substrate when the antenna is being folded and unfolded. The paper substrate was modeled in the simulations with a relative dielectric constant ϵ_r of 3.2 [104]. The unfolded antenna is shown in Figure 14(a). Figure 14(b) shows the folded Nojima square CSA. The blue paper tape is used to make the sketching-paper substrate tight, as close as possible to the fully folded state. The substrate thickness of this prototype is very small compare to the central-

hub size, and the CSA only has 1.5 turns, so the fully folded prototype shape is approximately the same to the simulation shape shown in Figure 6(c).

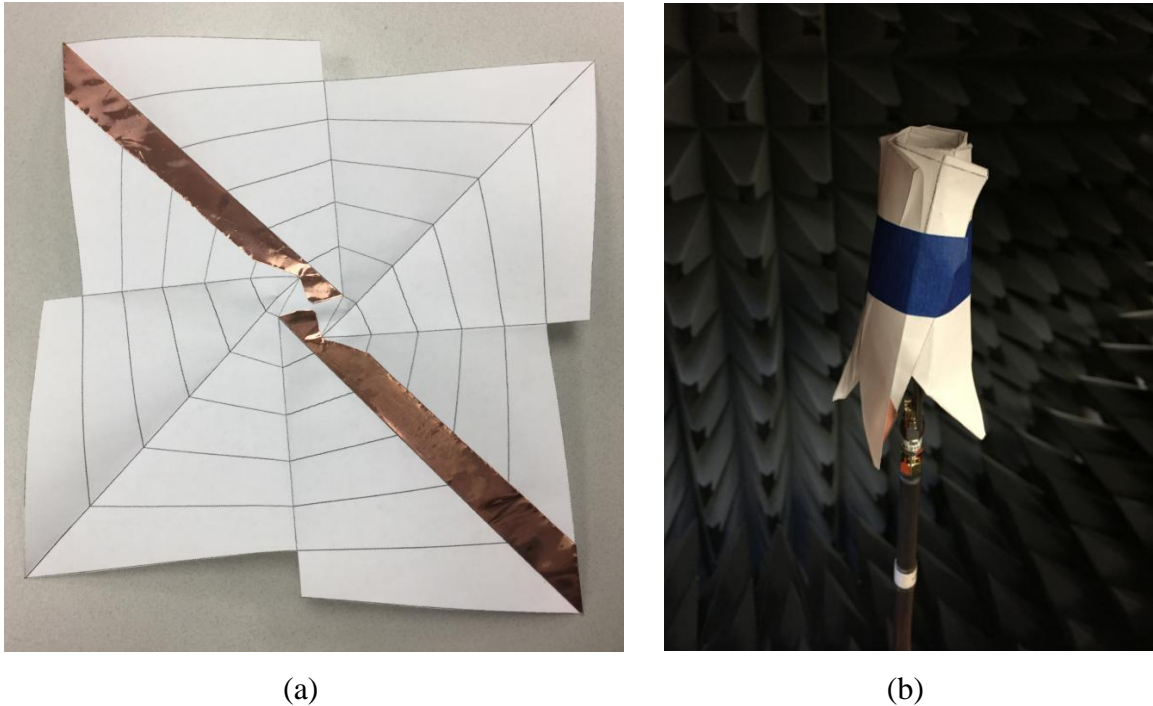


Figure 5.14. The prototype of the Nojima square CSA at (a) unfolded state and (b) fully folded state.

Both the unfolded state (dipole antenna shape) and the folded state (Nojima square CSA) are balanced radiating structures, while the coaxial cable is an unbalanced feed structure. Thus, a balun structure must be used to transform the unbalanced feeding signal to the balanced antenna and realize the impedance transformation [105-106]. Figure 5.15 shows the front and back side of the linearly tapered microstrip balun. Rogers RO5880 with the dielectric constant $\epsilon_r = 2.2$ is the substrate material of the balun. The substrate thickness h is 1.5 mm. The length of the balun l_1 is 90 mm. From the simulation results in Figure 5.8, the widths w_1 , w_2 , and w_3 were found to be 2.4 mm, 4.5 mm, and 25 mm, respectively, as shown in Figure 5.15. At the input port, the cross-section of the line resembles a microstrip with approximately 50Ω characteristic impedance, while, at the

output port, the strips are of equal width, constituting a balanced strip double line with approximately 100Ω characteristic impedance. This balun also exhibits wideband performance. A 50Ω SMA connector is soldered at the input side of the balun. Two slots were cut on the central-hub of the paper substrate, allowing the copper tape to pass through. The copper tape was soldered at the output of the balun.

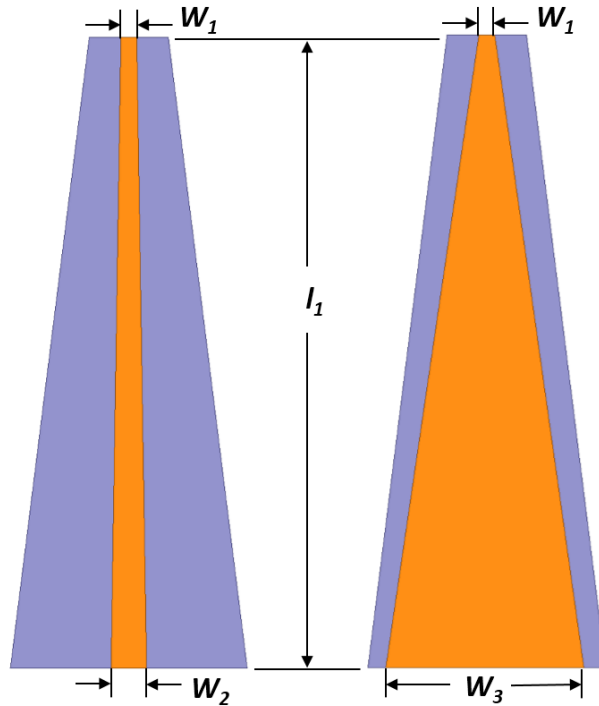


Figure 5.15. The front and back side of the linearly tapered microstrip balun.

Figure 5.16 shows the simulation antenna models with the balun of the unfolded and fully folded states. In order to make the antenna shape clear, the paper layers are hidden in the picture. The side length of the central-hub for the Nojima CSA prototype is 19 mm. From Section III, lines ① and ② of the Nojima square pattern have 6 segments. The width, which is denoted as ℓ_{A6M6} (see ℓ_{AnMn} in Figure 5.5), of the metal strip ends is approximately 32 mm. From the formula (5.16), the bandwidth of the folded antenna is approximately

1.78. The measured bandwidth is 1.67 with the antenna's operating frequency ranging from 2.1 GHz to 3.5 GHz [99]. The measured bandwidth is slightly smaller than the theoretical one.

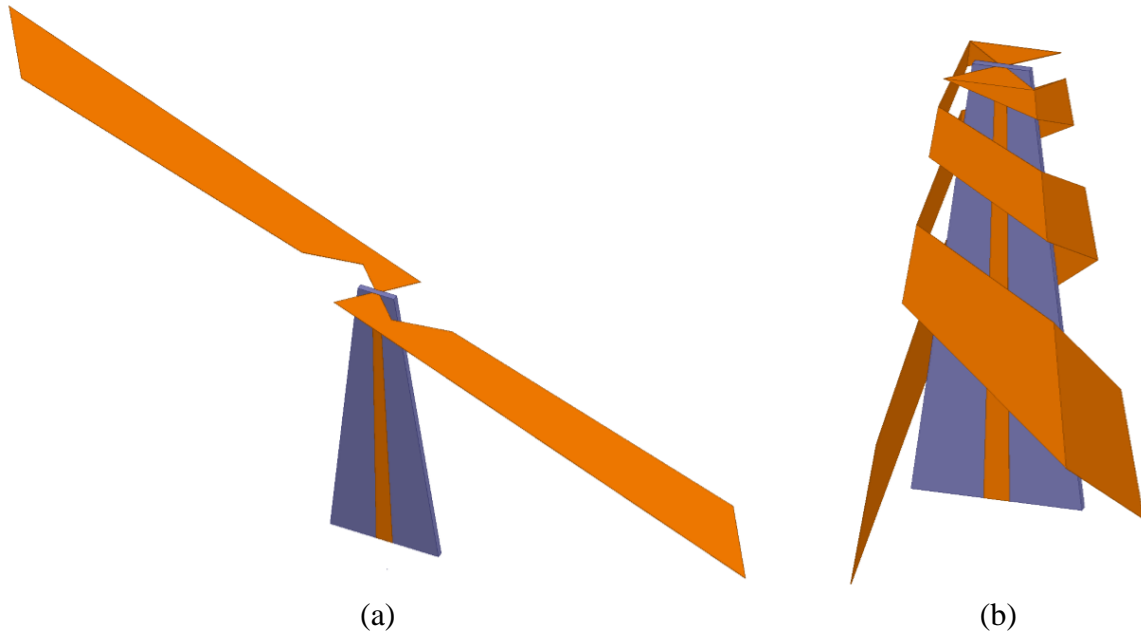


Figure 5.16. The simulation Nojima square CSA model with balun at (a) unfolded state and (b) fully folded state.

It should be pointed out that the proposed origami antenna is a physically reconfigurable antenna (i.e., an antenna that can change its performance by changing its physical geometry) that can operate as: (a) a CSA when it is folded and (b) a dipole when it is unfolded. When this antenna operates as a dipole antenna, it will operate at a significantly lower frequency than the lowest operating frequency of the CSA, because the dimension of the unfolded dipole is much larger than the folded CSA.

In Figure 5.16(a), the total length of each metal arm, which is denoted as ℓ_{AM6} is 148 mm, so the dipole is expected to operate as a half-wavelength dipole around 0.5 GHz. Figure 5.17 shows the simulated and measured reflection coefficient of the Nojima square

CSA at the unfolded state, where it operates as a dipole. Figure 5.18 shows the simulated and measured reflection coefficient of the Nojima square CSA at the fully folded state. The reflection coefficient of this antenna is below -10 dB from 2.1 GHz to 3.5 GHz for both simulation and measurement, which confirms its broadband operation.

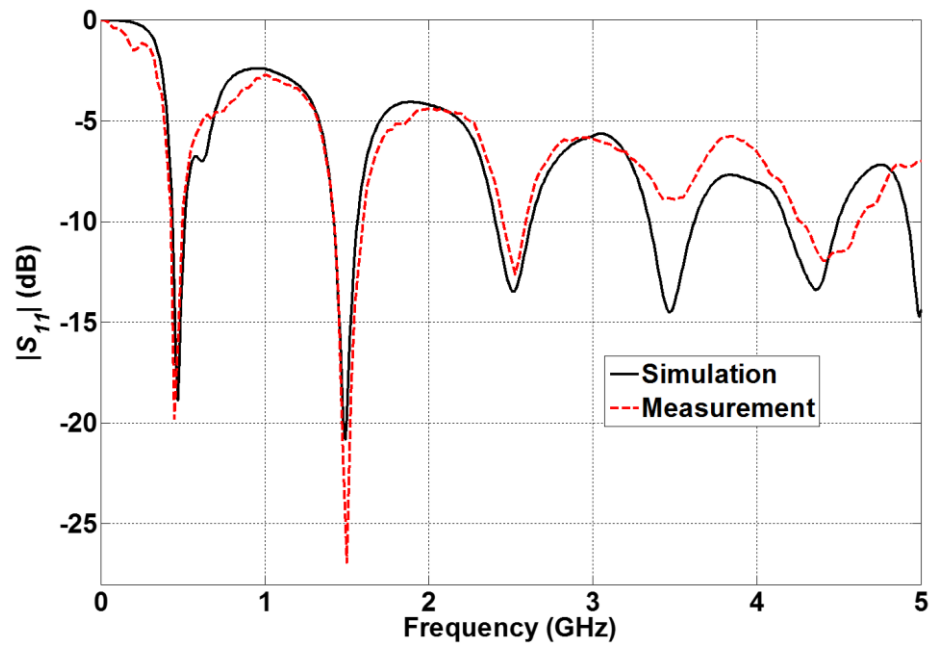


Figure 5.17. The simulated and measured S_{11} of the Nojima square CSA at the unfolded state.

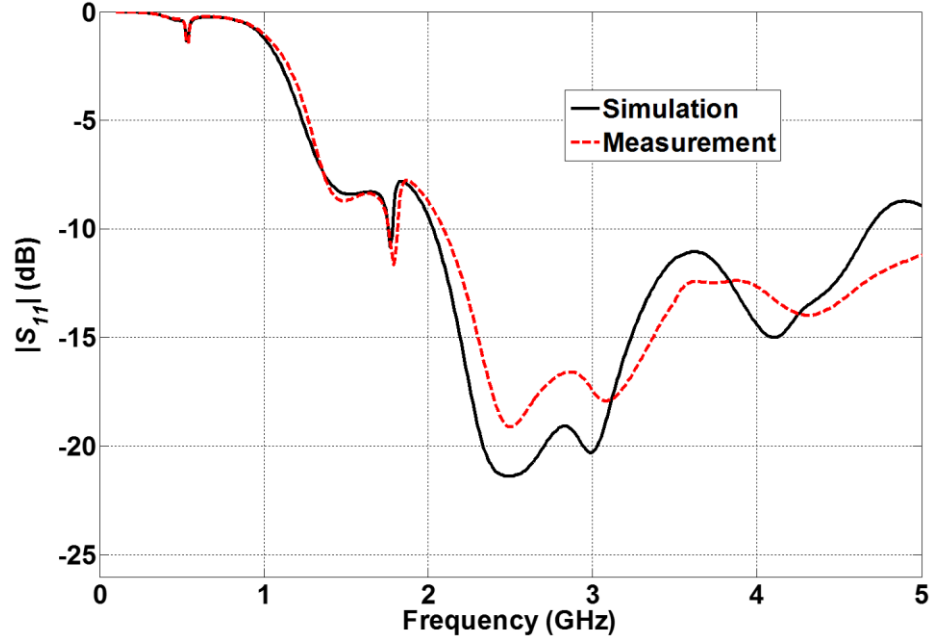


Figure 5.18. The simulated and measured S_{11} of the Nojima square CSA at the unfolded state.

Figure 5.19 shows the simulated 3-D radiation pattern of the Nojima square CSA at the unfolded state for 0.48 GHz and fully folded state for 2.5 GHz. Figure 5.19 illustrates that when the Nojima antenna is flat (i.e., unfolded), it resembles the pattern of an ordinary half wavelength dipole at 0.48 GHz corresponding to the antenna resonance shown in Figure 5.17. Figure 5.20 shows the simulated and measured azimuth and elevation gain patterns of the planar Nojima antenna. The measured peak realized gain is 1.8 dB and the Nojima antenna at this planar state is linearly polarized. Also, Figure 5.19 shows that when the Nojima antenna is folded, it exhibits a directional radiation. Our simulation results show that the peak gain is approximately constant in the operating frequency band 2.1 GHz - 3.5 GHz. Also, the shape of the 3-D radiation pattern stays directional, and the E-plane beamwidth varies from 123 ° to 172 ° in this frequency band.

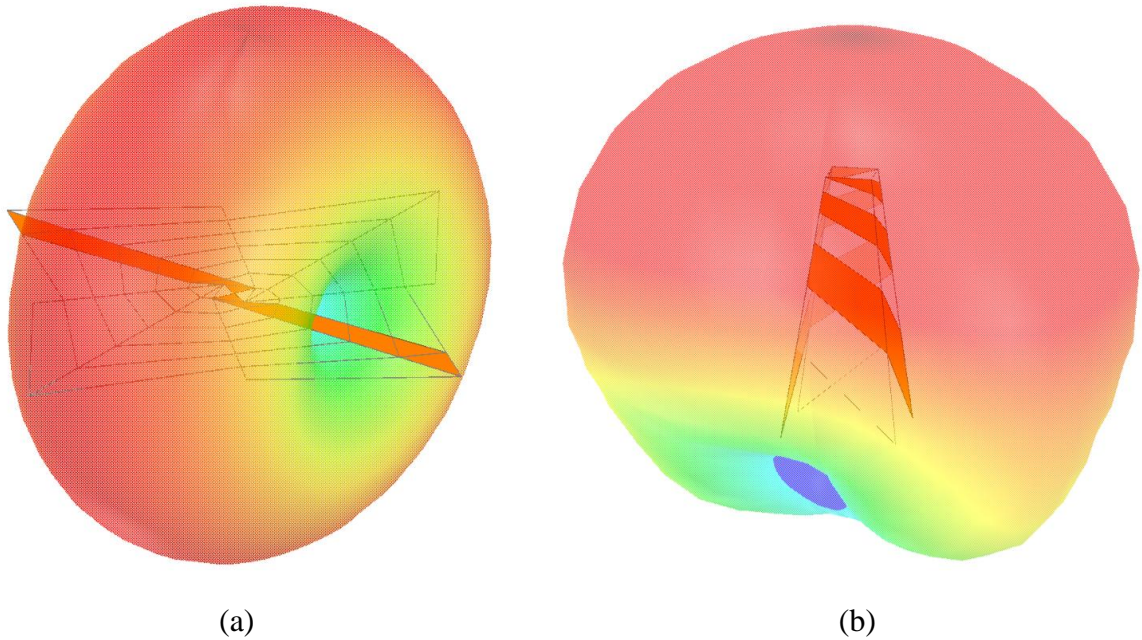


Figure 5.19. Simulated 3-D radiation pattern of the Nojima square CSA at (a) 0.48 GHz for unfolded state and (b) 2.5 GHz for folded state.

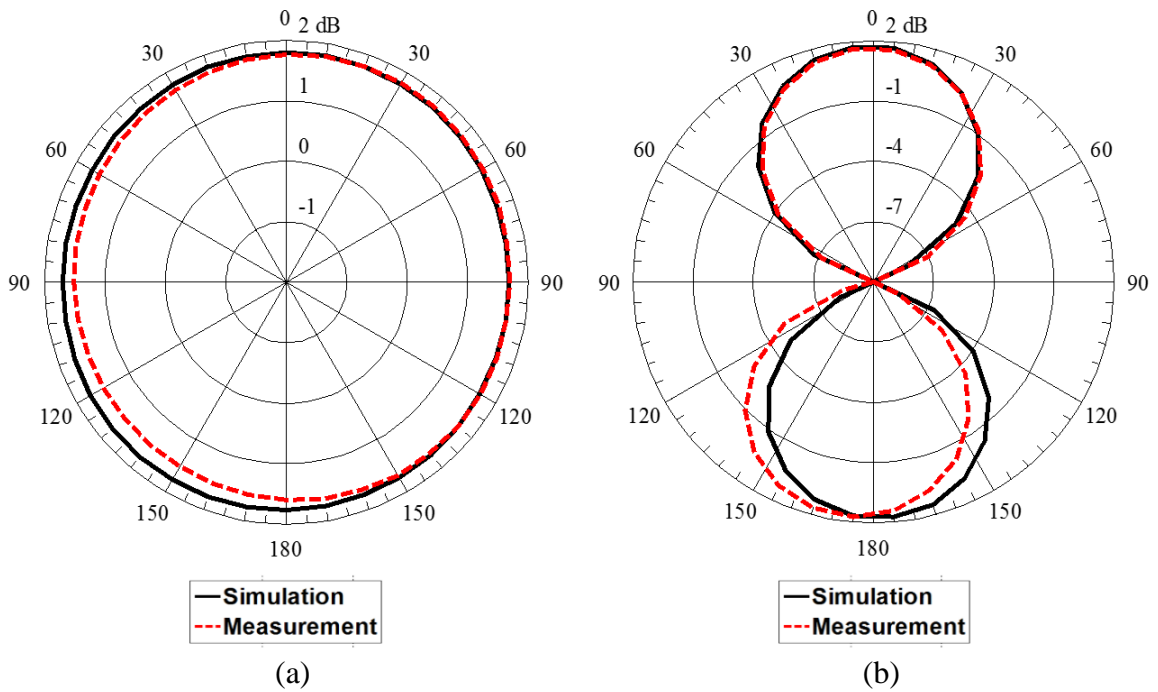


Figure 5.20. Simulated and measured realized gain pattern of the Nojima square CSA at unfolded state for (a) elevation plane when $\phi = 90^\circ$, and (b) azimuth plane.

Figure 5.21 shows the simulated and measured realized gain along the zenith direction versus frequency. It should be noted that the simulated results of the Nojima square CSA in Figure 5.9 and Figure 5.21 are different, since Figure 5.21 corresponds to the Nojima square CSA with a microstrip balun, whereas Figure 5.9 corresponds to the Nojima square CSA without a balun. Also, Figure 5.21 plots the realized gain of the origami CSA, which includes the effects of impedance mismatch, whereas Figure 5.9 plots the gain that does not include the effects of impedance mismatch. The prototype was measured in a StarLab anechoic chamber as shown in Figure 5.14(b). The measurement shows that the realized gain of the prototype is larger than 4 dB in the operating frequency band of 2.1 GHz to 3.5 GHz.

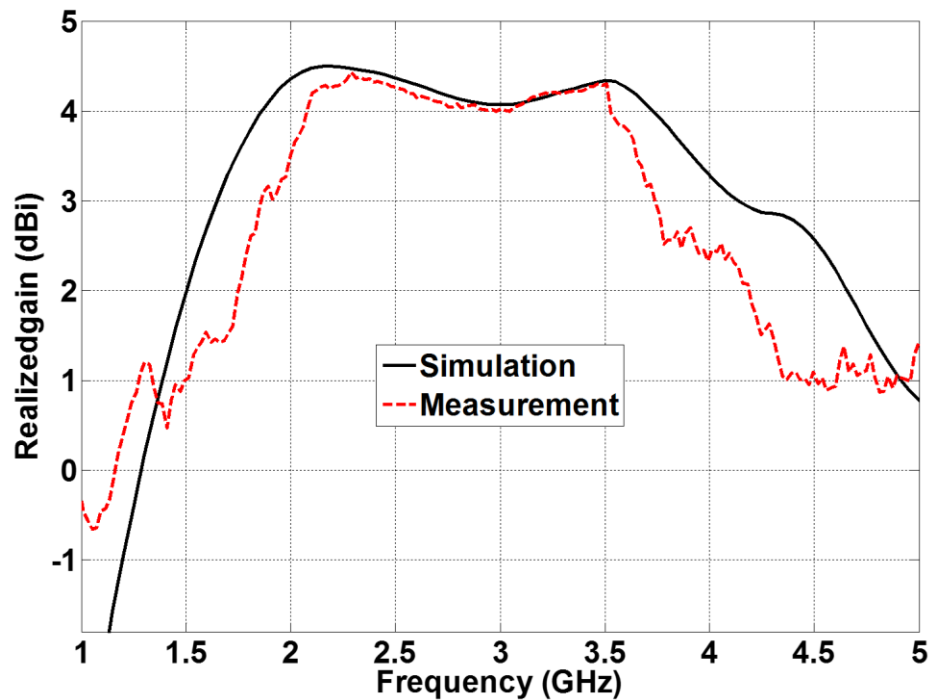


Figure 5.21. Simulated and measured realized gain along the $+z$ direction of the Nojima square CSA at the folded state.

Figure 5.22 shows the simulated and measured gain axial ratio along the $+z$

direction of the Nojima origami antenna at its folded state. The measured axial ratio is below 2 (i.e., 3 dB) in the operating frequency band of 2.1 GHz to 3.5 GHz, which agrees with the simulation results. This shows that the folded origami antenna (i.e., origami CSA) is circularly polarized. The slight disagreement between the measured and simulated reflection coefficient, realized gain and axial ratio of the fully folded antenna can be attributed to the fact that the simulation folded model is an ideal pyramid shape, which cannot be exactly realized by the prototype.

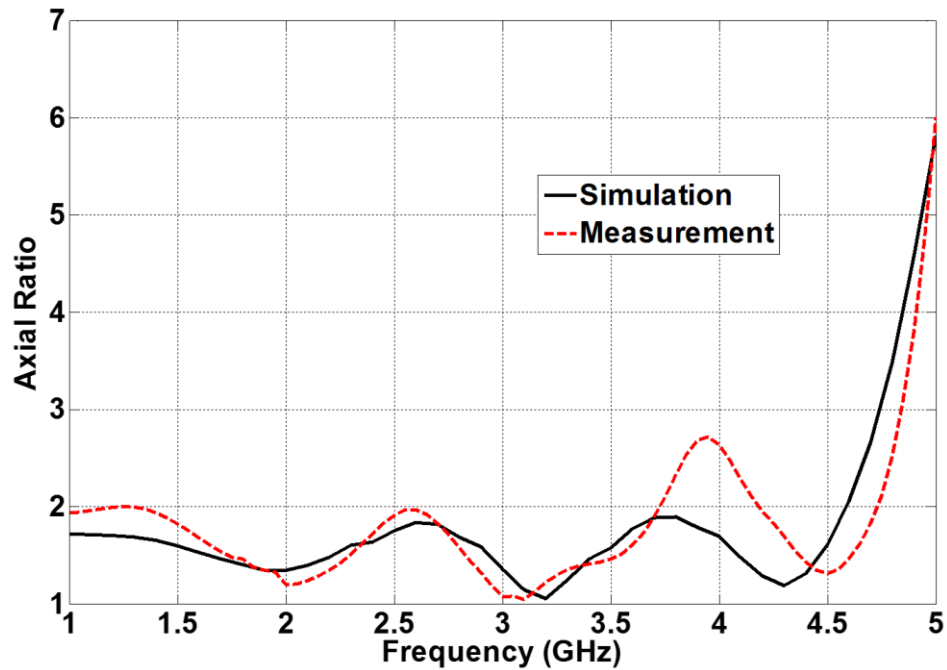


Figure 5.22. Simulated and measured realized gain axial ratio along the $+z$ direction of the Nojima square CSA at the folded state.

Figure 5.23 compares the simulated and measured normalized radiation pattern for the elevation planes of the antenna. Figure 5.23(a) and Figure 5.23(b) show the elevation patterns at 2.5 GHz for $\phi = 0^\circ$ and $\phi = 90^\circ$. Figure 5.23(c) and Figure 5.23(d) show the elevation patterns at 3 GHz for $\phi = 0^\circ$ and $\phi = 90^\circ$. The measured gain data illustrate that this prototype of the square central-hub Nojima origami CSA is directional toward the

zenith.

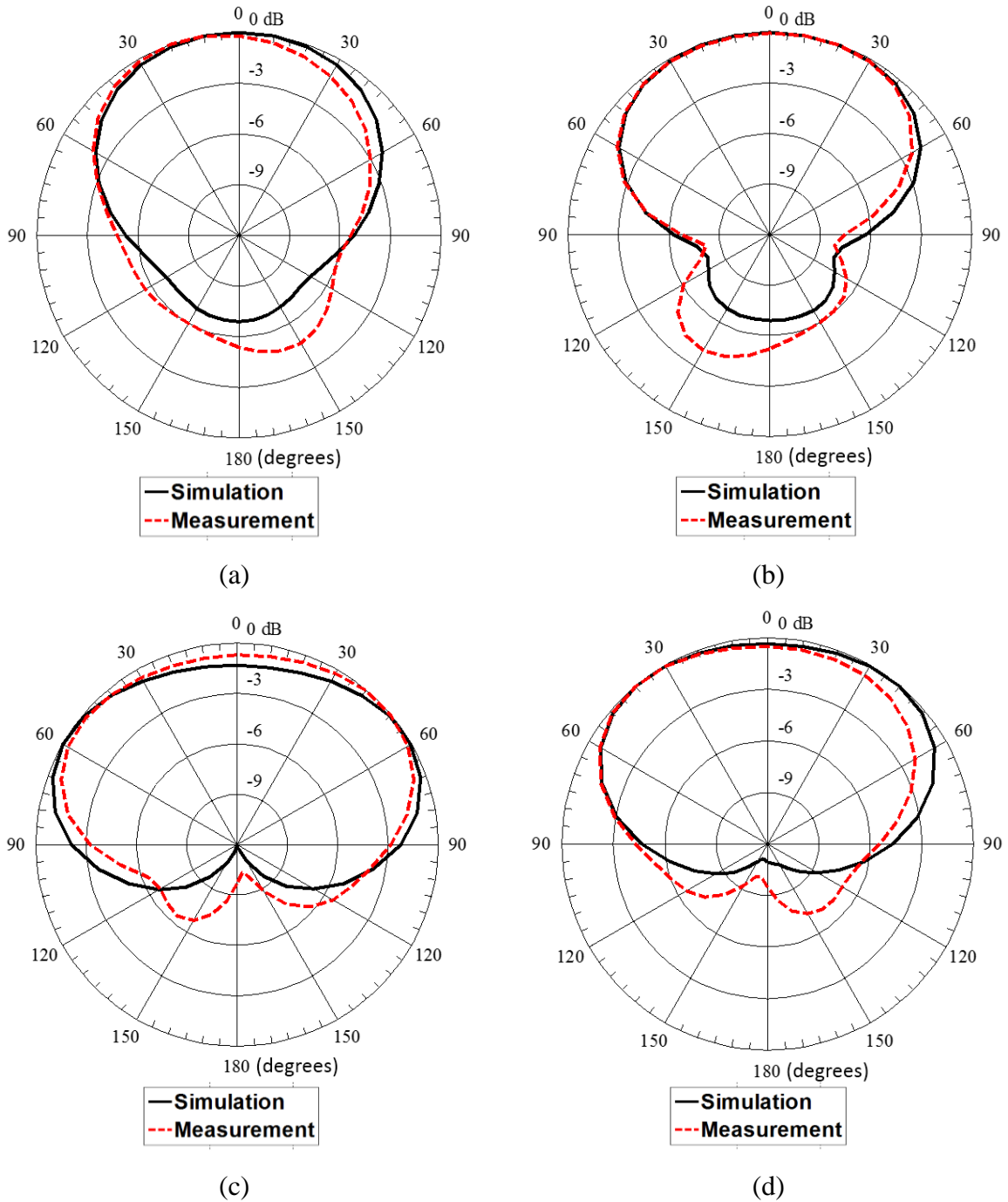


Figure 5.23. The simulated and measured realized gain patterns along the +z direction of the Nojima square CSA at the folded state for (a) 2.5 GHz, $\phi = 0^\circ$, (b) 2.5 GHz, $\phi = 90^\circ$, (c) 3 GHz, $\phi = 0^\circ$, (d) 3 GHz, $\phi = 90^\circ$.

The Nojima antenna can be folded and unfolded by pulling the ends of a pair of lines ① (see Figure 5.2). For example, the folding actuation mechanism can be realized by a gripper system, as used in Chapter 4. When the antenna is folded, the balun structure is totally inside the antenna, and the gripper structure can be placed on the top of the antenna. Each arm of the gripper is at least 150 mm and will be placed on the side of the antenna. The area of the step motor is 20 mm × 20 mm. The entire system can be packaged in a cylindrical space with 40 mm radius and 180 mm height. We have recently manufactured the origami antennas on 3-mil thick Kapton substrate and we are evaluating its performance and robustness. Our results on the evaluation of origami antennas on flexible substrates along with their actuation mechanisms will be presented in the future work.

5.5 Summary

In this chapter, a morphing Nojima origami antenna, which can transform itself from a planar dipole structure to a 3D conical spiral antenna structure, is presented. The angle parameters of the Nojima pattern are studied and the equations for designing 3-D Nojima CSAs are derived. Two quasi-equivalent geometrical models of traditional CSAs are developed. A prototype Nojima square CSA was manufactured to validate the design equations and simulation results. Our findings can be summarized as follows:

1. The 2-D Nojima pattern can be folded into a symmetrical 3-D multilateral conical structure. In this way, an omnidirectional linearly polarized dipole antenna can transform (i.e., morph) itself into a directional circularly polarized broadband conical spiral antenna, thereby providing reconfigurable antenna performance in terms of operating frequency, gain and radiation pattern.

2. This Nojima antenna design provides a new and more convenient way to construct polygonal conical spiral antennas on flexible and foldable substrates that exhibit similar performance to traditional conical spiral antennas.

The operating frequencies of the proposed origami CSA/dipole antenna can be changed when the physical dimensions of the origami antenna are modified. Since the dimension of the unfolded dipole is much larger than the folded CSA, it will cover a significantly lower frequency band (e.g., UHF band or lower band for satellite communication) than the lowest frequency of the CSA. Therefore, two transceiver systems have to be used; however, only one antenna is needed to cover both frequency bands, which is beneficial for space-borne and satellite applications as it will reduce the number of antennas needed in a platform. Our future research will concentrate on the development of a compact and robust deployment mechanism for this design. Also, the fabrication of origami CSAs on materials different than paper (e.g., flexible PCBs) is expected to become easier with future advancements in additive manufacturing.

The satellite communication bands are mainly in the UHF and SHF range. Separate antennas are mounted on modern satellites to cover the wide frequency bands [107]. Some ultra-wide band antenna (6.8:1 ratio bandwidth) [108] and antenna arrays (6:1 ratio bandwidth) [109], [110] have been developed recently. The physical sizes of these antennas are large. The proposed antenna prototype in this chapter is built with low-cost material, and it has small folded volume. The antenna works at both the UHF radar band (0.48 GHz) and the S-band (2.1 GHz - 3.5 GHz). All these technical parameters make it a good candidate for multi-band satellite antenna.

CHAPTER 6

ORIGAMI SEGMENTED HELICAL ANTENNA WITH SWITCHABLE SENSE OF POLARIZATION

In this chapter, a new design of a segmented helical antenna (SHA), which can switch its sense of polarization by rotating around its center axis, is presented. Two implementation methods (one based on origami folding and one based on skeleton scaffolding) are developed. Example bifilar SHA designs are presented for the UHF frequency band. The performance of the antennas is studied and validated through simulations and measurements. Specifically, the reflection coefficient, axial ratio, realized gain and radiation pattern beamwidth of the proposed SHAs are investigated and compared with the ones of a conventional bifilar helical antenna. Both SHAs exhibit high directional gain as conventional helical antennas. Both SHAs are circular polarized with small axial ratios (below 1.2 dB). The sense of the circular polarization of the SHAs can be switched from LHCP to RHCP by mechanical rotation around their central axis. Also, the SHAs can collapse to achieve high packaging ratios, which is very useful for satellite systems and in particular small satellites, e.g., CubeSats.

The techniques of reducing the size of the axial mode helical antennas (HAs) and polarization switching are briefly reviewed in Section 6.1. In Section 6.2, the hyperbolic paraboloid origami structure, which is used for this SHA design, is presented and analyzed. In Section 6.3, an origami SHA with switchable polarization is developed, and its performance is compared with the performance of conventional HAs. In Section 6.4, an SHA based on a skeleton scaffolding and with switchable polarization is described, this

design is inspired by the origami SHA. In Section 6.5, prototypes of the skeleton SHA are manufactured, and their performance is validated through simulations and measurements.

6.1 Introduction of Techniques for HA Volume Reduction and Polarization Switching

Axial mode conventional helical antennas have been widely used in satellite communications and global positioning systems due to their high gain and circular polarization. The properties of conventional helical antennas have been extensively studied. Segmented helical antennas, such as square cross section helical antennas, have been investigated in [111-113]. SHAs can provide approximately equivalent performance compared to the conventional helical antenna. The linear segments, which make up a SHA can be easily supported on a dielectric structure. This kind of structure can be designed and manufactured at a very low cost.

The physical size of helical antennas becomes considerably large at lower frequencies and requires a strong mechanical support. Several methods to reduce the total antenna volume have been developed and studied. A dielectric rod inside the helix was introduced in [114]. The volume of such antenna is tremendously decreased by 95%, but the gain is also decreased (below 4 dBi). Placing radial stubs along the circumference of the helix without affecting the radiation characteristics of the antenna was studied in [115-116]. The stubs increase the electrical length of antennas, and 40%-70% antenna volume reduction is achieved. However, the stubs change the input impedance of the antenna and a matching network is necessary in such designs. Meandering radiating elements of the helical antenna were used in [117-119]. The volume of these antennas was approximately

50% smaller compared to traditional helical antennas, but the axial ratio and the beamwidth of these antennas were compromised.

Deployable helical antennas for CubeSats have been investigated recently [74, 120-121]. Bifilar and quadrifilar HAs, which have better gain and lower beamwidth than a monofilar HA, are used in these designs. These antennas are composed of conductors that are supported by novel structures. This allows efficient folding, packaging, and deployment in space. Origami based helical antennas have been developed in [120-121]. The origami helical antennas have comparable performance to conventional helical antennas. Also, origami helical antennas can operate at different frequency bands by adjusting the height of the origami cylinders that support them.

Most circular polarized (CP) helical antennas only have one sense of polarization: right-hand circular polarization (RHCP) or left-hand polarization (LHCP). The sense of CP field of the helical antenna is determined by the direction of twist of the helix arms. In some applications, dual-band reception of both RHCP and LHCP signals are required. Dual sense CP antennas have been investigated, such as cross dipole antennas [122] and slot antennas [123]. In such antennas, the directions of the peak gain at the two states are opposite, and the gain is low (below 4 dBi). CP sense switchable antennas have also been developed in [124-125]. These antennas need extra switching circuits and power supplies.

6.2 The Hyperbolic Paraboloid Origami Unit for Origami SHA

The hyperbolic paraboloid origami structure, as shown in Figure 6.1, was originally developed in 1928 in Bauhaus [126]. This hyperbolic paraboloid can be created by taking a square piece of paper and folding the diagonals and concentric squares in alternating

direction, i.e., a square of mountain folds depicted in Figure 6.1(a) by the solid lines, followed by a square of valley folds depicted by the dash lines in Figure 6.1(a), and so on. After following this process, the paper pops automatically into a saddle curve [127]. Non-squares hyperbolic paraboloid origami structures have also been developed by Erik Demaine in [127].

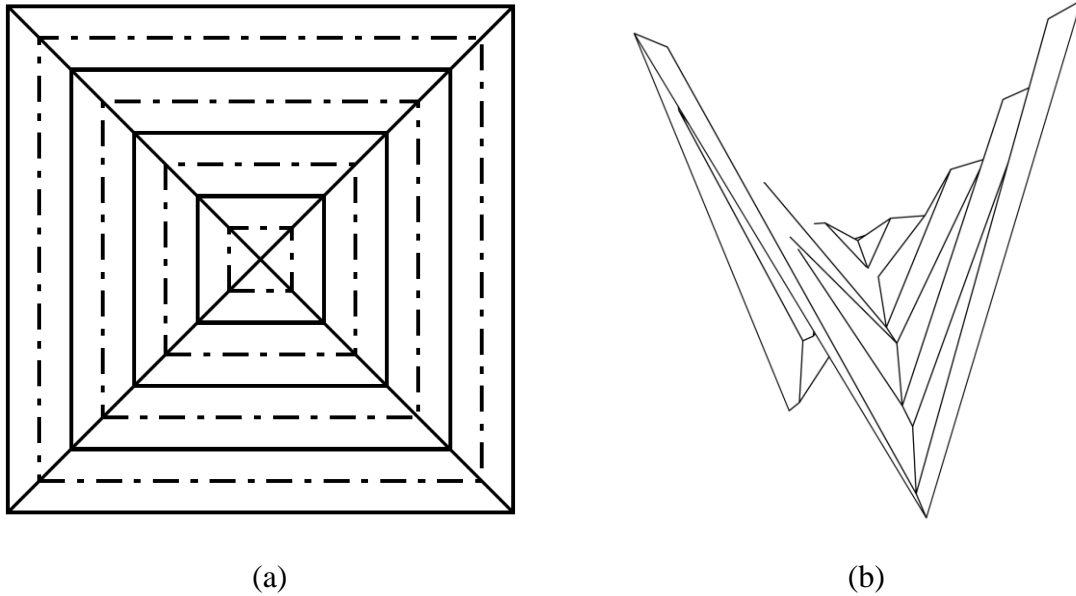


Figure 6.1. (a) Creased square pattern for hyperbolic paraboloid origami. (b) Hyperbolic paraboloid origami.

A new 3D structure can be developed by connecting several rectangle hyperbolic paraboloid origami structures in series, as shown in Figure 6.2. This structure can be used as a base for a new origami segmented helical antenna with switchable sense of polarization [128]. This new antenna consists of a series of identical rectangle hyperbolic paraboloid origami units where the two side edges of each unit have the segmented antenna trace, as shown in Figure 6.3 and Figure 6.4. This new antenna has two stable states (bi-stable design): a left-handed and a right-handed state. By fixing the bottom edge of each unit and rotating its top edge, each origami unit can pop from one state to the other.

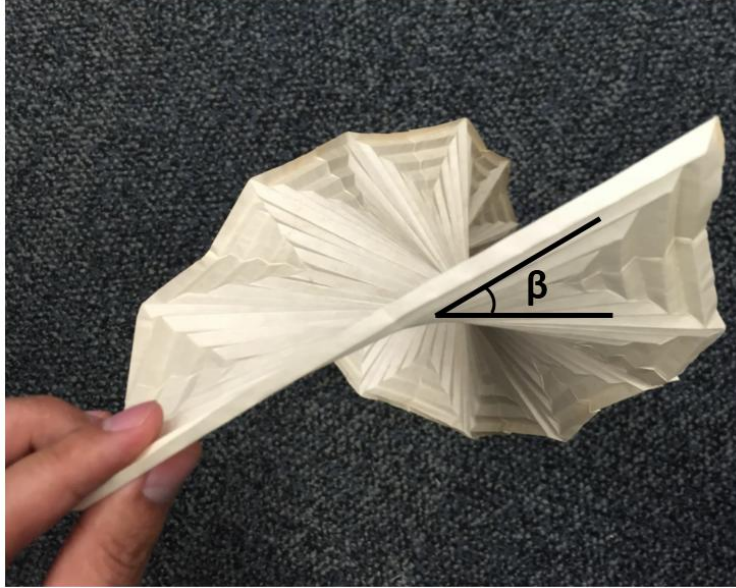


Figure 6.2. Origami paper base that can rotate around its center axis with multiple hyperbolic paraboloid units.

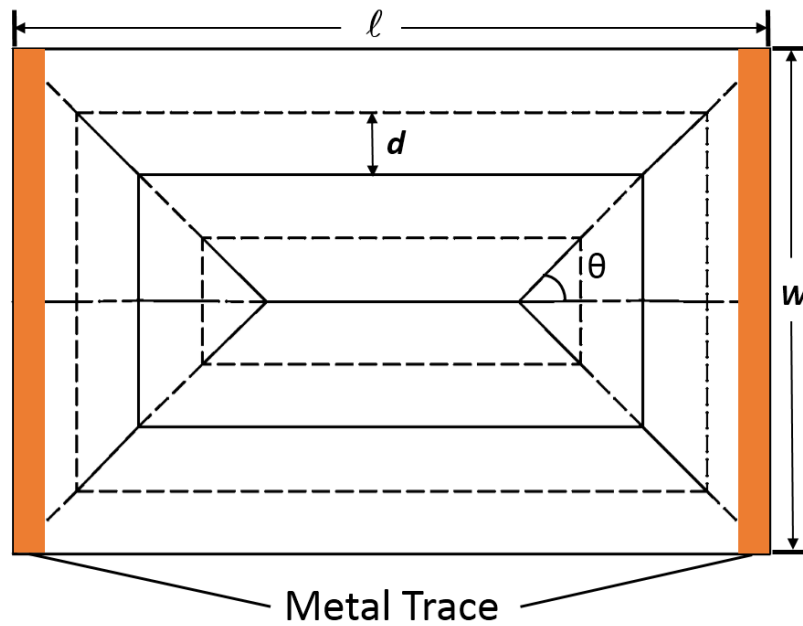


Figure 6.3. The origami rectangle unit pattern for the hyperbolic paraboloid with the antenna traces.

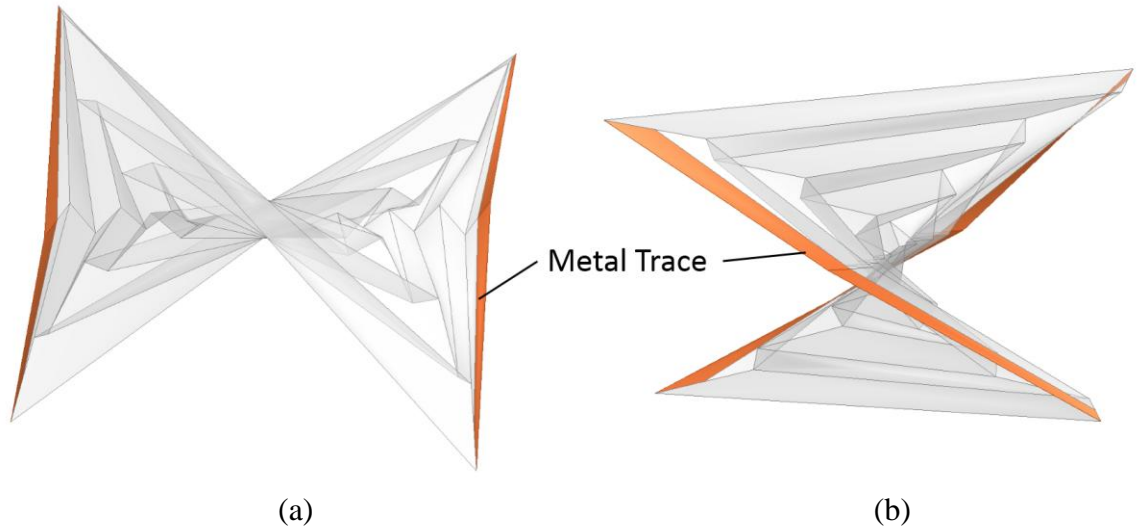


Figure 6.4. (a) Top view and (b) side view of a rectangle hyperbolic paraboloid origami unit with the antenna traces.

Figure 6.3 shows the rectangle origami unit. The solid lines are mountain-folds, and the dash lines are valley-folds. The lines of each rectangle alternate from solid to dashed. The length of each origami unit is ℓ , and the width of each origami unit is w . The number of rectangles in each unit is m , in Figure 6.3, $m = 4$. The distance d between the adjacent rectangles should be identical. The rotation angle β of each unit, which is shown in Figure 6.2, is determined by the ratio ℓ/w and the number m . The larger the ratio ℓ/w is, the smaller β will be. Also, the fewer rectangles in each unit, the smaller β will be.

When the angle θ , shown in Figure 6.2, equals 45° , the rectangle hyperbolic paraboloid origami unit can collapse its height. In this case, the origami unit can be compressed as a collapsible spring, as shown in Figure 6.5. This collapsible state of the paraboloid is not stable, but it can be used to stow the origami structure compactly and therefore it can be an intermediate non-operational state.

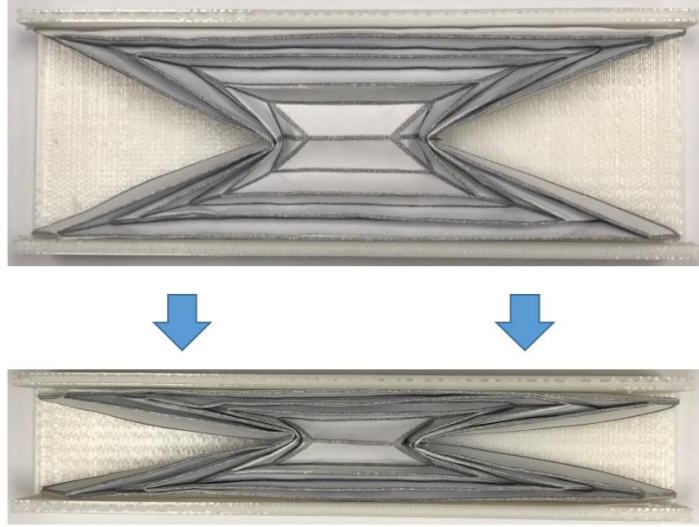


Figure 6.5. Rectangle hyperbolic paraboloid origami unit at the compact intermediate state for stowing.

For our example origami SHA design in this paper, which will be presented in next section, the length, ℓ , of the origami unit equals 100 mm. Each unit has 7 rectangles and a width, w , of 84 mm. The distance, d , is 6 mm, and the height of each folded unit is approximately 20 mm. The metal trace is attached along the two short sides of each rectangle origami unit. If the paper base has n rectangle origami units, then the total length of metal trace will be nw , and the number of turns, N , of the SHA will be

$$N = n\beta / 2\pi . \quad (6.1)$$

Materials with different thicknesses were tested for this origami unit. The origami base must be thick enough to mechanically support the hyperbolic paraboloid structure, but if it becomes too thick it will not be foldable. Figure 6.6 shows the rectangle hyperbolic paraboloid origami unit for the left-handed and right-handed states for different materials (paper and Kapton[®]) and different thicknesses. The thickness of the material has a small effect on the rotation angle β . The thicker the material is, the smaller β will be. From our

experiment results, the applicable thickness range for the commercially available paper without any coating is from 100 μm to 400 μm . For our example design in this paper, 100 μm -thick paper is used as the origami base. The rotation angle, β , of the 100 μm -thick paper origami unit is approximately 90°. The origami units that were built with Kapton® FPC film exhibit similar properties compared to the paper base. The applicable thickness range for the Kapton films is from 50 μm to 150 μm . The 2 mil-thick Kapton unit, shown in Figure 6.6(c) and Figure 6.6(d), has the biggest rotation angle β . The 5 mil-thick Kapton unit, shown in Figure 6.6(g) and Figure 6.6(h), has the most stable structure.

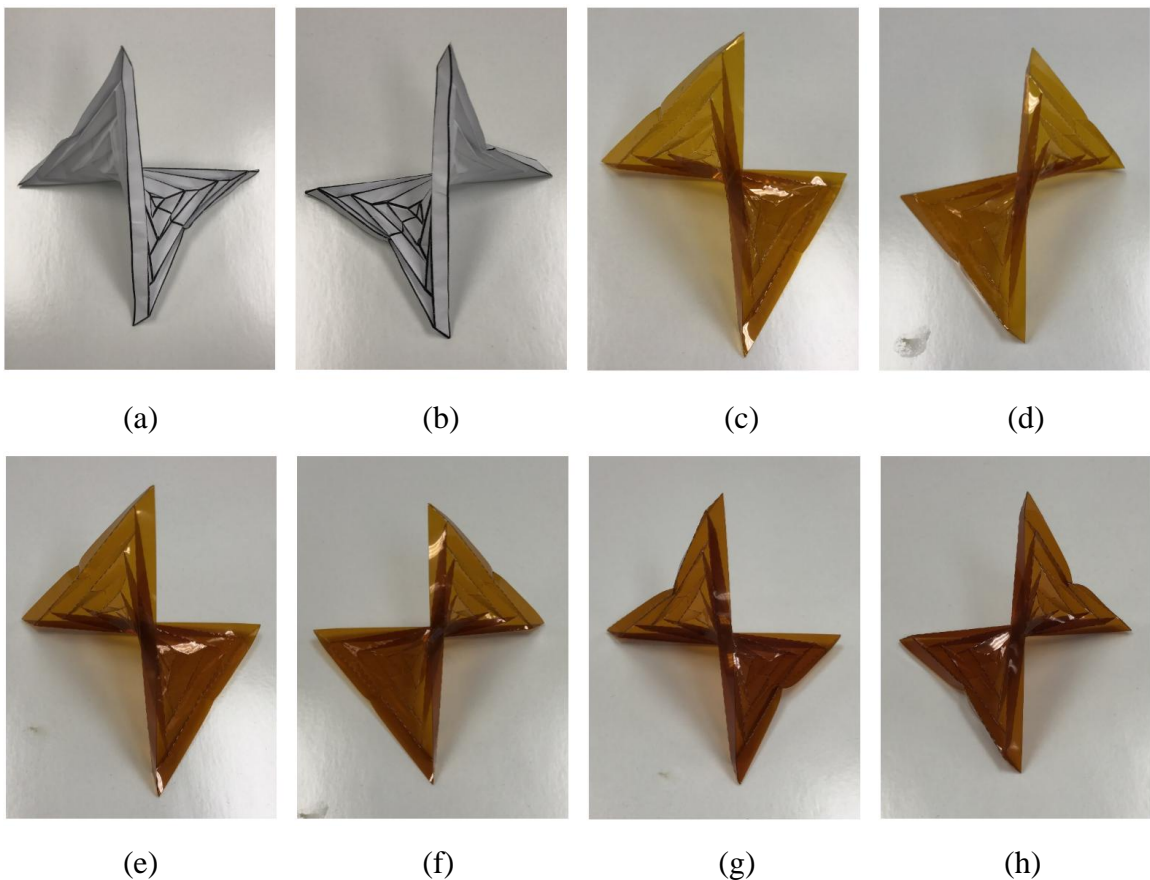


Figure 6.6. The hyperbolic paraboloid origami unit for (a) 150 μm -thick paper at left-hand state, (b) 150 μm -thick paper at right-hand state, (c) 50 μm -thick (2-mil) Kapton film at left-hand state, (d) 50 μm -thick (2-mil) Kapton film at right-hand state, (e) 76 μm -thick (3-mil) Kapton film at left-hand state, (f) 76 μm -thick (3-mil) Kapton film at right-

hand state, (g) 127 μm -thick (5-mil) Kapton film at left-hand state, and (h) 127 μm -thick (5-mil) Kapton film at right-hand state.

6.3 Origami Segmented Helical Antenna

In this section, an origami Segmented Helical Antenna (SHA) is developed using multiple connected in series rectangle hyperbolic paraboloid origami units, which were discussed in the previous section. This origami geometry will allow a right-handed SHA to be switched to a left-handed SHA by rotating all its origami units clockwise and the left-handed SHA to be switched back to the right-handed SHA by rotating all its origami units counterclockwise. Therefore, this origami SHA can provide a switchable sense of polarization.

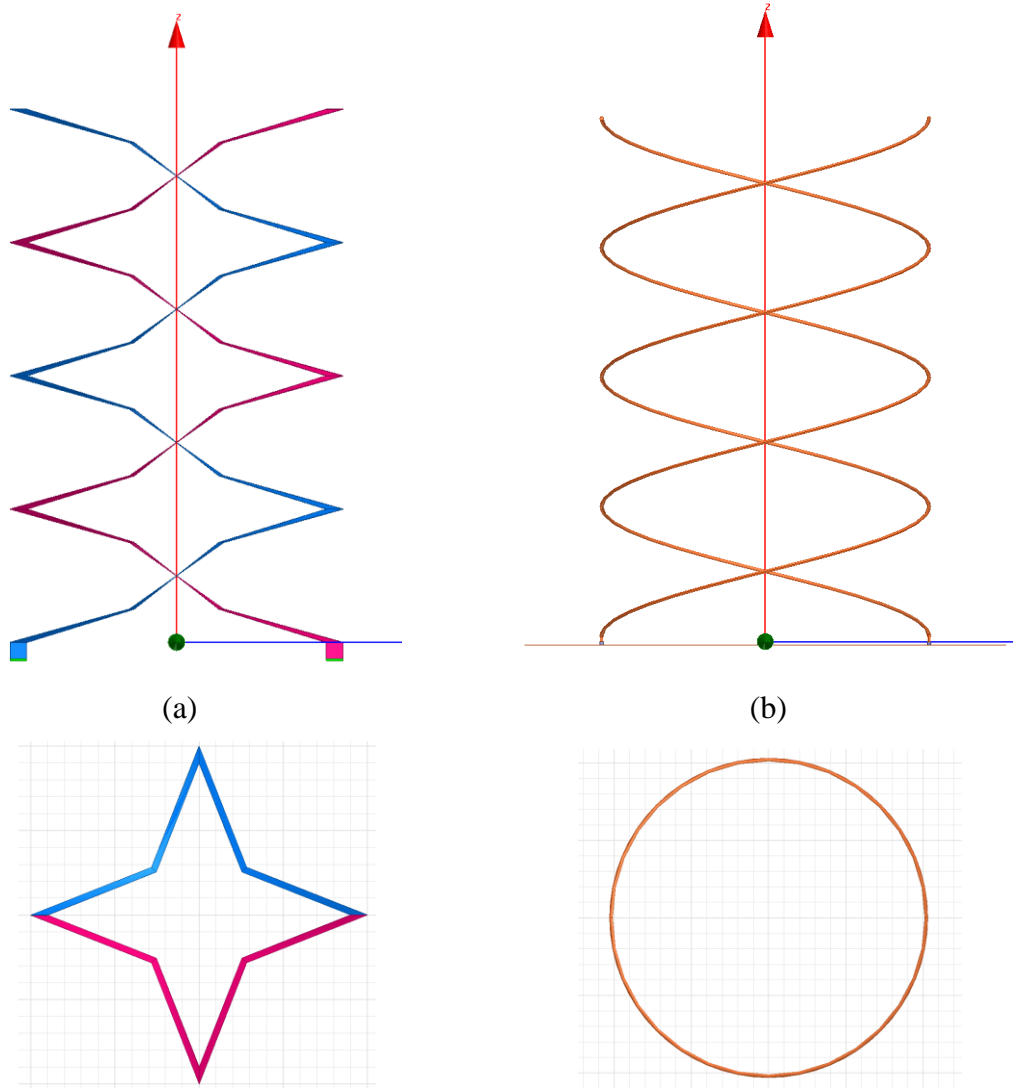
In this section and as an example, the performance of an origami bifilar SHA is investigated using simulations and measurements. The equivalent conventional bifilar helical antenna, which has the same diameter and height as the ones of the origami SHA, is analyzed and used as a reference.

Figure 6.7 shows the side and top views of the simulation models of the origami SHA and the conventional HA that will be examined. The origami paper base is not shown in Figure 6.7 in order to clearly show the antenna trace. The blue and red strips in Figure 6.7(a) and Figure 6.7(c) are the two metal traces of the SHA. Each metal trace is connected to a 50 ohm excitation. The two excitation ports have 180° phase difference. A 150 mm by 150 mm ground plane is used. This origami SHA is composed by 8 origami rectangle units ($n=8$). The rotation angle, β , of the each origami unit is 90°. The number of turns, N , of this SHA can be calculated from equation (6.1), which is two. The total height of the origami antenna is 160 mm, and the length of each metal strip is 672 mm. Figure 6.7(c) shows that

the cross section of this SHA is a symmetrical polygon with 8 edges. The length of each edge is 42 mm, which is half of the width of the origami unit. The pitch angle, α , of the origami SHA can be calculated by:

$$\alpha = \tan^{-1}\left(\frac{\text{Antenna Height}}{n \times w}\right). \quad (6.2)$$

which is 13.4° . The conventional HA, shown in Figure 6.7(b) and Figure 6.7(d), also has two turns. The circumference of the conventional HA is $\pi \ell$. The spacing, S , between each turn is 80 mm. Therefore, the pitch angle α for the conventional HA is calculated as 14.2° .



(c)

(d)

Figure 6.7. The side view of (a) the origami SHA, and (b) the conventional HA. The top view of (c) the origami SHA, and (d) the conventional HA.

Figure 6.8 shows the simulated reflection coefficient of the conventional HA and the origami SHA. It can be observed that the two curves are similar, and both antennas have several resonant frequencies.

Figure 6.9 shows the manufactured prototype at the left-handed state and the right-handed state. The prototype is constructed using 50 μm -thick copper tape on 100 μm -thick sketching-paper substrate without any coating. The copper tape is glued on the paper and creased with the paper, so that it will stay attached to the paper substrate when the antenna is rotating. The width of the copper trace is 3 mm. The two copper traces are fed using SMA connectors. The feeding network adopted for the prototypes used a broadband 180° hybrid coupler. A central support post is placed in the center axis of the origami structure, which goes through the center of each origami paper unit. An arm made of polylactic acid (PLA) is fixed on the top of this post, and glued at the top edge of the origami paper base, as shown in Figure 6.10 and Figure 6.11. The entire origami base can be rotated around its central axis by rotating the PLA arm. When the PLA arm rotates by $2N\pi$, which is 720° in this example design, the antenna switches from its right-handed state to its left-handed state.

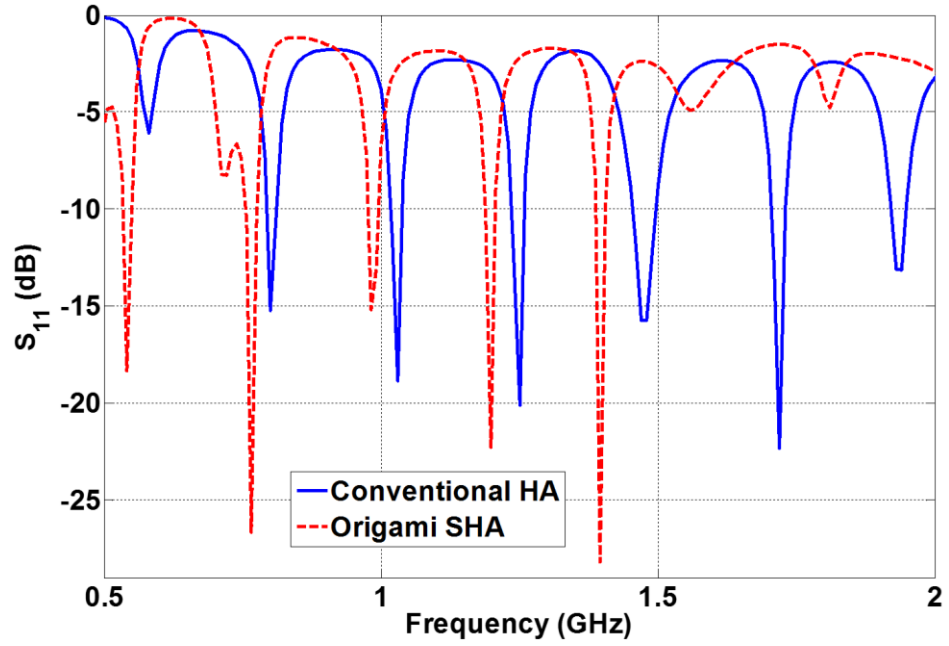


Figure 6.8. Simulated S_{11} of the conventional HA and origami SHA.

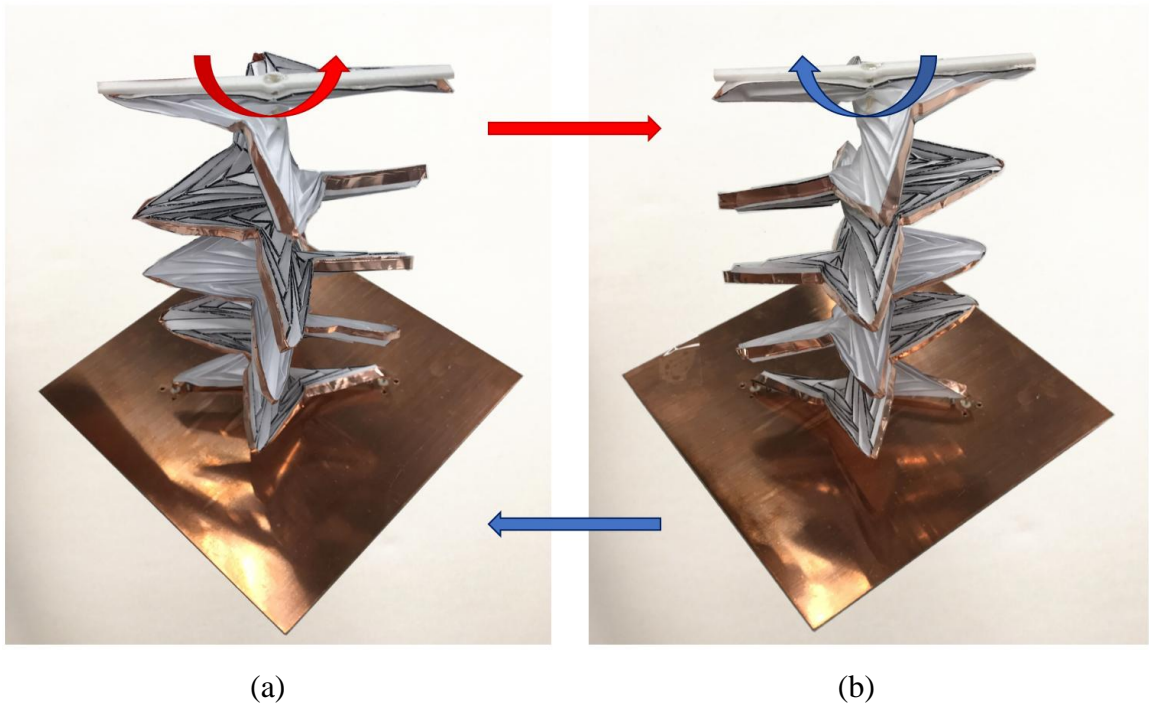


Figure 6.9. The manufactured prototype of origami SHA at (a) left-handed state and (b) right-handed state.

A telescoping metal post is used as a central support post of the origami SHA, as shown in Figure 6.10. From our simulation results, the metal post has negligible effects on the radiation properties of the origami SHA. The height of the antenna can be changed from 70 mm to 160 mm. The origami SHA can be tightly folded into a $100 \text{ mm} \times 70 \text{ mm} \times 5 \text{ mm}$ volume, as shown in Figure 6.10(c). Therefore, when telescopic post collapses, the volume of the origami SHA is decreased by 96% compared to the cylindrical volume of the conventional helical antenna.

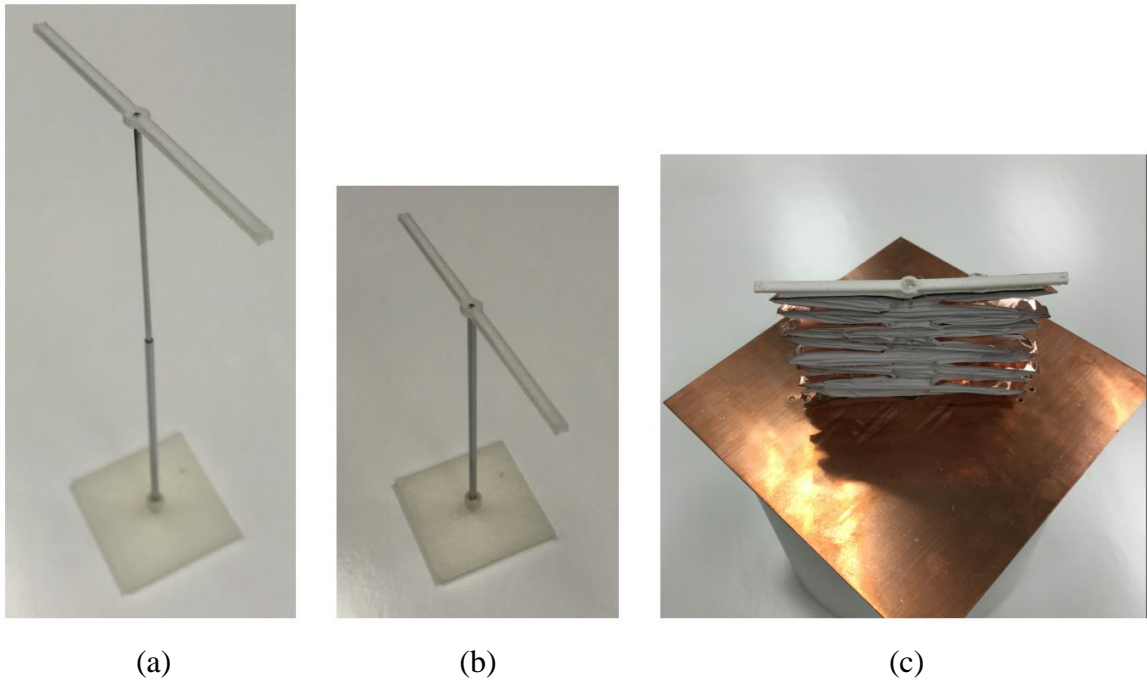


Figure 6.10. (a) Expanded telescoping central axis, (b) Collapsed telescoping central axis, (c) Tightly folded origami SHA.

The measured reflection coefficients and the simulation results for both the left-handed state and right-handed state of the origami SHA are shown in Figure 6.11. It can be seen that the two states have almost identical measured S_{11} -parameters and the origami SHA has four resonant frequencies from 0.7 GHz to 1.4 GHz. The origami SHA has a narrow operating frequency band. The simulated reflection coefficients at the four

operating frequencies are less than -15 dB. The measured S_{11} is less than -10 dB at the first three operating frequencies. The slight disagreement between the measured and simulated reflection coefficient is due to the fact that the simulated origami antenna is based on an ideal centrosymmetric model, which cannot be exactly realized by the prototype, since it was built manually. Also, the slight differences between the measured S_{11} -parameters for the two states can be attributed to the fact that the origami paper base is constructed manually and, therefore, the geometries of the two states are not identical.

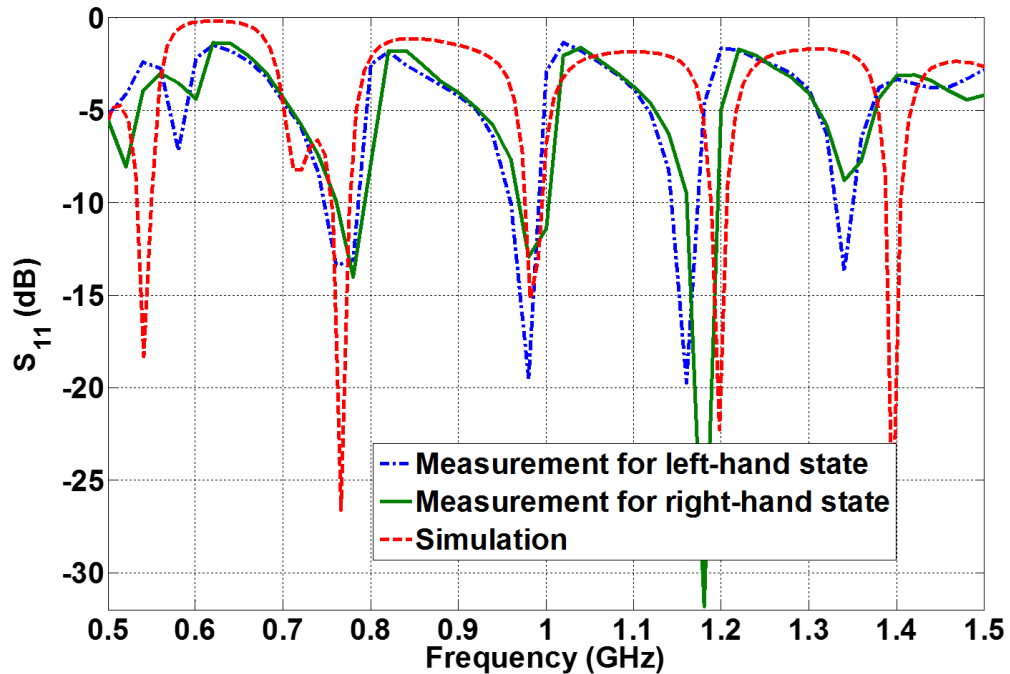


Figure 6.11. Measured S_{11} of the origami based SHA at both left-hand state and right-hand state.

Figure 6.11 shows that the origami SHA has four resonant frequencies from 0.77 GHz to 1.34 GHz. Also, this SHA exhibits directional gain performance at these frequencies as shown in Figure 6.12. Table 6.1 shows the measured far-field performance metrics of the prototyped origami SHA at the four frequencies. The far-field measurements were performed using a StarLab anechoic chamber. The results illustrate that the origami

SHA has the best axial ratio (0.94 dB) and highest co-polarization realized gain (6.82 dBi) at 0.98 GHz. The comparison of the far-field characteristics between the origami SHA and the conventional HA will be discussed in Section 6.5.

Table 6.1. Measured Far-field Characteristics of Origami SHA.

Far-field Characteristics	0.77 GHz	0.98 GHz	1.2 GHz	1.34 GHz
Axial Ratio	14.3 dB	0.94 dB	2.75 dB	4.46 dB
Co-polarization Realized Gain	2.68 dBi	6.82 dBi	5.35 dBi	5.77 dBi
Cross-polarization Realized Gain	-0.72 dBi	-9.28 dBi	-23.29 dBi	-6.22 dBi
E-plane HPBW	63 °	62 °	95 °	79 °
H-plane HPBW	82 °	69 °	91 °	84 °

Figure 6.12 shows the measured RHCP and LHCP elevation pattern of the origami SHA for $\varphi = 0^\circ$ and $\varphi = 90^\circ$ for both the left-handed and the right-handed states at 0.98 GHz. Figure 6.12 illustrates that the origami SHA works in the axial mode, and the maximum gain is along its central axis. The level of cross-polarization gain is approximately 16 dB lower than the co-polarization gain over the main beam direction. The shape of the radiation patterns at the two states are almost identical. The sense of polarization of this origami SHA can be switched from RHCP and LHCP by rotating the antenna around its axis to change the right-handed helix to a left-handed helix thereby providing a reconfigurable polarization.

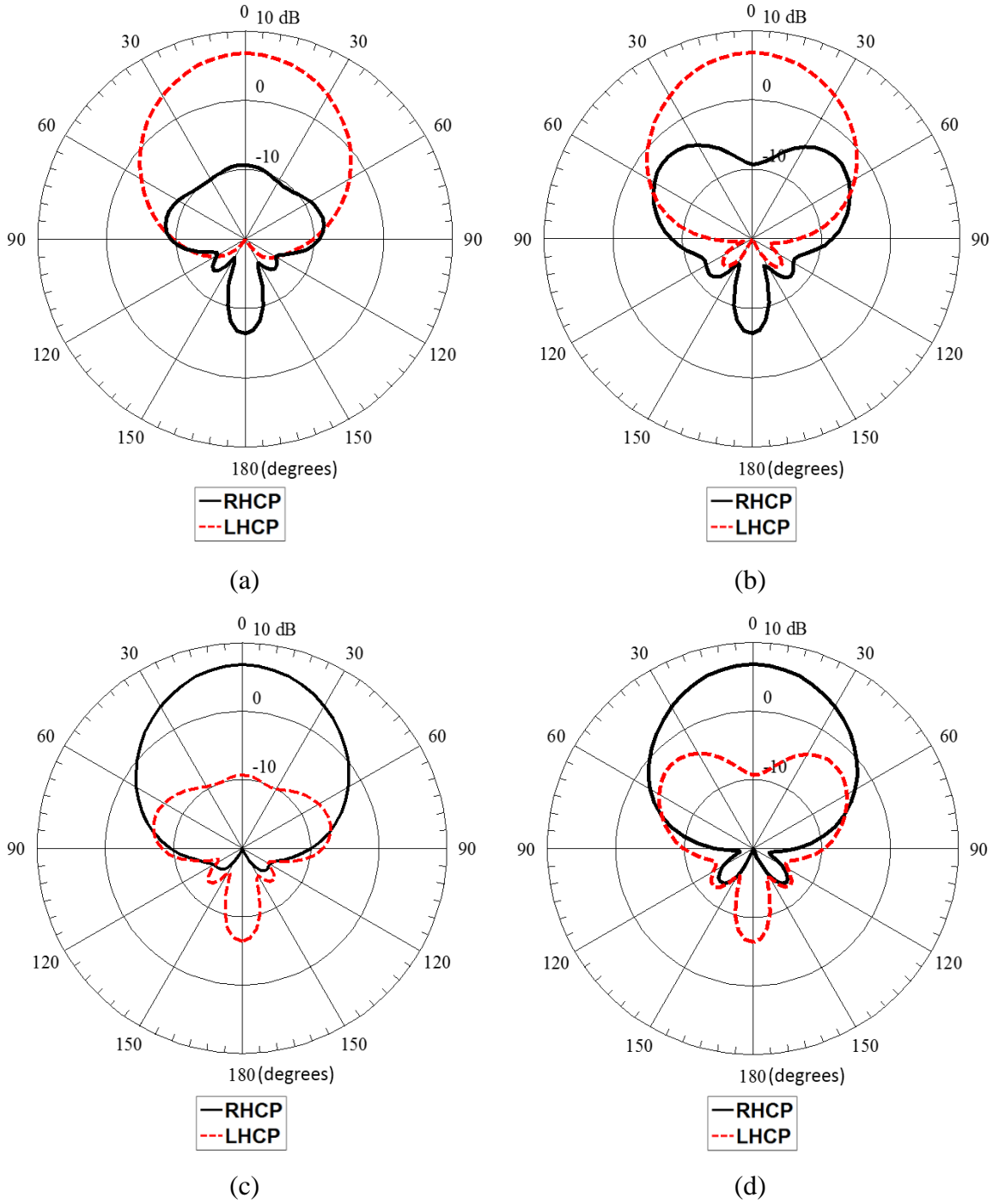


Figure 6.12. Measured elevation patterns of the origami SHA for the RHCP and LHCP components of the electric field at 0.98 GHz: (a) $\varphi = 0^\circ$ at the left-hand state, (b) $\varphi = 90^\circ$ at the left-hand state, (c) $\varphi = 0^\circ$ at the right-hand state, and (d) $\varphi = 90^\circ$ at the right-hand state.

As previously mentioned in Section 6.2, when the crease pattern is created and folded on the paper base, each origami paper unit will have a steady state. It could pop from left-handed state to the right-handed state with identical unit height and the rotation angle β , which ensures the stability of the geometry of the origami SHA. However, after the paper base is compressed and deployed as shown in Figure 6.10, we found that it is difficult for each origami unit to maintain the unified height. This is due to the nature of the paper material. To solve this problem, the skeleton scaffolding based SHA is presented in the next section. Also, other flexible materials will be studied by our future research.

6.4 Segmented Helical Antenna on Origami-Inspired Skeleton Scaffolding

Inspired by the origami SHA, which was presented in the previous section, a new SHA is developed based on a rotatable skeleton scaffolding. Figure 6.13 shows the unit of the skeleton scaffolding of this SHA. A cylindrical axis goes through the central hole of the arm, and the arm can rotate around this axis. There are circular holes at two ends of the arm. Copper wire feeds through these holes to construct the segmented helix. A hollow cylinder, which controls the unit height, is placed around the central axis between two adjacent arms. The arm and the hollow cylinder are shown in Figure 6.13, and they both can slide up and down along the central axis. The distance between the two holes of the arm is denoted as ℓ , which is geometrically equivalent to the length of the origami unit presented in Section 6.2. It also equals the length of the diagonal line of the segmented helix's cross section. The height of each unit is denoted as h . The thickness of the arm is denoted as t_1 , which determines the minimum volume of this antenna when it is collapsed (the collapsible skeleton SHA is presented in next section). The range of the rotation angle

β between adjacent arms is between 0° to 180° .

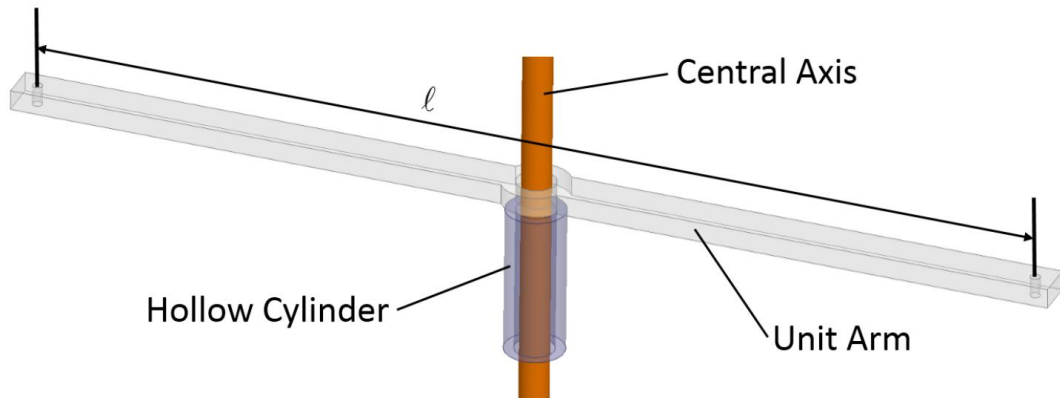
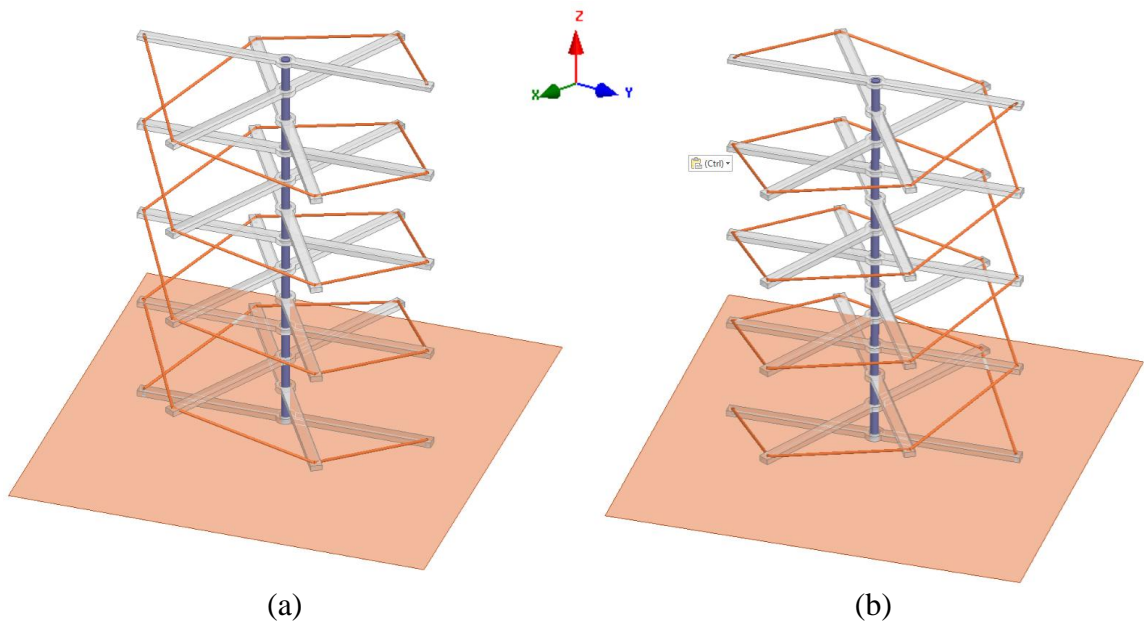


Figure 6.13. Unit of the supporting skeleton of the SHA.

As examples, two skeleton SHAs are designed here: a hexagon skeleton SHA and a square skeleton SHA. Both SHAs have the same geometrical size as the origami SHA presented in the previous section. The length, ℓ , of the arm is 100 mm, and the total height of the antenna is 160 mm. Their simulation 3-D models are shown in Figure 6.14 for both the right-handed and left-handed states. Both SHAs have a total of 2 turns.



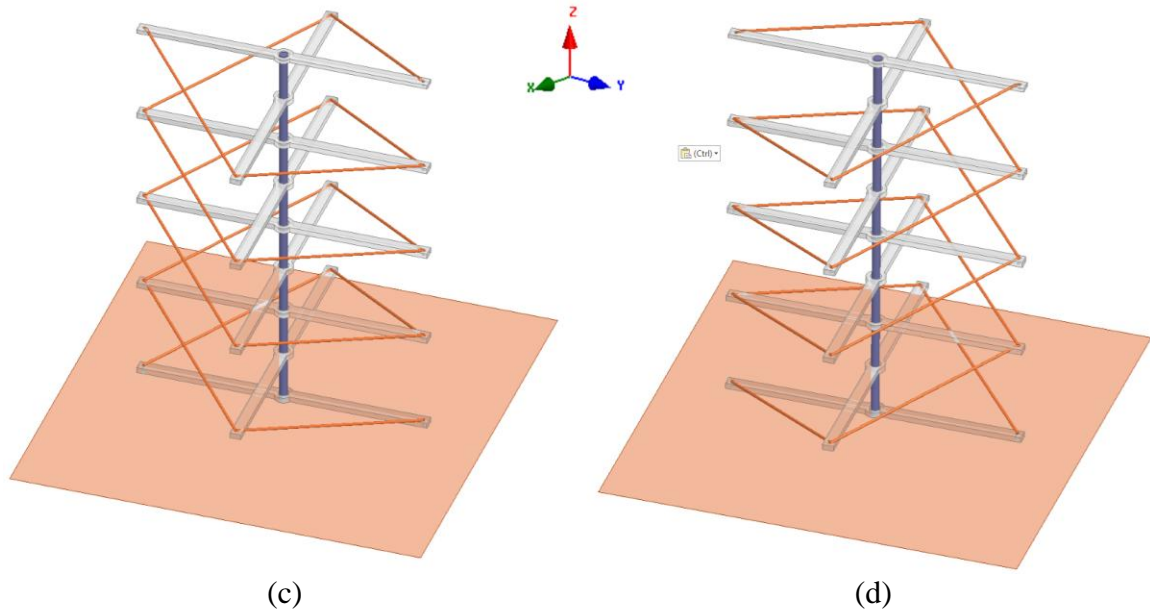


Figure 6.14. The simulation model of (a) the hexagon SHA at left-hand state, (b) the hexagon SHA at right-hand state, (c) the square SHA at left-hand state and (d) the square SHA at right-hand state.

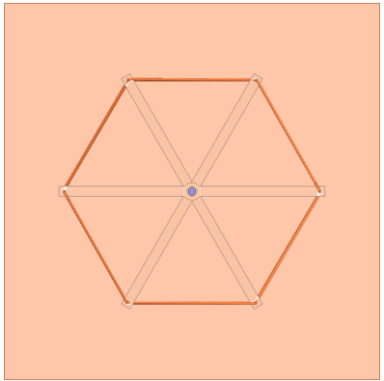
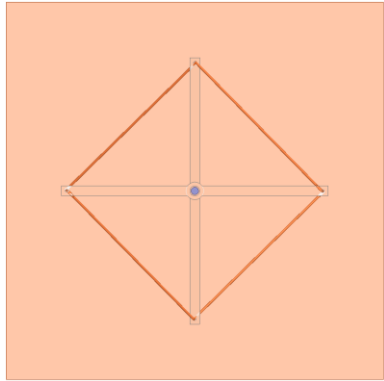
The thickness of each arm is 2mm. Copper wire with 0.4 mm diameter feeds through a hole at one end of one arm and through the hole at the end of the next arm. The symmetrical bifilar segmented helix structure is built with the skeleton arms. Each copper wire is connected at the base of the antenna to a 50 ohm excitation, and the other end of each copper wire is fixed on the top arm. The two excitation ports have 180° phase difference. A 150 mm by 150 mm square copper sheet is used as the ground plane. The skeleton SHA has two states: right-handed state and left-handed state. A right-handed skeleton SHA can be switched to a left-handed skeleton SHA by rotating the top arm 720° (two turns), while all the rest arms are dragged by the copper wire and rotate to the positions of the left-handed state.

One of the advantages of this symmetrical skeleton structure is that the whole skeleton can be rotated around the central axis by only rotating the top arm, while all the

rest arms are pulled by the copper wire to rotate. A right-handed skeleton SHA can be switched to a left-handed skeleton SHA by rotating the top arm 720° (two turns). Also, when the distances between adjacent arms are identical, the angles between adjacent arms will be identical. When the top arm is fixed on the central axis, a simple motor system can achieve the rotation operation.

Table 6.2 shows the geometric parameters of the hexagon and square skeleton SHAs that are shown in Figure 6.14. The square skeleton SHA has fewer arms, larger unit height and shorter copper wire length compared to the hexagon skeleton SHA. The pitch angle, α , of these two skeleton SHAs can be calculated by formula (6.2). The performance of the two antennas is examined in the next section.

Table 6.2. Geometry Parameters of the Segmented Helical Antenna.

Geometric Parameters	Hexagon Segmented Helical Antenna	Square Segmented Helical Antenna
Top View		
Number of Turns, N	2	2
Antenna Height	160 mm	160 mm
Number of Units, n	12	8
Angle Between the Adjacent Arms	60°	90°
Unit Height, h	13.3 mm	20 mm
Segment Length	51.75 mm	73.5 mm
Total Length of Each Copper Wire	621 mm	588 mm

6.5 Skeleton Segmented Helical Antenna Performance

In this section, prototypes of the two skeleton SHAs with the geometric parameters of Table 6.2 are built. Figure 6.15 shows the prototypes of the skeleton SHAs and the conventional HA. In order to make the conventional HA have the standard geometry, a 3 mm thick hollow cylinder base with helical groove lines is used as support. The central

axis, hollow cylinder, and arms of the skeleton scaffolding were printed with PLA filament using a 3D printer. The dielectric constant of the PLA is 2.5. The copper 26-gauge wire (0.409 mm diameter) used in the prototype is magnet wire with polyester coating. The thickness of the insulation layer is 0.023 mm. It should be pointed out that our simulation results show that the PLA cylinder base has negligible impact of the gain and polarization performance of the conventional HA, but it does shift its operating frequency approximately 8 MHz compared to the case with no base. The two segmented helical elements of each SHA antenna are fed using SMA connectors and with 180° phase difference between them. When the top arm rotates 720° , the entire segmented helical structure will rotate from its right-handed state to left-handed state.

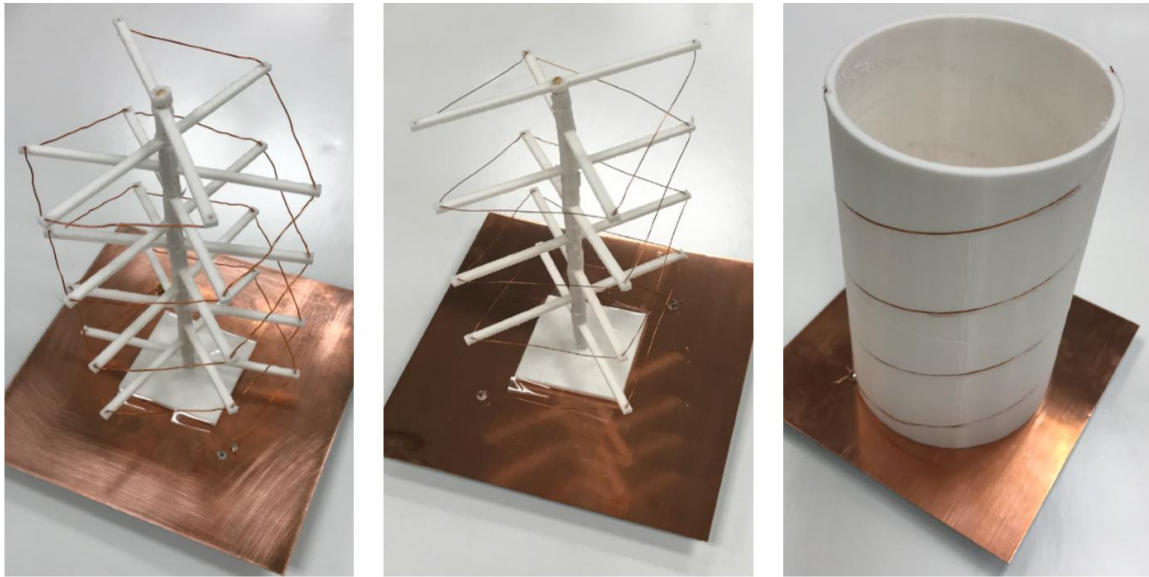


Figure 6.15. Manufactured prototype of the (a) hexagon skeleton SHA, (b) square skeleton SHA, and (c) conventional HA.

The measured performance characteristics of the proposed skeleton SHAs are compared with the ones of the origami SHA and the equivalent conventional bifilar HA in Table 6.3. All the antennas have the same diameter, height, and number of turns. The

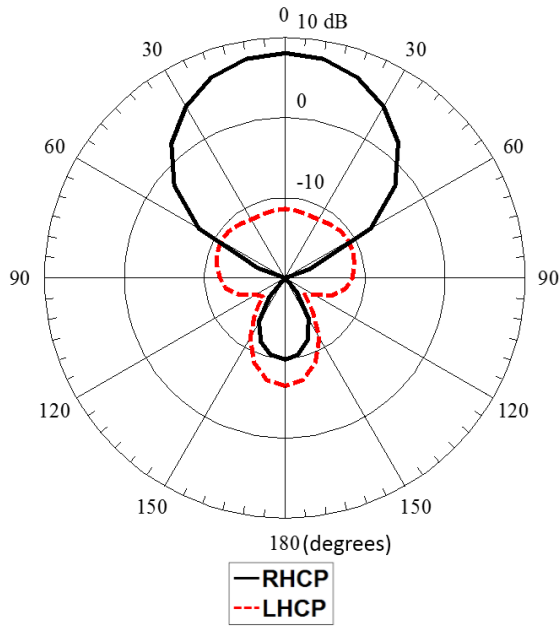
operating frequency of each antenna is picked so that it operates in axial mode and with the best axial ratio. From the results in Table 6.3, it can be concluded that all the SHAs have CP performance with small axial ratio (below 1.2 dB). The origami SHA has 1.4 dB lower gain, larger axial ratio and wider beamwidth than the corresponding ones of the conventional HA. The half-power beamwidths (HPBW) of the radiation pattern of the two skeleton SHAs are approximately the same to the ones of the conventional HA. The two skeleton SHAs have slightly lower realized gain and slightly larger axial ratio compared to the ones of the conventional HA. Also, since the circumference of the hexagon skeleton SHA has more sides than that of the square skeleton SHA, the hexagon skeleton SHA is geometrically more similar to the conventional HA and therefore, it is expected that the axial ratio and gain performances of the hexagon skeleton SHA will be more similar to the ones of the conventional SHA. The operating frequency of the origami SHA is approximately the same to the operating frequency of the conventional HA. Whereas, the operating frequencies of the skeleton SHAs are slightly higher than the operating frequency of the conventional HA. This happens because the circumference of the skeleton SHAs are smaller than the circumference of the conventional HA. The operating frequencies of the skeleton SHAs can be decreased by increasing the length of their arms.

Figure 6.16 compares the measured RHCP and LHCP elevation pattern for $\varphi = 0^\circ$ and $\varphi = 90^\circ$ for the skeleton SHAs at both the right-hand state and the left-hand state. The prototypes were measured in a StarLab anechoic chamber at the operating frequencies of the SHAs (i.e., the hexagon SHA was measured at 1.08 GHz, and the square SHA was measured at 1.16 GHz). It is evident that both antennas work in the axial mode, and the maximum gain is along their central axis. The level of cross-polarization gain is

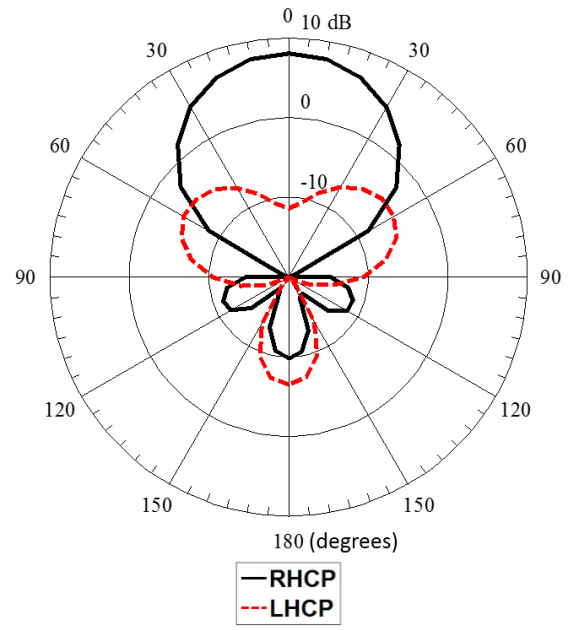
approximate 20 dB lower than the co-polarization gain over the main beam direction. The RHCP and LHCP gain can be switched when the skeleton SHAs are rotated from their right-handed state to their left-handed state. The slight difference between the pattern shapes at the two states can be attributed to the fact that the physical structure of the copper wire is not exactly the same at the two states.

Table 6.3. Comparison between the SHAs and the Conventional SHA.

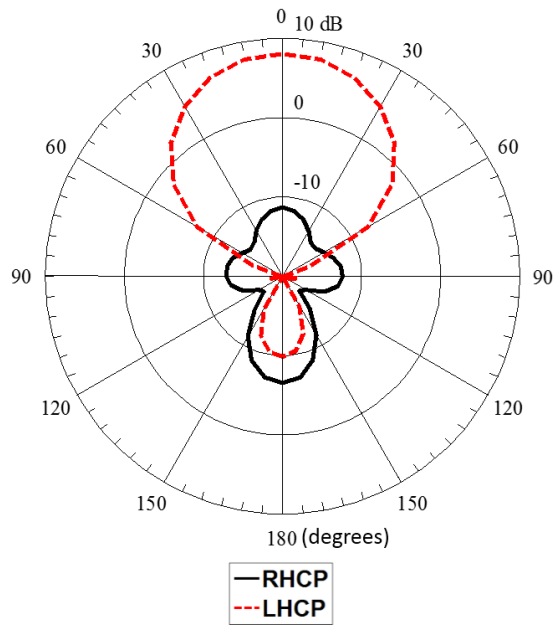
Antenna Characteristics	Skeleton Hexagon SHA	Skeleton Square SHA	Origami SHA	Conventional HA
Pitch Angle	14.4 °	15.2 °	13.4 °	14.2 °
Operating Frequency	1.08 GHz	1.16 GHz	0.98 GHz	1.03 GHz
Reflection Coefficient	-18 dB	-17 dB	-13 dB	-18 dB
Axial Ratio	0.74 dB	1.12 dB	0.94 dB	0.72 dB
Co-polarization Realized Gain	8.1 dBi	7.73 dBi	6.82 dBi	8.22 dBi
Cross-polarization Realized Gain	-11.32 dBi	-13.96 dBi	-9.28 dBi	-9.76 dBi
E-plane HPBW	55 °	58 °	62 °	57 °
H-plane HPBW	56 °	57 °	69 °	56 °



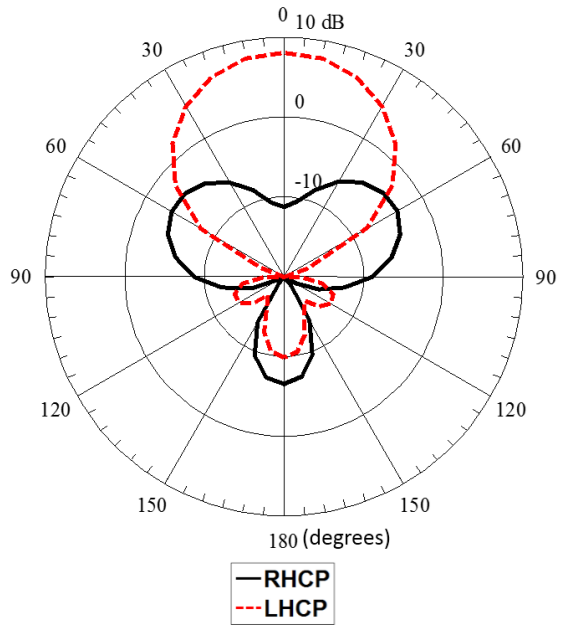
(a)



(b)



(c)



(d)

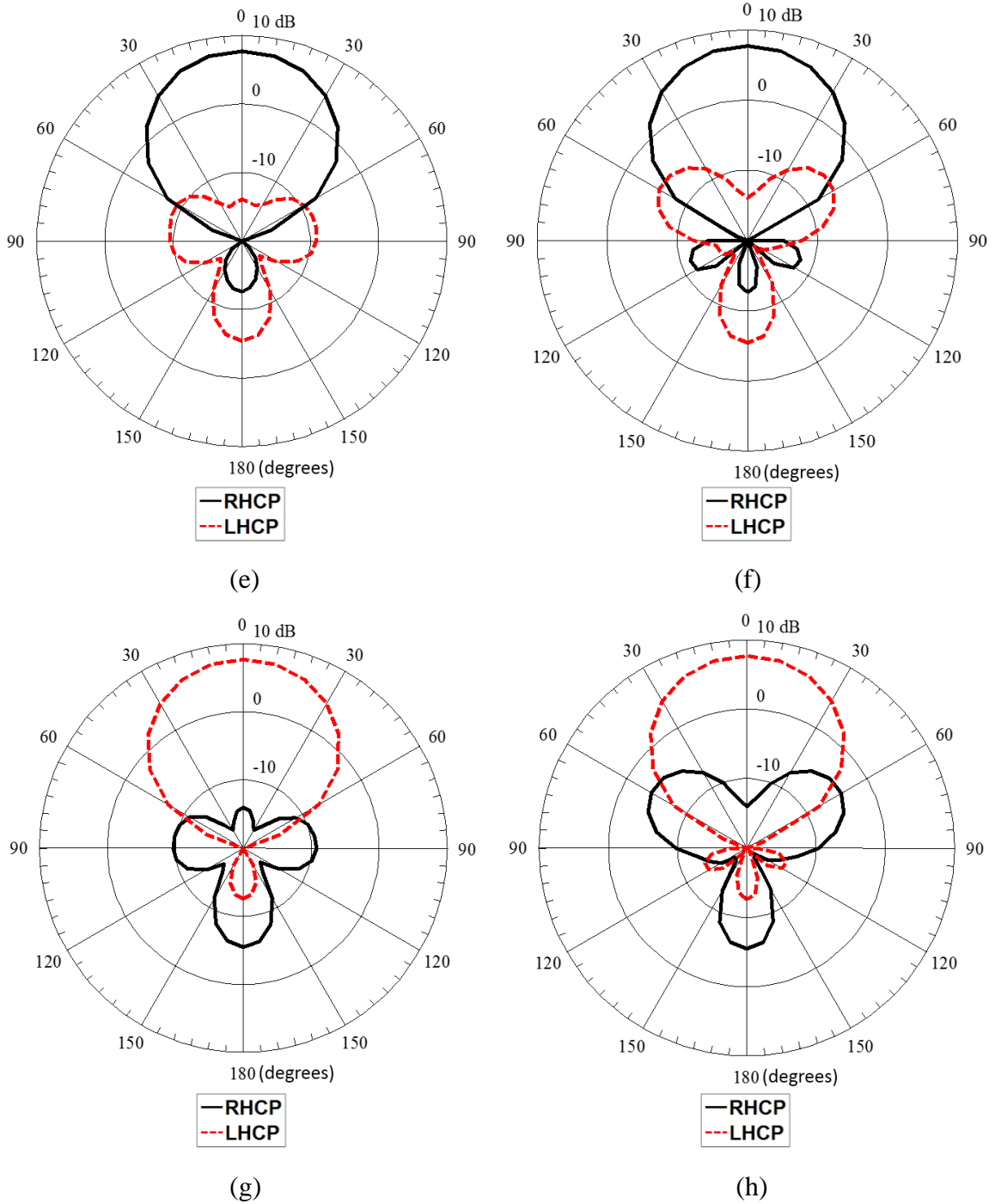


Figure 6.16. Measured elevation patterns for the RHCP and LHCP components of the electric field: (a) hexagon SHA for $\varphi = 0^\circ$ at the right-hand state, (b) hexagon SHA for $\varphi = 90^\circ$ at the right-hand state, (c) hexagon SHA for $\varphi = 0^\circ$ at the left-hand state, (d) hexagon SHA for $\varphi = 90^\circ$ at the left-hand state, (e) square SHA for $\varphi = 0^\circ$ at the right-hand state, (f) square SHA for $\varphi = 90^\circ$ at the right-hand state, (g) square SHA for $\varphi = 0^\circ$ at the left-hand state, and (h) square SHA for $\varphi = 90^\circ$ at the left-hand state.

The gain of helical antennas operating at the axial mode depends on the number of turns. Specifically, the gain increases as the number of turns increases. However, the gain does not increase linearly with the number of turns. In fact, for a large number of turns, an increase in the number of turns does not necessarily result in more directional radiation pattern [129]. Practical helical antennas have 5 to 15 turns. Table 6.4 shows the variation of the simulated gain versus the number of turns of our bifilar skeleton SHAs. From these simulation results, it is observed that increasing the number of turns beyond 10 turns does not significantly increase the gain of the SHAs. Also, higher gain can be achieved by using a reflector [121] or helical antenna arrays [130].

Table 6.4. Simulated Gain versus Number of Turns of the Bifilar Skeleton SHA

Number of Turns	2	4	6	8	10
Hexagon SHA Gain (dBi)	9.94	11.5	13.23	14	14.38
Square SHA Gain (dBi)	9.85	11.27	12.85	13.64	14.04

The skeleton based SHA is also a collapsible and deployable antenna like the origami SHA. A supporting mechanism is developed, as shown in Figure 6.17. Specifically, the hollow cylinders between the arms were removed and an additional hole was drilled on each PLA arm. The position of this hole is close to the central axis. A nonconductive thread is fed through the holes, and the thread is fixed on each arm. The thread pulls the arms upward sliding them along the central post when the antenna is expanded, and also sets the distance between adjacent arms. A telescoping metal post is used as the central axis. This design structure allows the antenna arms to rotate and the antenna to collapse or expand its

height. The minimum collapsed height of this skeleton SHA, shown in Figure 6.17(b), is approximately 17 mm, which make the antenna occupy 90% smaller volume compared to the volume of the completely expanded SHA. This is very useful for satellite antenna systems, where the SHA can be collapsed and stowed compactly during launch while it can expand when it reaches space.

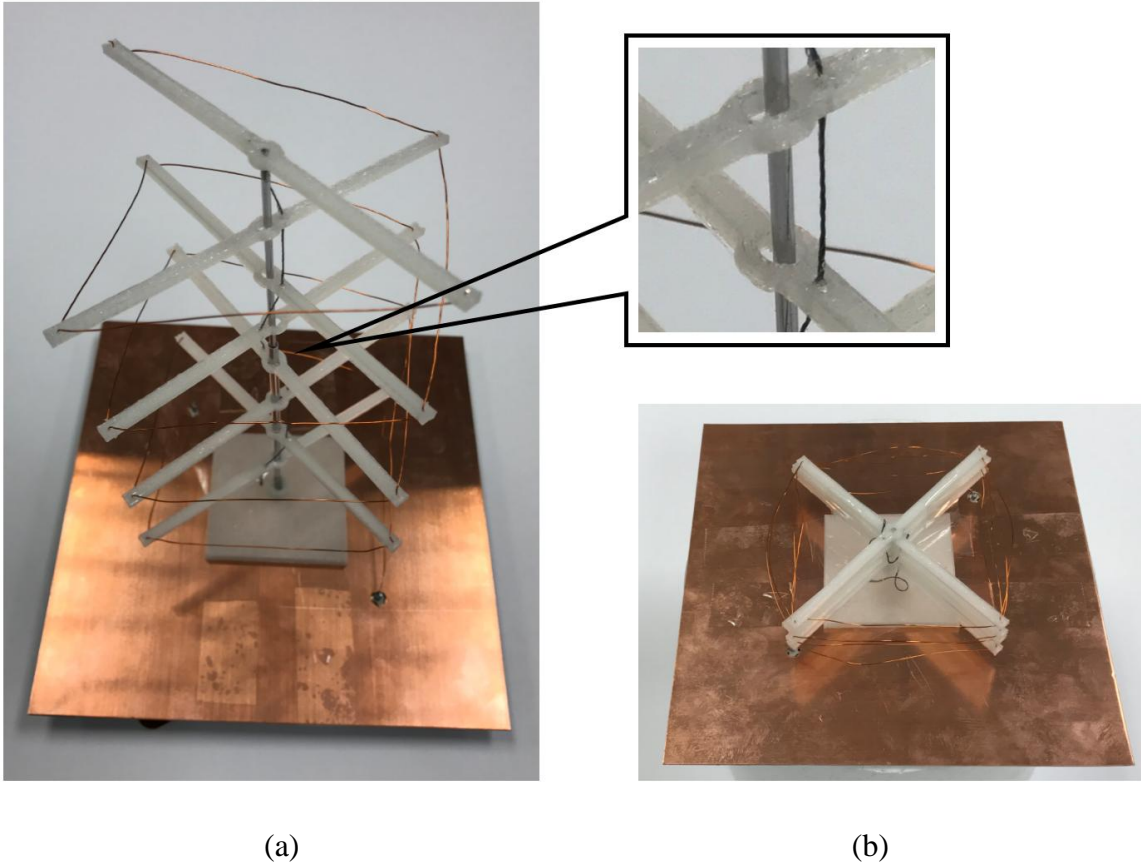


Figure 6.17. (a) Deployable skeleton scaffolding for square SHA. (b) Compressed square skeleton SHA.

CHAPTER 7

CONCLUSION AND FUTURE WORK

7.1 Conclusions

This dissertation presented research of origami applications on electromagnetic systems. Four types of origami structures are studied to build reconfigurable electromagnetic devices such as antennas, antenna arrays and reflectors. The practical process for designing reconfigurable origami antennas is demonstrated for the first time.

The origami accordion structure is presented in Chapter 3. The origami accordion has a large internal space generated from a thin sheet, and the antenna can be deployed on the shell, which makes the structure suitable for installation of components such as sensors and circuits. Also, that structure can be used for adjustable antenna reflector. The origami spring structure is studied in Chapter 4. The origami spring can be compressed into a very small volume, and its total length is adjustable. The biggest advantage of this structure is that the whole spring body can be controlled by pressing or stretching one of its levels. It's very convenient to design the actuation system for the origami body. In Chapter 5, the first antenna operating as an omnidirectional linearly polarized dipole antenna or as a directional circularly polarized wideband conical spiral antenna is presented. The design is based on a Nojima pattern, which wraps the 2-D material into a 3-D structure. All the design equations are developed based on the operating frequency band. In Chapter 6, designs of bifilar segmented helical antennas with the switchable sense of polarization are presented based on origami and skeleton scaffoldings. The antennas are circularly polarized with small axial ratios, and they can collapse to achieve high packaging ratios.

The origami structure changes its geometry naturally, and it can be compactly packaged into small volume. Besides its deployability and stowability, the origami structure provides a lot of possibilities for the reconfigurable electromagnetic system design. Origami antennas and origami electromagnetics are expected to impact a variety of applications related to communications, surveillance and sensing.

7.2 Future Work

All the origami designs presented in this dissertation are non-rigid origami, where deformation is allowed on each individual face and/or vertices and creases can move within the paper. The future work for this research is to develop rigid origami electromagnetic models. The rigid origami structure offers a purely geometric mechanism that can be realized at any scale because it does not rely on the elasticity of materials and is not significantly hindered by gravity [33]. The transformation of rigid origami from an unfolded state to a final configuration is controlled by a smaller number of degrees of freedom, which makes the equipment geometry more accurate and repeatable. Also, thick origami structure enables more choices for the manufacturing process for origami electromagnetic devices. For example, a PCB circuit can be a face of the origami body.

In addition, self-folding/deploying mechanisms are essential for the origami electromagnetic systems in the space application. For each origami design, the actuation system should be designed. A good actuation system will provide fast deployment speed and improve the strength-to-weight ratios. Active materials, which convert various forms of energy into mechanical movement, can be used as actuators.

More RF devices will be developed based on origami structures to support multiple services, such as frequency selective surface, RFID tag and waveguide. Also, novel manufacturing techniques and materials for origami RF devices, such as 3-D printing with liquid-metal-alloy, will be used for origami electromagnetic structures in the future.

REFERENCES

- [1] Y. Akira, “*Atarashii Origami Geijutsu*,” Tokyo: Origami Geijutsusha, 1954.
- [2] P. Engel, “*Origami from Angelfish to Zen*,” Dover Publications, 1994.
- [3] S. D. Guest and S. Pellegrino, “The Folding of Triangulated Cylinder, Part I, Geometric Considerations,” *J. of Appl.*, vol. 61, pp. 773-777, 1994.
- [4] B. A. Cipra, “In the Fold; Origami Meets Mathematics,” *SIAM News*, vol. 34, 2002.
- [5] T. Nojima, “Origami Modeling of Functional Structures based on Organic Patterns”, Kyoto University.
- [6] J. P. Gardner, et, “The James Webb Space Telescope,” *Space Sci. Reviews*, vol. 123, pp. 485-606, May 2006.
- [7] R. Hoffmann, A. K. Pickett, D. Ulrich, E. Haug, D. Lasry and J. Clinkemallie, “A Finite Element Approach to Occupant Simulation: the PAM-CRASH Airbag Model”, *Automotive frontal impacts*, pp. 79-87, 1989.
- [8] K. Kuribayashi, K. Tsuchiya, Z. You, D. Tomus, M. Umemoto, T. Ito and M. Sasaki, “Self-deployable Origami Stent Grafts as a Biomedical Application of Ni-rich TiNi Shape Memory Alloy Foil”, *Mater. Sci. Eng.*, vol. 419, pp. 131-137, 2006.
- [9] K. Kuribayashi, H. Onoe and S. Takeuchi, “Cell Origami: Self-Folding of Three-Dimensional Cell-Laden Microstructures Driven by Cell Traction Force,” *PLOS One*, vol. 7, issue 12, Dec. 2006.
- [10] D. Han, S. Pal, J. Nangreave, Z. Deng, Y. Liu and H. Yan, “DNA Origami with Complex Curvatures in Three-Dimensional Space,” *Sci.*, vol. 332, pp. 342-346, 2011.
- [11] S. Felton, M. Tolley, E. Demaine, D. Rus and R. Wood, “A Method for Building Self-Folding Machines,” *Sci.*, vol. 345, pp. 644-646, 2014.
- [12] J. Zhang, A. Wang and P. Wang, “A survey on reconfigurable antennas,” *IEEE Proc. Internat. Conf. Microw. Millimeter Wave Technol.*, no. 3, pp.1156-1159, 2008.
- [13] S. J. Mazlouman, A. Mahanfar, C. Menon and R. G. Vaughan, “A Review of Mechanically Reconfigurable Antennas using Smart Material Actuators,” *Proc. of the 5th European Conf. on Antennas and Propag.*, 2011.
- [14] S. V. Hum and J. P. Carrier, “Reconfigurable Reflectarrays and Array Lenses for Dynamic Antenna Beam Control: A Review,” *IEEE. Trans. Antennas and Propag.*, vol. 62, no. 1, pp. 183-198, Jan. 2014.

- [15] R. H. Patnam, "Broadband CPW-Fed Planar Koch Fractal Loop Antenna," *IEEE Antennas Wireless Propag. Lett.*, vol. 7, pp. 429-431, 2008
- [16] J. M. Hedgepeth and L. R. Adams, "Design Concepts for Large Reflector Antenna Structures," NASA Contractor Report 16134, 1983.
- [17] M. W. Thomson, "The Astromesh Deployable Reflector," *IEEE Proc. Antennas Propag. Soc. Internat. symp.*, no. 3, pp. 1516-1519, 1999.
- [18] X. Yan and F. Guan, "Structure-Electronic Synthesis Design of Deployable Truss Antenna," *Aerospace Sci. Technol.*, vol. 26, pp. 259-267, 2012.
- [19] Selding, P. "Boeing Finishes Deployment of Stuck SkyTerra 1 Antenna," *Space News*, Dec. 2012.
- [20] R. C. Gupta, S. K. Sagi, K. P. Raja, N. K. Sharma and R. Jyoti, "Shaped Prime-Focus Reflector Antenna for Satellite Communication," *IEEE Antennas Wireless Propag. Lett.*, vol. 16, pp. 1945-1946, 2017.
- [21] T. K. Sreeja, A. Arun and J. Jaya Kumari, "An S-band Micro-Strip Patch Array Antenna for Nano-Satellite Applications," *ICGT Internat. Conf.*, pp. 325-328, Trivandrum, India, Dec. 2012.
- [22] S. K. Podilchak, A. P. Murdoch and Y. M.M. Antar, "Compact, Microstrip-Based Folded-Shorted Patches: PCB Antennas for Use on Microsatellites," *IEEE Antennas and Propag. Magazine*, vol. 59, no. 2, pp. 88-95, 2017.
- [23] R. C. Brown, P. Clarricoats and Z. Hai, "The Performance of a Prototype Reconfigurable Mesh Reflector for Spacecraft Antenna Applications," *IEEE Proc. 19th Microw. Conf.*, pp. 874-878, 1989.
- [24] P. J. B. Clarricoats, A. D. Monk and H. Zhou, "Array-fed Reconfigurable Reflector for Spacecraft Applications," *IEEE Proc. Microw. Antennas Propag.*, vol. 141, pp. 531-535, 1994.
- [25] K. Tomiyasu, "Conceptual Reconfigurable Antenna for 35 GHz High-Resolution Spaceborne Synthetic Aperture Radar," *IEEE Trans. Aerosp. Electron. Syst.*, vol. 39, pp. 1069-1074, 2003.
- [26] J. Dong, Y. Li and B. Zhang, "A Survey on Radiation Pattern Reconfigurable Antennas," *IEEE Proc. 7th Internat. Conf. WiCOM*, 2011.
- [27] M. K. A. Rahim, M. R. Hamid, N. A. Samsuri, N. A. Murad, M. F. M. Yusoff and H. A. Majid, "Frequency Reconfigurable Antenna for Future Wireless Communication System," *Microw. Conf. (EuMC), 46th European*, Oct. 2016.
- [28] N. Robinson, "*The Origami Bible*," North Light Books, 2004.

- [29] R. J. Lang, “*The Complete Book of Origami: Step-by-Step Instructions in Over 1000 Diagrams/37 Original Models*,” Courier Dover Publications, 1988.
- [30] Wikipedia, “Origami,” [online]. Available: <https://en.wikipedia.org/wiki/Origami>
- [31] Z. Abel, J. Cantarella, E. D. Demaine, D. Eppstein, Thomas C. Hull, Jason S. Ku, Robert J. Lang and Tomohiro Tachi, “Rigid Origami Vertices: Conditions and Forcing Sets,” *J. of Computational Geometry*, vol. 7, no. 1 (2016): 171-184.
- [32] Cheng Lv, “Theoretical and Finite Element Analysis of Origami and Kirigami Based Structures,” Dissertation for the Doctor of Philosophy Degree, Arizona State University, August 2016.
- [33] N. Turner, B. Goodwine and M. Sen, “A review of origami applications in mechanical engineering,” *J. of Mechanical Eng. Sci.*, vol. 230, no. 14, pp. 2345-2362, 2016
- [34] R. J. Lang, “The Tree Method of Origami Design,” *Proc. of the 2nd Internat. Meeting of Origami Sci. and Technol.*, pp. 73–82, 1994.
- [35] R. J. Lang, “A computational algorithm for origami design,” *12th Annual ACM Symp. on Computational Geometry*, 1996.
- [36] M. D. Gregory and D. H. Werner, “Application of the Memristor in Reconfigurable Electromagnetic Devices,” *IEEE Antennas and Propag. Magazine*, vol. 57, no. 1, pp. 239-248, 2015.
- [37] Z. Tian, H. J. Qian and X. Luo, “Reconfigurable Dual-Band Bandpass Filter with Fully-Switch Operation Using $\lambda/2$ Folded-Resonator With Varactor-Loaded Open-Stub,” *IEEE Internat. Microw. Symp.*, pp. 918-921, Jun. 2017.
- [38] A. P. Deo, A. Sonker and R. Kumar, “Design of Reconfigurable Slot Antenna using Varactor Diode,” *Internat. Conf. on Commun. and Electron.*, pp. 511-515, Jul. 2017.
- [39] R. Simorangkir, Y. Yang, K. P. Esselle and Y. Diao, “A Varactor-Tuned Frequency-Reconfigurable Fabric Antenna Embedded in Polymer: Assessment of Suitability for Wearable Applications,” *IEEE Internat. Microw. Symp.*, pp. 204-207, Jun. 2017.
- [40] B. C. C. Chang, Y. Qian and T. Itoh, “A Reconfigurable Leaky Mode Patch Antenna Controlled by PIN Diode Switches,” *IEEE Proc. Antennas Propag. Soc. Internat. Symp.*, no. 4, 2694-2697, 1999.
- [41] D. Peroulis, K. Sarabandi and L. P. B. Katehi, “Design of Reconfigurable Slot Antennas,” *IEEE Trans. Antennas Propag.*, vol. 53, pp. 645-654, 2005.

- [42] S.V. Shynu, G. Augustin, C. K. Aanandan, P. Mohanan and K. Vasudevan, "Design of Compact Reconfigurable Dual Frequency Microstrip Antennas using Varactor Diodes," *Progress In Electromagn. Research*, vol. 60, pp. 197-205, 2006.
- [43] H. Rajagopalan, J. M. Kovitz and R. Rahmat-Samii, "MEMS Reconfigurable Optimized E-Shaped Patch Antenna Design for Cognitive Radio," *IEEE Trans. Antennas Propag.*, vol. 62, no. 3, pp. 1056-1064, 2014.
- [44] D. E. Anagnostou, M. T. Chryssomailis, B. D. Braaten, J. L. Ebel and N. Sepulveda, "Reconfigurable UWB Antenna With RF-MEMS for On-Demand WLAN Rejection," *IEEE Trans. Antennas Propag.*, vol. 62, no. 2, pp. 602-608, 2014.
- [45] A. Zohur, H. Mopidevi, D. Rodrigo, L. Jofre and B. A. Cetiner, "RF MEMS Reconfigurable Two-Band Antenna," *IEEE Antennas Wireless Propag. Lett.*, vol. 12, pp. 72-75, 2013.
- [46] D. V. Semeniknina, A. I. Semenikin and Y. V. Yukhanov, "Scanning Waveguide Antenna Array with MEMS Enabled Reconfigurable Frequency Selective Surfaces in Aperture," *IEEE Symp. on Wireless Tech. and Appl.*, pp. 96-99, Kota Kinabalu, Malaysia, Sep. 2014.
- [47] A. I. Semenikin, D. V. Semeniknina and Y. V. Yukhanov, "Modeling of MEMS Enabled Reconfigurable Frequency Selective Surfaces in Aperture of Waveguide Antenna Array," *Internat. Symp. on ANTEM*, pp. 145-148, Montreal, Canada, Jul. 2016.
- [48] H. Lago, M. F. Jamlos, S. Z. Aziz and N. A. Rhman, "A High Gain Reconfigurable Narrow Beam Steering Array (RNBSA) Antenna with MEMS," *IEEE Symp. on Wireless Tech. and Appl.*, pp. 116-120, Kota Kinabalu, Malaysia, Sep. 2014.
- [49] H. Lago, M. F. Jamlos, S. Z. Aziz and N. A. Rahman, "A Reconfigurable MEMS Beam Steering Array (RMBSA) Antenna for Smart RADAR Application," *IEEE Symp. on Wireless Tech. and Appl.*, pp. 96-99, Kota Kinabalu, Malaysia, Sep. 2014.
- [50] C. J. Panagamuwa, A. Chauraya and J. C. Vardaxoglou, "Frequency and Beam Reconfigurable Antenna Using Photoconducting Switches," *IEEE Trans. Antennas Propag.*, vol. 54, no. 2, pp. 449-454, 2006.
- [51] S. Pendharker, R. K. Shevgaonkar and A. N. Chandorkar, "Optically Controlled Frequency-Reconfigurable Microstrip Antenna with Low Photoconductivity," *IEEE Antennas Wireless Propag. Lett.*, vol. 13, pp. 99-102, 2014.
- [52] D. Ramachandran, A. Oz, V. K. Saraf, G. K. Fedder, T. Mukherjee, "MEMS-Enabled Reconfigurable VCO and RF Filter", *IEEE RFIC Symp. Dig.*, pp. 251-254, June 2004.

- [53] J. Reinke, A. Jajoo, L. Wang, G. Feddr and T. Mukherjee, "CMOS-MEMS Variable Capacitors with Low Parasitic Capacitance for Frequency-Reconfigurable RF Circuits," *IEEE Radio Freq. Integr. Circuits Symp.*, pp. 509-512, Boston, MA, Jun. 2009.
- [54] B. Ghassemiparvin, S. Shah and N. Ghalichechian, "Novel Paraffin-based 100-GHz Variable Capacitors for Reconfigurable Antennas," *European Conf. on Antennas and Propag.*, pp. 3506-3510, Paris, France, Mar. 2017.
- [55] F. Yang and Y. Rahmat-Samii, "A Reconfigurable Patch Antenna Using Switchable Slots for Circular Polarization Diversity," *IEEE Microw. Wireless Components Lett.*, vol. 12, no. 3, pp. 96–98, Mar. 2002.
- [56] M. K. Fries, M. Gräni, and R. Vahldieck, "A Reconfigurable Slot Antenna with Switchable Polarization," *IEEE Microw. Wireless Components Lett.*, vol. 13, no. 11, pp. 490–492, Nov. 2003.
- [57] X. X. Yang, B.-C. Shao, F. Yang, A. Z. Elsherbeni, and B. Gong, "A polarization Reconfigurable Patch Antenna with Loop Slots on the Ground Plane," *IEEE Antennas Wireless Propag. Lett.*, vol. 11, pp. 69–72, 2012.
- [58] N. Brennan, G. H. Huff, B. Rupp, M. A. Bevan, S. A. Long and W. M. Dorsey, "A Fluidic-Enabled Polarization Reconfigurable Antenna on a Hexagonal Substrate Tile," *IEEE Antennas Propagat. Soc. Internat. Symp.*, pp. 1642-1643, Orlando, FL, Jul. 2013.
- [59] S. A. Long and G. H. Huff, "A Fluidic Loading Mechanism for Phase Reconfigurable Reflectarray Elements," *IEEE Antennas Wireless Propag. Lett.*, vol. 10, pp. 876-879, 2011.
- [60] S. A. Long, W. M. Dorsey, G. H. Huff, N. Brennan, B. Rupp and M. A. Bevan, "Fluidic-Enabled Reconfigurable Patch With Integrated Dielectric Spectrometer," *IEEE Antennas Wireless Propag. Lett.*, vol. 13, pp. 1116-1119, 2014.
- [61] F. Farzami, S. Khaledian, B. Smida and D. Erricolo, "Reconfigurable Dual-Band Bidirectional Reflection Amplifier with Applications in Van Atta Array," *IEEE Trans. Microw. Theory Techn.*, no. 99, pp. 1-10, 2017.
- [62] R.E. Mihailovich, M. Kim, J.B. Hacker, E.A. Sovero, J. Studer, J.A. Higgins and J.F. DeNatale, "MEM Relay for Reconfigurable RF Circuits," *IEEE Microw. Compon. Lett.*, vol. 11, no. 2, pp. 53-55, 2001.
- [63] S. Danesh, S. K. A. Rahim, M. Abedian, M. Khalily and M. R. Hamid, "Frequency-Reconfigurable Rectangular Dielectric Resonator Antenna," *IEEE Antennas Wireless Propag. Lett.*, vol. 12, pp. 1331-1334, 2013.

- [64] Z. Chen and H. Wong, "Wideband Glass and Liquid Cylindrical Dielectric Resonator Antenna for Pattern Reconfigurable Design," *IEEE Trans. Antennas Propag.*, vol. 65, no. 5, pp. 2157-2164, 2017.
- [65] S. J. Mazlouman, A. Mahanfar, C. Menon and R. G. Vaughan, "Reconfigurable Axial-Mode Helix Antennas Using Shape Memory Alloys." *IEEE Trans. Antennas Propag.* vol. 59, no. 4, pp. 1070-1077, 2011.
- [66] J. Costantine, Y. Tawk, C. G. Christodoulou, J. Banik, and S. Lane, "CubeSat Deployable Antenna Using Bistable Composite Tape-Springs," *IEEE Antennas Wireless Propag. Lett.*, vol. 11, pp. 285-288, 2012.
- [67] G. J. Hayes, Y. Liu, J. Genzer, G. Lazzi and M. D. Dickey, "Self-Folding Origami Microstrip Antennas," *IEEE Antennas Wireless Propag. Lett.*, vol. 62, no. 10, pp. 5416–5419, 2014.
- [68] K. Miura, "Method of Packaging and Deployment of Large Membrane in Space," *Internat. Astronautical Congr. IAF*, Tokyo, Japan, 1980.
- [69] K. Miura, "Map Fold a La Miura Style, its Physical Characteristics and Application to the Space Science," *Internat. Meeting Origami Sci. Technol.*, Ferrara, Italy, 1989.
- [70] G. M. Olson, S. Pellegrino, J. Costantine and J. Banik, "Structure Architectures for a Deployable Wideband UHF Antenna," *53rd AIAA/ASME/ASCE/AHS structure, structural dynamics mater. conf.*, Hawaii, 2012.
- [71] K. Fuchi, J. Tang, B. Crowgey, A. R. Diaz, E. J. Rothwell and R. O. Ouedraogo, "Origami tunable frequency selective surfaces," *IEEE Antennas Wireless Propag. Lett.*, vol. 11, pp. 473-475, 2012.
- [72] C. M. Kruesi, R. J. Vyas and M. M. Tentzeris, "Design and development of a novel 3-D cubic antenna for wireless sensor networks and RFID applications," *IEEE Trans. Antennas Propag.*, vol. 57, no. 10, pp. 3293-3299, 2009.
- [73] I. T. Nassar and T. M. Weller, "Development of Novel 3-D Cube Antennas for Compact Wireless Sensor Nodes," *IEEE Trans. Antennas Propag.*, vol. 60, no. 2, pp. 1059-1065, 2012.
- [74] J. Constantine, Y. Tawk, I. Maqueda, M. Sakovsky, G. Olson, S. Pellegrino and C. G. Christodoulou, "UHF deployable helical antennas for CubeSats," *IEEE Trans. Antennas Propag.*, vol. 64, no. 9, pp. 3752–3759, 2016.
- [75] H. Hu and S. V. Georgakopoulos, "Wireless Powering Based on Strongly Coupled Magnetic Resonance with SRR Elements," *IEEE Antennas Propagat. Soc. Internat. Symp.*, Chicago, IL, Jul. 2012.

- [76] M. D. Dickey, R. C. Chiechi, R. J. Larsen, E. A. Weiss, D. A. Weitz, and G. M. Whitesides, "Eutectic Gallium-Indium (egain): a Liquid Metal Alloy for the Formation of Stable Structures in Microchannels at Room Temperature," *Advanced Functional Materials*, vol. 18, no. 7, pp. 1097–1104, 2008.
- [77] M. Cosker, L. Lizzi, F. Ferrero, R. Staraj and J. Ribero, "Realization of 3-D Flexible Antennas Using Liquid Metal and Additive Printing Technologies," *IEEE Antennas Wireless Propag. Lett.*, vol. 16, pp. 971-974, 2017.
- [78] W. Su, S. A. Nauroze, B. Ryan and M. M. Tentzeris, "Novel 3D printed Liquid-metal-alloy microfluidics-based Zigzag and Helical Antennas for Origami Reconfigurable Antenna "Trees"," *IEEE Internat. Microw. Symp.*, pp. 1579-1582, Honolulu, HI, Jun. 2017.
- [79] R. J. Lang, "Crease Pattern: Hexonion," *The FOLD*, Nov.-Dec., 2012.
- [80] T. Tachi, "Rigid Origami Simulation," [online]. Available: <http://origami.c.u-tokyo.ac.jp/~tachi/cg/>
- [81] M. Rutschlin and V. Sokol, "Reconfigurable Antenna Simulation: Design of Reconfigurable Antennas with Electromagnetic Simulation," *IEEE Microw. Magazine*, vol. 14, no. 7, pp. 92-101, 2013.
- [82] S. Yao, S. V. Georgakopoulos, B. Cook and M. M. Tentzeris, "A Novel Reconfigurable Origami Accordion Antenna," *IEEE Internat. Microw. Symp.*, Tampa Bay, FL, June, 2014.
- [83] S. Yao, X. Liu, S. V. Georgakopoulos and M. M. Tentzeris, "A Novel Tunable Origami Accordion Antenna," *IEEE Antennas Propagat. Soc. Internat. Symp.*, Memphis, TN, July 6-11, 2014.
- [84] P. Jackson, "*Folding Techniques for Designers: From Sheet to Form*," Laurence King Publishing Ltd, London. 2011
- [85] E. Strozyk and S. Neeb, "Accordion Collection," [online]. Available: <http://www.elisastrozyk.de/seite/accordioncollection.html>.
- [86] T. Lee, and J. M. Gattas, "Geometric Design and Construction of Structurally Stabilized Accordion Shelters," *J. Mechanisms Robotics*, vol. 8, no. 3, 2016
- [87] A. R. Djordjevic, A. G. Zajic, and M. M. Ilic, "Enhancing the Gain of Helical Antennas by Shaping the Ground Conductor," *IEEE Antennas Wireless Propag. Lett.*, vol. 5, pp. 138–140, 2006.
- [88] B. Trumbore, "Spring Into Action," [online]. Available: <http://trumbore.com/spring>

- [89] J. E. Lindsay, "A parasitic end fire array of circular loop elements," *IEEE Trans. on Antennas and Propag.*, vol. 15, no. 7, pp. 697-698, 1967.
- [90] S. Ito, N. Inagaki and T. Sekiguchi, "An investigation of the array of circular-loop antennas," *IEEE Trans. on Antennas and Propag.*, vol. 19, no. 4, pp. 469-476, 1971.
- [91] A. Shoamanesh and L. Shafai, "Properties of coaxial Yagi loop arrays," *IEEE Trans. on Antennas and Propag.*, vol. 26, no. 4, pp. 547-550, 1978.
- [92] V. H. Rumsey, "Frequency independent antennas," *Inst. Radio Eng. Int. Conv. Record, pt. I*, pp. 114–118, Mar. 1957.
- [93] V. H. Rumsey, "*Frequency Independent Antennas.*" New York: Academic, 1966.
- [94] J. D. Dyson, "The characteristics and design of the conical log-spiral antenna," *IEEE Trans. Antennas Propag.*, vol. 13, no. 4, pp. 488–499, 1965.
- [95] Y. Yu and K. Mei, "Theory of conical equiangular-spiral antennas part I-Numerical technique," *IEEE Trans. Antennas Propag.*, vol. 15, no. 5, pp. 634–639, 1967.
- [96] Y. Yu and K. Mei, "Theory of conical equiangular-spiral antennas part II – Current distributions and input impedances," *IEEE Trans. Antennas Propag.*, vol. 16, no. 1, pp. 14–21, 1968.
- [97] P. A. Ramsdale and P. W. Crampton, "Properties of 2-arm conical equiangular spiral antenna over extended bandwidth," *Microw., Optics and Antennas, IEEE Proc.*, vol. 128, no. 6, pp. 311–316, 1981.
- [98] T.W. Hertel and G. S. Smith, "Analysis and design of two-arm conical spiral antennas," *IEEE Trans. Electromagn. Compat.*, vol. 44, no. 1, pp. 25–37, 2002.
- [99] T.W. Hertel and G. S. Smith, "The conical spiral antenna over the ground." *IEEE Trans. Antennas Propag.*, vol. 50, no. 12, pp. 1668–1675, 2002.
- [100] Y. Z. Zhu and J. D. Xu. "Design of two-arm conical spiral antenna for low elevation angle communication," *J. Electromagn. Waves and Appl.*, vol. 24, pp. 785-794, 2010.
- [101] A. Gu, S. Yang and Z. Nie, "Analysis and Design of Miniaturized Ultra-Wideband Conical Log Spiral Antennas," *Cross Strait Quad-Regional Radio Sci. and Wireless Tech. Conf.*, pp. 191–194, Jul. 2013.
- [102] S. Yao, X. Liu, S. V. Georgakopoulos and M. M. Tentzeris, "A mode reconfigurable Nojima origami antenna," *IEEE Antennas Propagat. Soc. Internat. Symp.*, pp. 2237–2238, Vancouver, BC, Canada, Jul. 2015.

- [103] S. A. Zirbel, R. J. Lang, S. P. Magleby, M. W. Thomson, D. A. Sigel, P. E. Walkemeyer, B. P. Trease and L. L. Howell, "Accommodating Thickness in Origami-Based Deployable Arrays," *J. Mechanical Design*, vol. 135, no. 111005, pp. 1–11, 2013.
- [104] A. Rida, L. Yang, R. Vyas, S. Bhattacharya, and M. M. Tentzeris, "Design and integration of inkjet-printed paper-based UHF components for RFID and ubiquitous sensing applications," *2007 Eur. Microw. Conf.*, pp. 724–727, Munich, Germany, Oct. 2007,
- [105] C. Hartwanger, U. Hong, R. Gehring, E. Sommer, H. Grim and H. Schoedel, "SHF antenna farm," *Proc. of the 5th EUCAP*, pp. 1995–1999, Rome, Italy, Apr. 2011.
- [106] T. Kim, J. Yook and T. Yoo, "A CBCPW-fed ultra-wideband planar monopole antenna for UHF band applications," *IEEE Antennas Propag. Soc. Internat. Symp.*, pp. 205–206, Memphis, TN, Jul. 2014.
- [107] C. Hartwanger, U. Hong, R. Gehring, E. Sommer, H. Grim and H. Schoedel, "SHF antenna farm," *Proc. of the 5th EUCAP*, pp. 1995–1999, Rome, Italy, Apr. 2011.
- [108] T. Kim, J. Yook and T. Yoo, "A CBCPW-fed ultra-wideband planar monopole antenna for UHF band applications," *IEEE Antennas Propag. Soc. Internat. Symp.*, pp. 205–206, Memphis, TN, Jul. 2014.
- [109] S. S. Holland and M. N. Vouvakis, "The Planar Ultrawideband Modular Antenna (PUMA) Array," *IEEE Trans. Antennas Propag.*, vol. 60, no. 1, pp. 130–140, 2012.
- [110] M. H. Novak and J. L. Volakis, "Ultrawideband Antennas for Multiband Satellite Communications at UHF–Ku Frequencies," *IEEE Trans. Antennas Propag.*, vol. 63, no. 4, pp. 1334–1341, 2015.
- [111] H. L. Knudsen, "Radiation field of a square, helical beam antenna," *J. applied physics*, vol. 23, no. 4, pp. 483-491, 1952.
- [112] J. P. Casey and R. Bansal, "Square helical antenna with a dielectric core," *IEEE Trans. Electromagn. Compat.*, vol. 30, no. 4, pp. 429-436, 1988.
- [113] M.C. Britton, J.S. Wight and P.C. Strickland, "Low-cost square cross section helical antenna," *Symp. on Antenna Technol. and Appl. Electromagn*, Winnipeg, pp. 425–428, Manitoba, Canada, Jul. 2000.
- [114] Y. Wang and S. Chung, "A miniature quadrifilar helix antenna for global positioning satellite reception," *IEEE Trans. Antennas Propag.*, vol. 57, no. 12, pp. 3746–3751, 2009.
- [115] R. M. Barts, W. L. Stutzman, "A reduced size helical antenna," *Proc. IEEE Antennas Propag. Soc. Int. Symp.*, pp. 1588-1591, Jul. 1997.

- [116] S. A. Nauroze and M. M. Tentzeris, "A Novel Printed Stub-loaded Square Helical Antenna," *IEEE Antennas Propagat. Soc. Int. Symp.*, pp. 774–775, Vancouver, BC, Canada, Jul. 2015.
- [117] D. K. C. Chew and S. R. Saunders, "Meander Line Technique for Size Reduction of Quadrifilar Helix Antenna," *IEEE Antennas Wireless Propag. Lett.*, vol. 1, pp. 109–111, 2002.
- [118] S. Hebib, N. J. G. Fonseca and H. Aubert, "Compact printed quadrifilar helical antenna with iso-flux-shaped pattern and high cross-polarization discrimination," *IEEE Antennas Wireless Propag. Lett.*, vol. 10, pp. 635–638, 2011.
- [119] J. Rabemanantsoa and A. Sharaiha, "Size reduced multi-band printed quadrifilar helical antenna," *IEEE Trans. Antennas Propag.*, vol. 59, no. 9, pp. 3138–3143, Sep. 2011.
- [120] X. Liu, S. Yao, B. S. Cook, M. M. Tentzeris and S. V. Georgakopoulos, "A reconfigurable origami axial-mode helical antenna," *IEEE Trans. Antennas Propagat.*, vol. 63, no. 12, pp. 5897–5903, Dec. 2015.
- [121] X. Liu, S. Yao and S. V. Georgakopoulos, "Frequency reconfigurable origami quadrifilar helical antenna with reconfigurable reflector," *IEEE Antennas Propagat. Soc. Internat. Symp.*, pp. 2263–2264, Vancouver, BC, Jul. 2015,.
- [122] C. Hsu, S. Lin and Y. Lin, "Dual-frequency dual-sense circular polarization on asymmetric crossed-dipole antenna," *IEEE Antennas Propagat. Soc. Internat. Symp.*, Chicago, IL, Jul. 2012.
- [123] X. L. Bao and M. J. Ammann, "Monofilar spiral slot antenna for dual-frequency dual-sense circular polarization," *IEEE Trans. Antennas Propagat.*, vol. 59, no. 8, pp. 3061–3065, 2011.
- [124] M. Boti, L. Dussopt and J. M. Laheurte, "Circularly polarised antenna with switchable polarisation sense," *Electronics Letters*, vol. 36, no. 18, pp. 1518–1519, 2000.
- [125] Y. Ushijima, E. Nishiyama and M. Aikawa, "Circular polarization switchable microstrip antenna with SPDT switching circuit," *IEEE Antennas Propagat. Soc. Internat. Symp.*, Toronto, ON, Jul. 2010.
- [126] E. Demaine and M. Demaine, "History of curved origami sculpture," [Online]. Available: <http://erikdemaine.org/curved/history/>
- [127] E. Demaine, M. Demaine and A. Lubiw, "Polyhedral sculptures with hyperbolic paraboloids," *Proc. of the 2nd Annu. Conf. of BRIDGES: Math. Connections in Art, Music, and Sci.*, pp. 91–100, Winfield, Kansas, Jul. 1999.

- [128] S. Yao, X. Liu and S. V. Georgakopoulos, "Polarization switchable origami helical antenna," *IEEE Antennas Propagat. Soc. Internat. Symp.*, pp. 1667–1668, Fajardo, Puerto Rico, Jun. 2016.
- [129] W. Eakasit, "Helical antennas with truncated spherical geometry," M.S. thesis, Dept. Elect. Comput. Eng., VirginiaTech Univ., Blacksburg, VA, 2000.
- [130] X. Li, Q. Liu, J. Zhang and L. Zhao, "16-Element single-layer rectangular radial line helical array antenna for high-power applications," *IEEE Antennas Wireless Propag. Lett.*, vol. 9, pp. 708–711, 2010.

VITA

SHUN YAO

- 2002-2006 B. E. Electronic & Information Engineering
Shandong University
Jinan, China
- 2007-2011 M. S., Software Engineering
Beihang University
Beijing, China
- 2011-2017 Ph. D. Candidate, Electrical Engineering
Florida International University
Miami, Florida

PUBLICATIONS AND PRESENTATIONS

- [1] Stavros V. Georgakopoulos and Shun Yao, “Morphing origami multi-functional and reconfigurable antennas,” allowed, to be published (USPTO Patent Appl. No. 14/803,376).
- [2] Stavros V. Georgakopoulos and Shun Yao, “Segmented Helical Antenna with Reconfigurable Polarization,” filed in Jul. 2017 (USPTO Patent Appl. No. 15/643,981).
- [3] Stavros V. Georgakopoulos, Xueli Liu and Shun Yao, “Origami Antennas,” In: Antenna Engineering Handbook 5th Edition, J. L. Volakis ed., McGraw-Hill Press, 2017.
- [4] Shun Yao, Xueli Liu and Stavros V. Georgakopoulos, “Morphing Origami Conical Spiral Antenna Based on the Nojima Wrap,” *IEEE Transactions on Antennas and Propagation*, vol. 65, no. 5, pp. 2222-2232, 2017.
- [5] Xueli Liu, Shun Yao, Benjamin S. Cook, Manos M. Tentzeris and Stavros V. Georgakopoulos, “A Reconfigurable Origami Axial-Mode Helical Antenna,” *IEEE Transactions on Antennas and Propagation*, vol. 63, no. 12, pp. 5897-5903, 2015.
- [6] Shun Yao and Stavros V. Georgakopoulos, “Origami Segmented Helical Antenna with Switchable Sense of Polarization,” *IEEE ACCESS* (In minor revision).
- [7] Shun Yao, Kun Bao, Xueli Liu and Stavros V. Georgakopoulos, “Tunable UHF Origami Spring Antenna with Actuation System,” *IEEE Antennas Propagat. Soc. Internat. Symp.*, San Diego, CA, Jul. 9-14, 2017.

- [8] Shun Yao, Xueli Liu and Stavros V. Georgakopoulos, "Rotatable Segmented Helical Antenna with Reconfigurable Polarization," *IEEE Antennas Propagat. Soc. Internat. Symp.*, San Diego, CA, Jul. 9-14, 2017.
- [9] Shun Yao, Xueli Liu and Stavros V. Georgakopoulos, "Study and Design of Nojima Origami Conical Spiral Antenna," *IEEE Antennas Propagat. Soc. Internat. Symp.*, Fajardo, Puerto Rico, Jun. 26 - Jul. 1, 2016.
- [10] Shun Yao, Xueli Liu, Stavros V. Georgakopoulos and R. Schamp, "Polarization Switchable Origami Helical Antenna," *IEEE Antennas Propagat. Soc. Internat. Symp.*, Fajardo, Puerto Rico, Jun. 26 - Jul. 1, 2016.
- [11]. Shun Yao, Xueli Liu, John Gibson and Stavros V. Georgakopoulos, "A Self-deploy Yagi Loop Antenna Based on Origami Spring Structure," *IEEE Antennas Propagat. Soc. Internat. Symp.*, Vancouver, BC, Canada, Jul. 19-24, 2015.
- [12] Shun Yao, Xueli Liu and Stavros V. Georgakopoulos, "A Mode Reconfigurable Nojima Origami Antenna," *IEEE Antennas Propagat. Soc. Internat. Symp.*, Vancouver, BC, Canada, Jul. 19-24, 2015.
- [13] Shun Yao, Xueli Liu, Stavros V. Georgakopoulos and Manos M. Tentzeris, "A Novel Reconfigurable Origami Spring Antenna," *IEEE Antennas Propagat. Soc. Internat. Symp.*, Memphis, TN, July 6-11, 2014.
- [14] Shun Yao, Xueli Liu, Stavros V. Georgakopoulos and Manos M. Tentzeris, "A Novel Tunable Origami Accordion Antenna," *IEEE Antennas Propagat. Soc. Internat. Symp.*, Memphis, TN, July 6-11, 2014.
- [15] Shun Yao, Stavros V. Georgakopoulos, Benjamin Cook and Manos M. Tentzeris, "A Novel Reconfigurable Origami Accordion Antenna," *IEEE International Microwave Symposium*, Tampa Bay, FL, June 1-6, 2014.